Title

I. Transient Induced Molecular Electronic Spectroscopy (TIMES) technique to study the biomolecular interaction on the surface II. Microfluidic droplet-based techniques for single-cell study

Author

Tseng, Chi-Yang

Publication Date

2022

Peer reviewed|Thesis/dissertation

UNIVERSITY OF CALIFORNIA SAN DIEGO

I. Transient Induced Molecular Electronic Spectroscopy (TIMES) technique to study the biomolecular interaction on the surface
II. Microfluidic droplet-based techniques for single-cell study

A dissertation submitted in partial satisfaction of the
requirements for the degree
Doctor of Philosophy

in

Materials Science and Engineering

by

Chi-Yang Tseng

Committee in charge:

Professor Yu-Hwa Lo, Chair
Professor Prabhakar Bandaru
Professor Renkun Chen
Professor Tse Nga (Tina) Ng
Professor Oscar Vazquez Mena

2022

The dissertation of Chi-Yang Tseng is approved, and it is acceptable in quality and form for publication on microfilm and electronically.

University of California San Diego
2022

DEDICATION

To my family and friends.

TABLE OF CONTENTS

LIST OF FIGURES

LIST OF TABLES

ACKNOWLEDGEMENTS

To my advisor, Professor Lo, I really thank you for your guidance and encouragement through my graduate study here, not only for the support on academic research but also for the impact of you to make me become a much more independent thinker. I really cherish the time I work here in Lo's group.

To my Ph.D. committee, thank you for your suggestions and support to my Ph.D. completion. Especially thankful to Professor Bandaru, Professor Ng and Professor Vazquez Mena for the assistance during my difficulties at the first year in UCSD. I thank you for the support and encouragement.

To my collaborators on both projects, Fumin, Bobi and Celine, I thank you all for the support on research study. Every discussion with you really expands my biological knowledge. It was a memorable working experience with you.

To my lab mates, present and past, I thank you all for the help and discussion on experiments. I am really happy to meet you guys here, as we can share the same feelings and experiences. Especially to Ping-Wei and Brian, I thank you for the support on research as well as bringing cherish memory to my life here in San Diego, I cannot forget I have you as my best friends here.

I would like to thank my family lastly. I really appreciate my parents Chuan-Chen Tseng and Ling-Hsien Cheng for the greatest support to make me study abroad. Also, to my future wife I-Wen Brenda Huang, thank you for the accompany during my life in America. Thank you all, the support and encouragement from you are always the best inspiration to make me pursue my next journey in my life.

The thesis contains following papers which are either already published or under preparation:

Chapter 2 is a reprint material as it appears in *Scientific Report*s, 2019, Ping-Wei Chen, Chi-Yang Tseng, Fumin Shi, Bo Bi, Yu-Hwa Lo. Measuring electric charge and Molecular coverage on electrode Surface from transient induced Molecular electronic Signal (TIMES). *Scientific Reports,* 9, 1-10, 2019. The dissertation author contributed the work evenly as co-author.

Chapter 3 is a reprint of the material as it appears in *Analytical Chemistry* 2020, Ping-Wei Chen, Chi-Yang Tseng, Fumin Shi, Bo Bi, Yu-Hwa Lo. Detecting Protein–Ligand Interaction from Integrated Transient Induced Molecular Electronic Signal (i-TIMES). *Analytical Chemistry,* 92 (5), 3852–3859, 2020. The dissertation author contributed the work evenly as co-author.

Chapter 4, in part, is a reprint of the material as it to be published later: Chi-Yang Tseng, Alex Zhang, Yu-Hwa Lo. Paper-Based Transient Induced Molecular Electronic Signal (TIMES) on Reaction Kinetic Study. The dissertation author was the first author of this paper.

Chapter 5, in part, is a reprint of the material as it is to be published later as, Chi-Yang Tseng, Zhilin Guo, Celine Vuong, Edward Callaway, Yu-Hwa Lo. Enhancer Screening Using Single-Nuclei Droplet RT-PCR. The dissertation author contributed to the fabrication of device.

Chapter 6, in part, is a reprint of the material as it is to be published later as: Chi-Yang Tseng, Zhilin Guo, Rui Tang, Lauren Waller, Yu-Hwa Lo. Single-Cell Sequencing Using Imaging-Compatible Double Emulsion Sorting. The dissertation author was the first author.

Chi-Yang Tseng

San Diego, CA

March 2022

VITA

2010	Bachelor of Science in Chemistry, National Taiwan Normal University, Taiwan
2012	Master of Science in Chemistry, National Taiwan Normal University, Taiwan
2022	Doctor of Philosophy in Materials Science and Engineering, University of California San Diego, USA

PUBLICATIONS

Ping-Wei Chen, **Chi-Yang Tseng**, Fumin Shi, Bo Bi, Yu-Hwa Lo. Measuring electric charge and Molecular coverage on electrode Surface from transient induced Molecular electronic Signal (TIMES)**.** *Scientific Reports,* 9, 1-10, 2019

Ping-Wei Chen, **Chi-Yang Tseng**, Fumin Shi, Bo Bi, Yu-Hwa Lo. Detecting Protein–Ligand Interaction from Integrated Transient Induced Molecular Electronic Signal (i-TIMES). *Analytical Chemistry*, 92 (5), 3852–3859, 2020

Da Ying, Ping-Wei Chen, **Chi-Yang Tseng**, Yu-Hwa Lo, Drew A. Hall. A sub-pA current sensing front-end for transient induced molecular spectroscopy. *IEEE 2019 Symposium on VLSI Circuits*, C316-C317, 2019

Da Ying, **Chi-Yang Tseng**, Ping-Wei Chen, Yu-Hwa Lo, Drew A. Hall. A 30.3 fA/Hz Biosensing Current Front-End with 139 dB Cross-Scale Dynamic Range. *IEEE Transactions on Biomedical Circuits and Systems*, 15 (6), 1368-1379, 2021

Xinyu Chen, Lauren Waller, Jiajie Chen, Rui Tang, Zunming Zhang, Ivan Gagne, Bien Gutierrez, Sung Hwan Cho, **Chi-Yang Tseng**, Ian Y. Lian, and Yu-Hwa Lo. Label-free image-encoded microfluidic cell sorter with a scanning Bessel beam APL Photonics, 6 (7), 076101, 2021

Chi-Yang Tseng, Alex Zhang, Yu-Hwa Lo. Paper-Based Transient Induced Molecular Electronic Signal (TIMES) on Reaction Kinetic Study. *In preparation***,** 2022

Chi-Yang Tseng, Zhilin Guo, Celine Vuong, Edward Callaway, Yu-Hwa Lo. Enhancer Screening Using Single-Nuclei Droplet RT-PCR. *In preparation,* 2022

Chi-Yang Tseng, Zhilin Guo, Rui Tang, Lauren Waller, Yu-Hwa Lo. Single-Cell Sequencing Using Imaging-Compatible Double Emulsion Sorting. *In preparation,* 2022

ABSTRACT OF THE DISSERTATION

I. Transient Induced Molecular Electronic Spectroscopy (TIMES) technique to study the biomolecular interaction on the surface

II. Microfluidic droplet-based techniques for single-cell study

by

Chi-Yang Tseng

Doctor of Philosophy in Materials Science and Engineering

University of California San Diego, 2022

Professor Yu-Hwa Lo, Chair

As the microfluidic technology has been attracted more attentions and has potential for wide range of applications, in our research work we are utilizing this technique to expand its capability in different aspects of study. In this dissertation, I am going to present two topics of the work: Molecular interaction study using microfluidic techniques and Microfluidic droplet-based applications on single-cell analysis.

Biosensors are powerful analytical tools for many applications including drug discovery, medical diagnostics, and environment monitoring. Because of the advance of microfluidic technology, biosensors have a significant improvement by merging the biosensor into lab-on-chip (LOC) technology. In most of the microfluidic sensor, the detection mechanism is through the reaction event that occurs when the flowing analyte in the channel physically or chemically react with the immobilized reactant. The immobilization of

recognition elements is needed prior to the sample detection, but this can be a disadvantage of using microfluidic device due to one-time use only. To address this issue, we develop a new readout technique, “Transient Induced Molecular Electronic Signal (TIMES)”. The measured signal from TIMES is directly coming from the induced charge generated from the analyte or chemical reaction, and no immobilization of reactant on electrode surface is needed. I am going to present the work on protein-ligand study based on our microfluidic TIMES measurements, which is a highly potential study in drug discovery research area. Besides, TIMES technique has potential to be an alternative readout for lateral flow assay (LFA) study. The recent work we have done with paper-based TIMES study for antibodies binding interaction will be presented.

In the second topic, I am going to show our development on microfluidic device that used for single-cell analysis. There are two main workflows to perform single cell analysis: 1.) Plate-based method and 2.) Droplet-based method. The plate-based method is the traditional way, it is costly and time consuming. While in second method, the cells are encapsulated into small droplet, and all the reaction can be done in this tiny droplet, having capability to operate more than 10,000 cells in one reaction, so it saves more use of reagent and time on operation. In our study, we are trying to identify specific cell subtype by using enhancer screening with droplet-based analysis. However, the droplet manipulation is needed in this procedure. To be specific, droplet merging and double emulsion formation are two main steps in droplet-based analysis. Droplet merging is achieved for reagent addition after cells are lysed and RNA is released in the droplet. In our work, we developed a new microfluidic platform to merge droplets by using pillar-induced mechanism. The double emulsion is another main technique for droplet-based analysis. The main purpose for double emulsion formation is to make droplets compatible to water phase so the targeted droplets can be sorted with FACS equipment. In our study, we are going to expand its application on relating cell morphology to gene expression. The double emulsion technique is applied with image-guided sorting system that developed in our lab and combined with gene sequencing will provide value information for cell genotype-phenotype analysis.

Chapter 1

Introduction

1.1 Introduction – TIMES technique

Biosensors are considered powerful analytical tools for wide range applications including drug discovery, medical diagnostics, and environment monitoring.[1] The working principle of biosensor is to detect the interaction between analyte of interest to the reactant, which can be immobilized physically or chemically to the surface of transducer, and the identification of reaction event can be transferred into electrical or optical signal through external readout. The specificity or selectivity of biosensor is determined by the analyte of interest and the recognition elements.

As the advance of microfluidic technology, biosensors have a significant improvement by merging the biosensor into lab-on-chip (LOC) technology. The microfluidic technique provides several benefits, such as low cost of fabrication, reduction of reagent use, and high throughput sample detection and processing.[2] Microfluidic biosensors have been designed for many kinds of applications by their demand,

such as use in aptamer[3], antibody detection[4] and in glucose detection[5]. Those applications can be further used for clinical diagnostics and point-of-care (POC) application.

In most of the microfluidic sensor, the detection mechanism is through the reaction event that occurs when the flowing analyte in the channel physically or chemically react with the immobilized reactant. The immobilization of recognition elements is needed prior to the sample detection, this can be a disadvantage of using microfluidic device. The one-time immobilized device can only be used for detection of one type of interested analyte and leads to a great limitation for wide range application. To address this issue, we develop our own measure system, "Transient Induced Molecular Electronic Signal (TIMES)", to provide wider range of biomolecule detection. The detect signal measured by TIMES is directly coming from the induced charge generated from the analyte or reaction product, and no immobilization of reactant on electrode surface is needed. By using TIMES measurement, we not only present molecule detection in microfluidic device, but also show the capability on paper-based reaction detection. This label-free and immobilization-free measurement method offers wide applications and benefits in study of surface charge detection, protein-ligand interaction for drug discovery, and paper-based antibody-antigen reaction. Here, I would like to introduce the significance of those aspects of application on TIMES in the next separate chapters, Chapter 2 to Chapter 4.

1.2 Introduction – Microfluidic droplet-based technique

Droplet-based single-cell platform attracts more attentions because it provides high throughput and low-cost analysis. Not only because of those advantages but it provides higher specific cell type identifying with feasible methodology. In our study, we are trying to identify specific cell subtype by using enhancer screening. These rare cell types that occupy only ~2% population in brain and is hard to get access to its gene expression by using traditional single-cell analysis method.

Droplet based single cell analysis can be achieved in easier way, but many considerations in microfluidic channel design is needed. To be specific, droplet merging and double emulsion formation are two main steps in droplet-based analysis. Droplet merging is used for merging two droplets that one is contained RNAs from lysed cell inside and the other contained RT-PCR reagent inside. By droplet merging, these two droplets can combine together so that qPCR can be operated in the next step. Double emulsion is another main technique used for droplet-based analysis. The main purpose for double emulsion formation is to make the oil-phased droplets compatible to water phase so the targeted droplets can be sorted with FACS equipment and followed by gene sequence procedure. These two techniques are what we focus on to develop and will apply for those projects. I will separately present our work on enhancer screening using droplet-based analysis in Chapter 5, and 2D-image guided sorting system combined with double emulsion technique in Chapter 6.

Chapter 2

Surface Charge Density Measurement

2.1 Introduction

Surface charge density and molecular coverage play important roles in understanding and control of surface chemistries and reactions for many chemical and biomedical applications such as surface coatings, immunoassays, nucleic acid hybridization, etc. Due to chemical potential difference between a solid surface and a solution, the prevailing model suggests that an electrical double layer is formed at the solid-liquid interface.[6-7] It is conceived that the electrical double layer consists of two layers of charge: a Stern layer where the charge is bonded more tightly with the surface atoms in the solid and a diffusion layer where charged ions are highly mobile and their concentrations follow the Boltzmann distribution. If the solid surface is conductive, the total amount of charge in these two layers is counter balanced by the induced charge in the conductive surface to assure charge neutrality of the overall system. All charges in this double layer of the solution phase are called surface charge. Influenced by the sign and density of surface charge, ions or molecules in solution can be attracted to or repelled from the surface via charge-charge or charge-

dipole interaction. Hence surface charge density can affect the thermodynamics and kinetics of surface reactions.

Because of the importance of surface charge density to surface chemistry, extensive molecular dynamic simulations have been performed to calculate the surface charge density for solutions of different ionic composition and pH value[8-9]; and many attempts have been made to experimentally measure this and other related quantities[10-11]. So far atomic force microscopy (AFM)[12-16], surface plasmonic resonance[17-18], streaming potential[19-23], and contact angle titration[24-26] are among the most studied techniques that can produce information related to the surface charge density although none of the existing methods, to our best knowledge, can easily and directly measure the polarity and amount of surface charge in the natural environment where surface reactions take place.

To apply AFM to measure surface charge, one measures the force of Coulomb interactions between the AFM tip and the local surface under the tip[12-16]. In this technique, the surface charge density at the liquid/solid interface is obtained by analyzing the electrostatic force as a function of the distance between the tip and the surface. By chemically functionalizing the sample surface, the force between the surface and the AFM tip is changed. Wu et al. investigated the force change by different functional molecules such as -Br, $-NH_2$ and $-CH_3$ on the surface[16]. The results show a strong relation between the surface charge density and the surface modifications as well as the liquid pH value. Although the AFM technique provides in-sights about the surface electric properties under different environments, the measurements require sophisticated instrument, have low throughput, rely on detailed information about the tip geometry and its surface charge distribution, and perturb the local environment due to the close proximity of the AFM tip to the surface under test.

Alternatively, surface plasmonic resonance (SPR) technique has been applied to study the effects of surface charge. Shan *et al*. has used electrostatic repulsion between charged particles of the same polarity to balance the gravity in a SPR system[17-18]. Since SPR is sensitive to the refractive index change near a sensor surface, it can be used to measure the equilibrium distance of a particle from the SPR sensor surface.

SPR technique has been utilized to show that ionic strength of the solution and surface modifications can change the equilibrium distance between the particle and the surface. However, due to the relatively large size of the particle, difficulties in measuring the distance between the particle and the surface, and the surface properties of the particle itself which may alter the local distributions of the ions in the solution, the SPR technique is more suitable for qualitative instead of quantitative studies of surface properties in solution[27-28].

There exist also significant efforts to use streaming potential measurements to characterize the surface charge density[19-23]. The technique measures the voltage difference generated by a pressure driven flow over a charged surface or membrane. This measured voltage difference can be used to obtain zeta potential. Although one can find the charge density in the diffusion layer from zeta potential, the amount of charge in the diffusion layer is not equal to the total amount of surface charges according to the double layer model. As a result, the streaming potential technique is more suitable for comparing surface properties between different surface modifications. For example, Datta *et al*. has used streaming potential measurement to characterize synthetic membranes with different pore sizes and surface modifications[20]. Kim *et al*. has applied the technique to show that the electric property of a membrane is strongly dependent on the pH value and ionic strength of the solution[21]. In addition to the above methods, people have also measured contact angles to determine the surface charge density at the liquid/solid interface[24-26]. By combining the Young-Lippmann equation with the Guoy-Chapman model for electrical double layer, Horiuchi *et al*. has applied a three-phase contact angle titration measurement to find the dependence of surface potential and surface charge density on the solution pH value[25]. However, since the contact angle is highly sensitive to the surface physical and chemical properties, the contact angle titration measurement is quite complex and difficult to obtain reliable results, and often underestimates the surface charge density.

In this paper, we have extended the method of Transient Induced Molecular Electronic Signal (TIMES) reported earlier to directly measure the surface charge for any solution in contact with a conductive surface[29-30]. The results produce the amount and polarity of the surface charge in solution that

is in contact with the electrode surface. We integrated TIMES currents over a time period to obtain change in the amount of the surface charge when the test sample is displaced by a reference buffer. We also like to point out that the TIMES signals are generated by ions or molecules that are not permanently adhered to the electrode surface. In other words, if a molecule, charged or not, is permanently anchored to the surface of electrode, it would not contribute to the TIMES signal. Using this property, we can not only measure surface charge density but also surface coverage of molecules that are immobilized on the electrode surface. This is another salient feature for our technique since the knowledge of area coverage of certain molecules such as DNA capture probes or antibodies is particularly valuable for optimization of the reaction conditions and ensuring reproducible results for any microarrays.

2.2 Device setup and working procedures

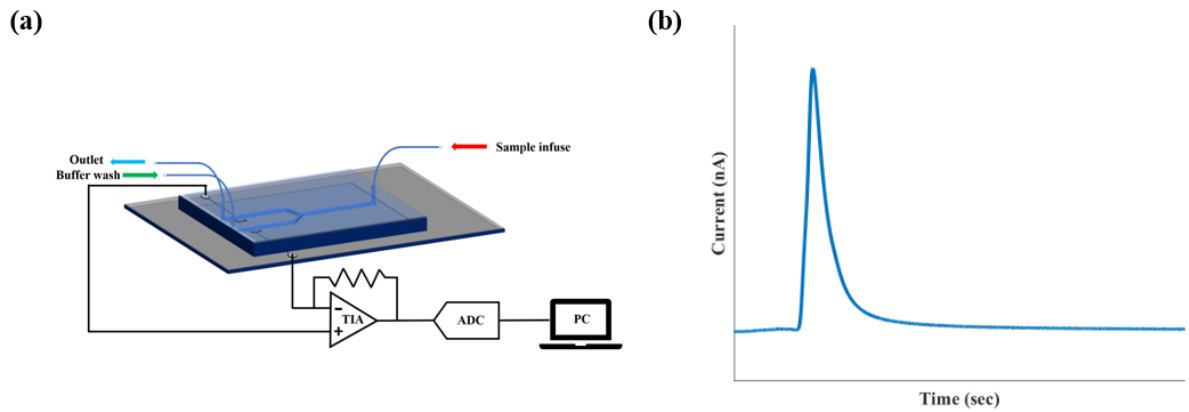

Figure 2.1. (a) Schematic diagram of device design and TIMES setup, (b) A typical TIMES signal produced by displacing the test sample with a reference buffer over the sensing electrode.

In this work, we have applied the TIMES technique to measure surface charge density for buffers of different concentration (ionic strength), pH value, and buffer types. The TIMES system consists of a microfluidic device with two parallel microfluidic channels that are connected to a single channel via a Y-

junction. Within each parallel channel that is 1mm wide and 30μm high, there is a platinum electrode connected to the external circuit by a bond wire. The electrode area within the channel is 1x1 mm^2. One of the electrodes is used as the sensing electrode and the other as the reference electrode. Both electrodes are connected to the differential inputs of a transimpedance amplifier (TIA) with a tunable transimpedance (Figure 2.1a). In the beginning of the experiment, the channel with the reference electrode is filled up with reference buffer, and the channel with the sensing electrode is filled up with the sample solution. After soaking each electrode in the respective solution for a sufficient amount of time for the system to reach its steady state, we flow the reference buffer into the channel with the sensing electrode at a flow rate of 100 uL/min so that the sample solution in contact with the sensing electrode is displaced by the reference buffer. We call this step the "washing process" and it is during this "washing process" that the TIMES signal is recorded. In other words, we measure the transient current flowing from the sensing electrode into the transimpedance impedance amplifier when the solution above the sensing electrode is switched from the sample solution to the reference buffer.

We can apply the above procedure to measure the absolute amount and polarity of surface charge for essentially any buffer/electrode combinations. The relative difference in the surface charge between the sample solution and the reference buffer can be obtained by integrating the TIMES current signal over the duration of buffer switching from sample solution to reference buffer. We can obtain the absolute amount of surface charge for the sample solution by choosing a reference buffer that has zero surface charge for a certain electrode. Since we know 0.099 M $KClO_4$/0.001 M $HClO_4$ (pH = 3.4) solution produces zero surface charge with Pt electrode[31], we can use this buffer and another electrode (e.g. Au) to find the surface charge between the buffer and the new electrode material. Similarly, for a given electrode (e.g. Pt), we can also find the surface charge between a new buffer and the electrode by comparing its signal with the signal from the reference (e.g. 0.099 M $KClO_4$/0.001 M $HClO_4$) buffer.

In this paper, we firstly used 0.099 M $KClO_4$/0.001 M $HClO_4$ (pH = 3.4) as the reference buffer to measure the surface charge of 1X PBS (pH=7.41) in contact with Pt electrode. Then for all other

experiments, we used 1X PBS (pH=7.41) as the reference buffer to measure the surface charge of other solutions of different ionic strength, pH value, buffer types, etc. Figure 2.1b shows a typical TIMES signal when displacing the sample solution over the sensing electrode by the reference buffer.

The above process can be described in a simple mathematical formula.

$$S(t) = \int_0^t I(\tau)d\tau = Q_{sample} - Q_{reference} \quad (1)$$

where Q_{sample} is the surface charge in the double layer of the sample solution and $Q_{reference}$ is the corresponding quantity for the reference buffer. Equation (1) also shows that any permanently adhered molecules does not contribute to the signal since only movable charge produces current. Using this important property, we further demonstrated how the TIMES technique can be used to measure surface coverage of molecules anchored to the surface, as described next.

To determine the effect of surface modification by adherent molecules, we have used thiol-modified nucleic acid and 6-mercapto-1-hexanol (MCH) as test molecules. The former forms strong sulfur-platinum linkage, and the MCH molecule also contains a thiol group and is often used as a blocking agent to displace weaker adsorptive contacts between DNA nucleotides and the Pt (Au) substrate to suppress non-specific binding for DNA hybridization experiment. To measure surface coverage by thiol-modified DNA and by MCH, we soaked the sensing electrode in solutions containing different concentrations of thiol-modified DNA. The Pt electrode surface covered by thiol-modified DNA contains fixed charge that cannot be changed by the aforementioned washing process, thus giving rise to no TIMES signal. As a result, if α is the fraction of area covered by the anchored molecule, the magnitude of the TIMES signal in equation (1) will be reduced to 1-α times of the signal without molecular coverage. This provides an easy and direct method to measure molecular coverage, a quantity that is critical to the optimization and repeatability for molecular sensing but has not been able to measure till now.

2.3 Results and discussions

Measuring absolute charge density with zero-surface-charge buffer as the reference

Since we used 1X PBS as the reference and washing buffer for most of the experiments discussed in the paper, we first describe the method of measuring the surface charge density for 1X PBS in contact with the Pt electrode. According to Rizo *et al*., the solution of 0.099 M $KClO_4$ and 0.001 M $HClO_4$ (pH = 3.4) yields zero-surface charge (ZSC)[31]. Therefore, we can obtain the surface charge density for buffer 1X PBS (pH=7.41) by using ZSC ($KClO_4$/$HClO_4$) as the reference and washing buffer. Following the procedures described in the previous section, we obtained the TIMES signal (Figure 2.2a) and the surface charge (Figure 2.2b) using equation (1) with 1X PBS being the "sample" and ZSC buffer as the "reference". The result shows that at the 1X PBS/Pt electrode interface, there exists a charge density of 70.67±0.37 mC/m^2 in the double layers. In the following experiments where we use 1X PBS as the reference and washing buffer, we will add this amount to the results to obtain the actual amount of surface charge density since our method measures the surface charge difference between the sample solution and the washing buffer.

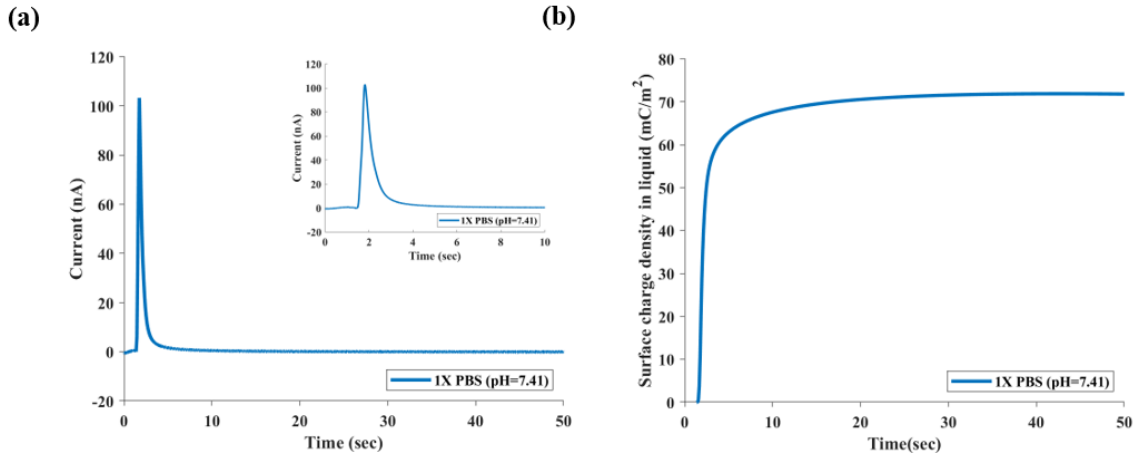

Figure 2.2. TIMES signal with 1X PBS on the sensing electrode displaced by the zero-surface charge (ZSC) solution. (a) TIMES signal. The inset shows the detailed waveform of the current transient. (b) Change of surface charge density at the solution/solid interface by integration of the TIMES signal over time. The final value when the system reaches steady state gives rise to the equilibrium surface charge density of the liquid (1X PBS) in contact with a conductive surface (Pt).

The effects of ionic strength and pH value on the surface charge density

The TIMES signals produced by PBS of different concentration (or ionic strength) are shown in Figure 2.3a. Applying equation (1) with the sample being the PBS of different concentration and the reference (washing buffer) being 1X PBS, we obtain the dependence of surface charge density on the PBS concentration (Figure 2.3b). 1X PBS buffer has its ionic strength (IS) of 162mM and pH value of 7.41. By varying its ionic strength from 1.6 mM to 1620 mM while keeping the pH value the same (by adding a very small amount of HCl or NaOH that did not alter the ionic strength of the buffer), we have found the following relation between the surface charge density and ionic strength:

$$\boldsymbol{Q - Q_o = -Q_n \ log\left(\frac{IS}{IS_o}\right),\ \ Q_n = 2.59\ mC/m^2}$$

It becomes apparent that lower ionic strength produces a greater amount of positive surface charge in the solution in contact with the Pt electrode. However, the effect of ionic strength on the surface charge is rather small since the surface charge density changes from 76.09±0.47 to 68.73±0.06mC/m^2 when the ionic strength varies by 1000 times from 1.6mM to 1620mM.

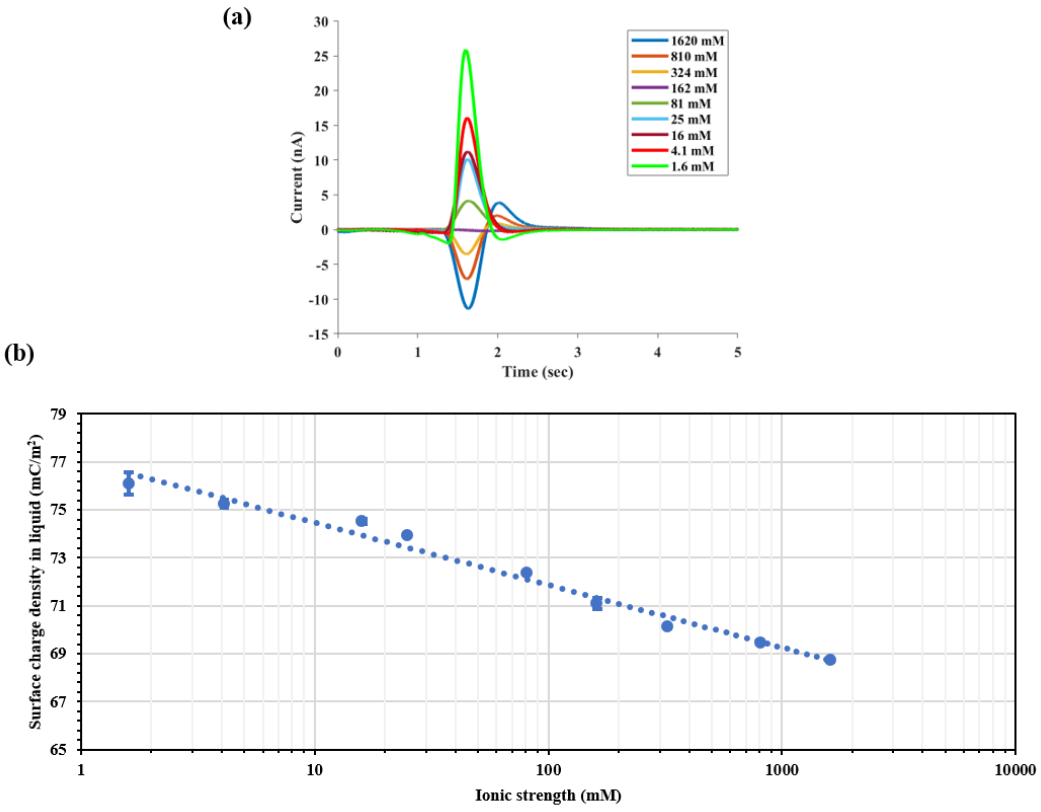

Figure 2.3. TIMES signals (a) and surface charge density (b) for different PBS concentration (ionic strength).

The effect of pH value on the surface charge can be obtained following a similar approach. In this study, we have fixed the ionic strength to 1X PBS (162mM) and varied its pH value from 5.69 to 9.65 by adding a small amount of HCl or NaOH. Again, using equation (1) with 1X PBS (pH=7.41) being the reference and washing buffer, we have measured the TIMES signals and the surface charge density dependence on the pH value of the buffer. From Figure 2.4b, we can obtain the relation:

$$Q - Q_o = -Q_m \, log\left(\frac{[H^+]}{[H^+]_o}\right), \quad Q_m = 13.67 \, mC/m^2$$

It was found that the surface charge density shows a much stronger dependence on the pH value than the ionic strength. Also, the surface charge density becomes more positive with increasing pH value of the buffer.

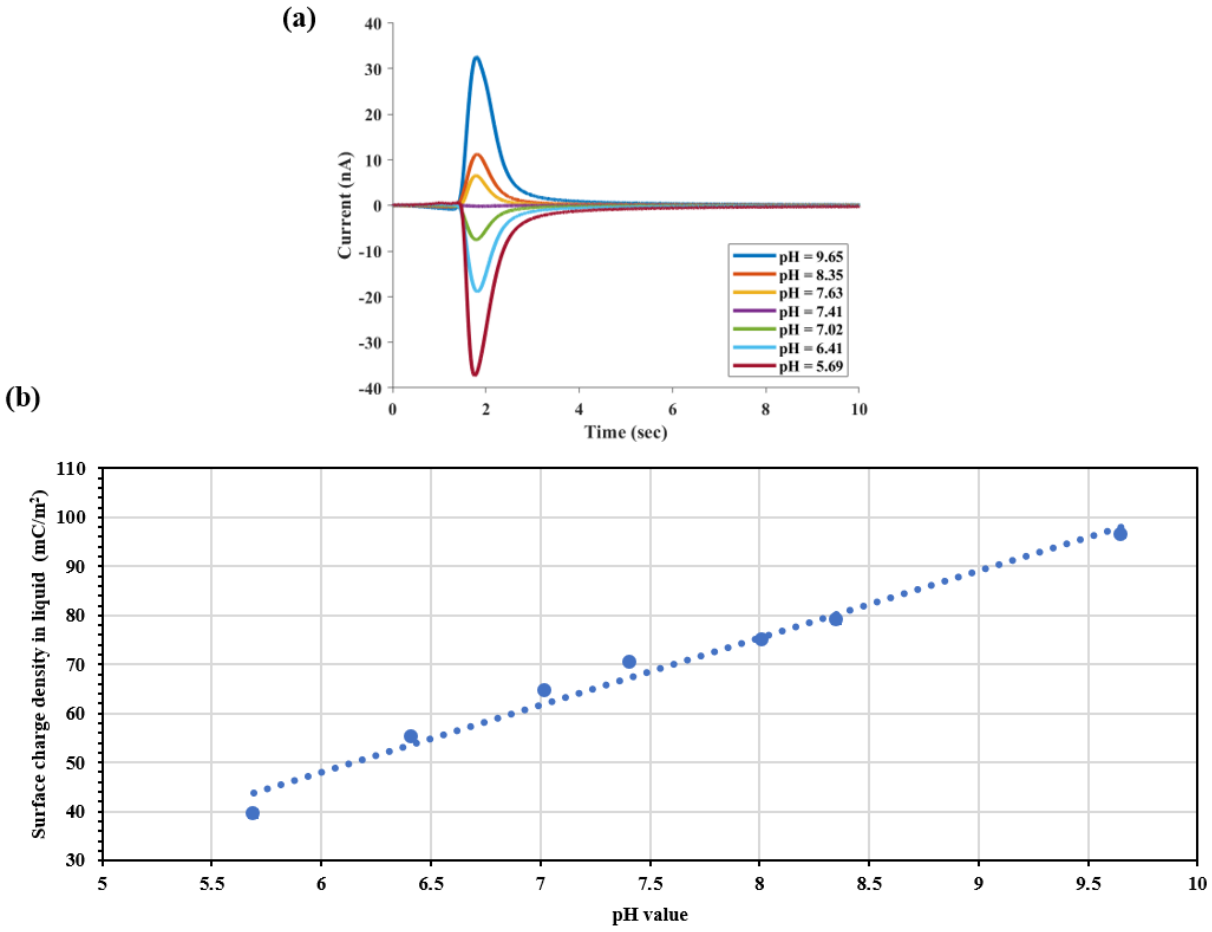

Figure 2.4. TIMES signals (a) and surface charge density (b) for different pH value of 1X PBS (IS=162 mM).

Surface charge density for different buffer types

A biological buffer typically consists of a weak acid and its conjugate base to provide a stable pH environment. We have measured the surface charge for some popular buffer solutions for biological samples, including Tris buffer and HEPES buffer. Figure 2.5 shows the TIMES results when we used 25 mM PBS, 25mM Tris buffer, and 25mM HEPES buffer as sample solutions and 1X PBS (162mM, pH=7.41) as the reference and washing buffer at room temperature (25^{o}C). The ionic strength of 25mM was chosen because it is the preferred concentration for many biological samples. Also noted that for sample solutions

under test, we have kept their pH value at their natural state: 7.26 for 25mM PBS, 7.56 for Tris, and 7.16 for HEPES. After integrating the TIMES signals as before, we have found that the surface charge density for 25mM PBS, 25mM Tris buffer, and 25mM HEPES buffer are nearly the same: 73.94±0.03, 74.19±0.04 and 75.95±0.04mC/m^2, respectively.

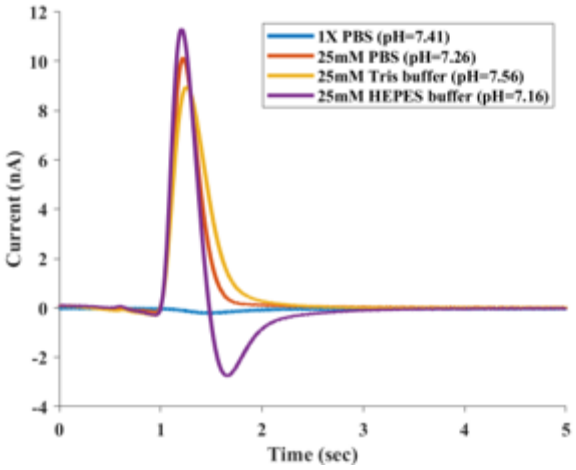

Figure 2.5. TIMES signals for 25 mM PBS, 25 mM Tris buffer, and 25 mM HEPES buffer with 1X PBS (162 mM) being the reference and washing buffer.

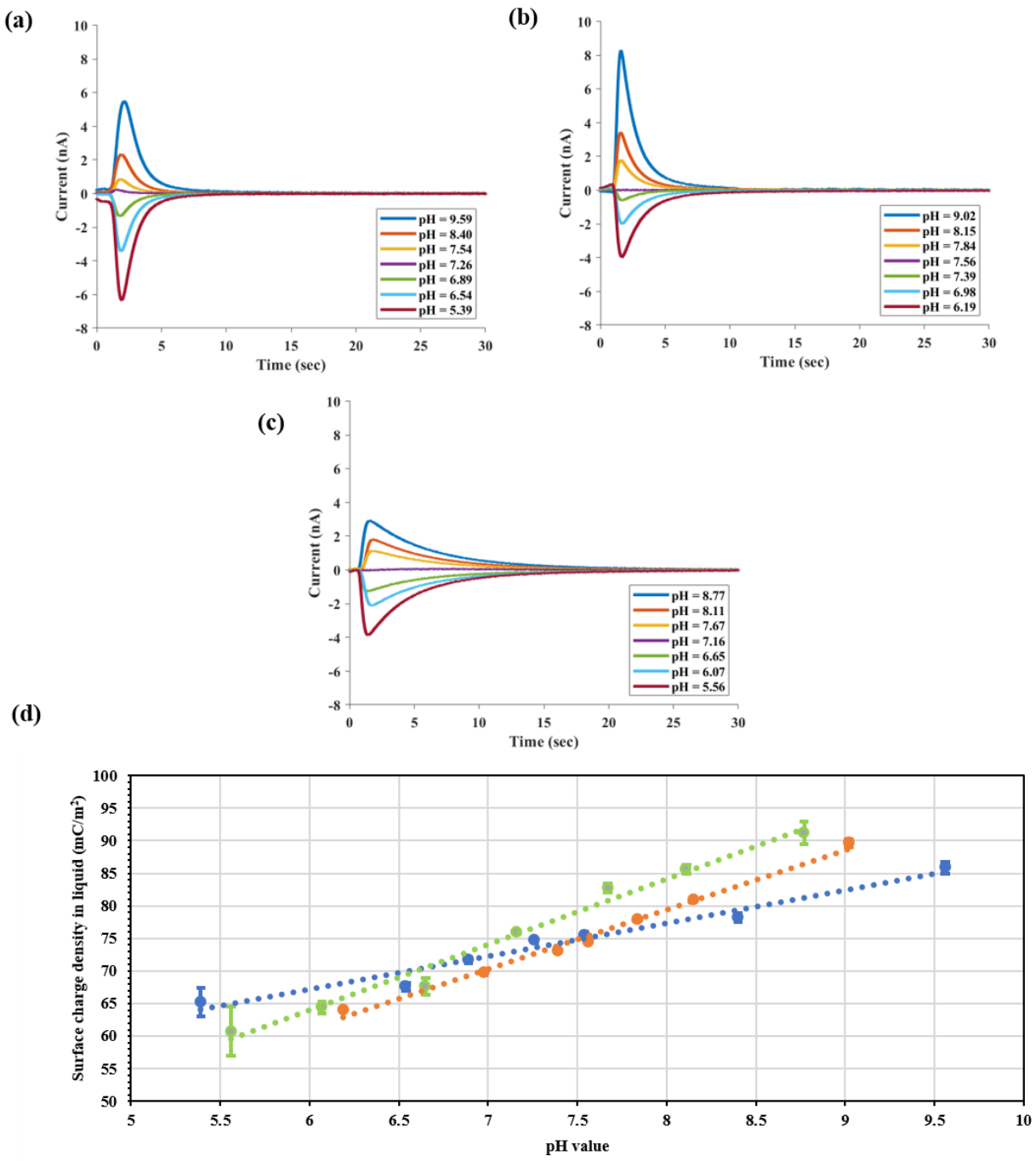

Figure 2.6. TIMES signals for 25mM PBS (a), 25mM Tris buffer (b), and 25mM HEPES buffer (c) of different pH value. (d) pH dependence of surface charge density for 25mM PBS (blue), 25mM Tris buffer (orange), and 25mM HEPES buffer (green) buffers.

Next we found the pH value dependence of surface charge density for each buffer and the results are summarized in Figure. 2.6. The TIMES signals in Figure. 2.6a-c were generated by washing the test samples of different pH value with the same type of 25 mM buffer at its natural pH value (i.e. 7.26 for PBS, 7.56 for Tris buffer, and 7.16 for HEPES buffer). Figure 2.6d shows the pH dependence of surface charge density for all three buffers.

Effects of surface modification and surface coverage by immobilized molecules

By extending the TIMES method, we can measure the effects of surface modification and the fraction of molecular coverage. Here we have used the concept that any fixed charge created by immobilized molecules on the electrode surface does not contribute to the TIMES signal. Therefore, when a fraction of the electrode surface is covered by immobilized molecules, the magnitude of the TIMES signals decreases. Provided α be the fraction of surface area covered by a type of molecule bonded to the surface, the surface charge density measured by the TIMES signal is expected to be $1-\alpha$ times of signal without surface coverage. Therefore, by taking the ratio of the integrated TIMES signal with and without molecular coverage, we can obtain the fraction of molecular coverage after surface modification. Such information is highly valuable because quantifying the surface coverage by molecules is essential to assure effective surface treatment and repeatable test results for nucleic acid hybridization, immunoassay, particle capturing, and many surface reactions.

In our experiment, we used thiol-modified ssDNA and MCH to demonstrate the ability of measuring surface coverage by adherent molecules. We first tested the surface coverage of MCH as a blocking agent to prevent non-specific binding for sensors of nucleic acid since MCH is supposed to cover any surface area that was not occupied by DNA probes. The sensing electrode in the microfluidic channel was first soaked in 1mM MCH solution for 3 hours for surface modification. Then the sensing electrode was filled up with 1X PBS with pH=5.69 as the “sample solution”. When the sample solution was displaced by 1X PBS with pH=7.41, the TIMES signal was recorded, as shown in Figure 2.7a. One can relate surface coverage by MCH to the TIMES signal using the following relations:

$$S_1 = Q_{pH5.69} - Q_{pH7.41} \quad (2)$$

$$S_2 = (1 - \alpha_{MCH})(Q_{pH5.69} - Q_{pH7.41}) \quad (3)$$

where S_1 and S_2 are the TIMES signals with and without MCH surface treatment and α_{MCH} is the fractional area coverage by MCH molecule. From equation (2) and (3), we obtain:

$$\alpha_{MCH} = 1 - \frac{S_2}{S_1} \quad (4)$$

Figure 2.7a shows the TIMES signals of the above experiment, and the fractional surface coverage for MCH molecule was found to be α_{MCH}=0.944±0.004, as indicated in the first row of Table 2.1. The result shows that 94.4±0.4% of electrode surface area has been covered by MCH as an effective agent to prevent non-specific binding in biosensing.

Next we performed experiment with bonding of thiol-modified ssDNA probe of different concentrations (1μM, 10nM and 100pM) to the Pt surface. The ssDNA solution was introduced to the sensing electrode and kept overnight to reach the equilibrium state. Then the channel with the ssDNA treated electrode was filled up with the "sample solution" of 1X PBS with pH=5.69. TIMES signals were recorded when the sample solution was displaced by the reference buffer (1X PBS with pH=7.41). Following the measurement, 1 mM MCH was introduced to the ssDNA treated electrode as a blocking agent to cover areas uncovered by ssDNA. Following the same procedure described previously, we measured TIMES signal after MCH treatment. For the ssDNA/MCH treated surface, the signals are expected to follow the relations:

$$S_4 = (1 - \alpha_{ssDNA})(Q_{pH5.69} - Q_{pH7.41}) \quad (5)$$

$$S_5 = (1 - \alpha_{ssDNA} - \alpha_{MCH})(Q_{pH5.69} - Q_{pH7.41}) \quad (6)$$

where S_4 and S_5 are the TIMES signals after ssDNA modification and after MCH treatment, respectively. From equation (2), (5) and (6), we can obtain the fractional surface coverage by ssDNA (α_{ssDNA}) and by MCH (α_{MCH}). The TIMES signals for different ssDNA concentrations and for the MCH treatment that followed the ssDNA surface modification are shown in Figure 2.7b-d.

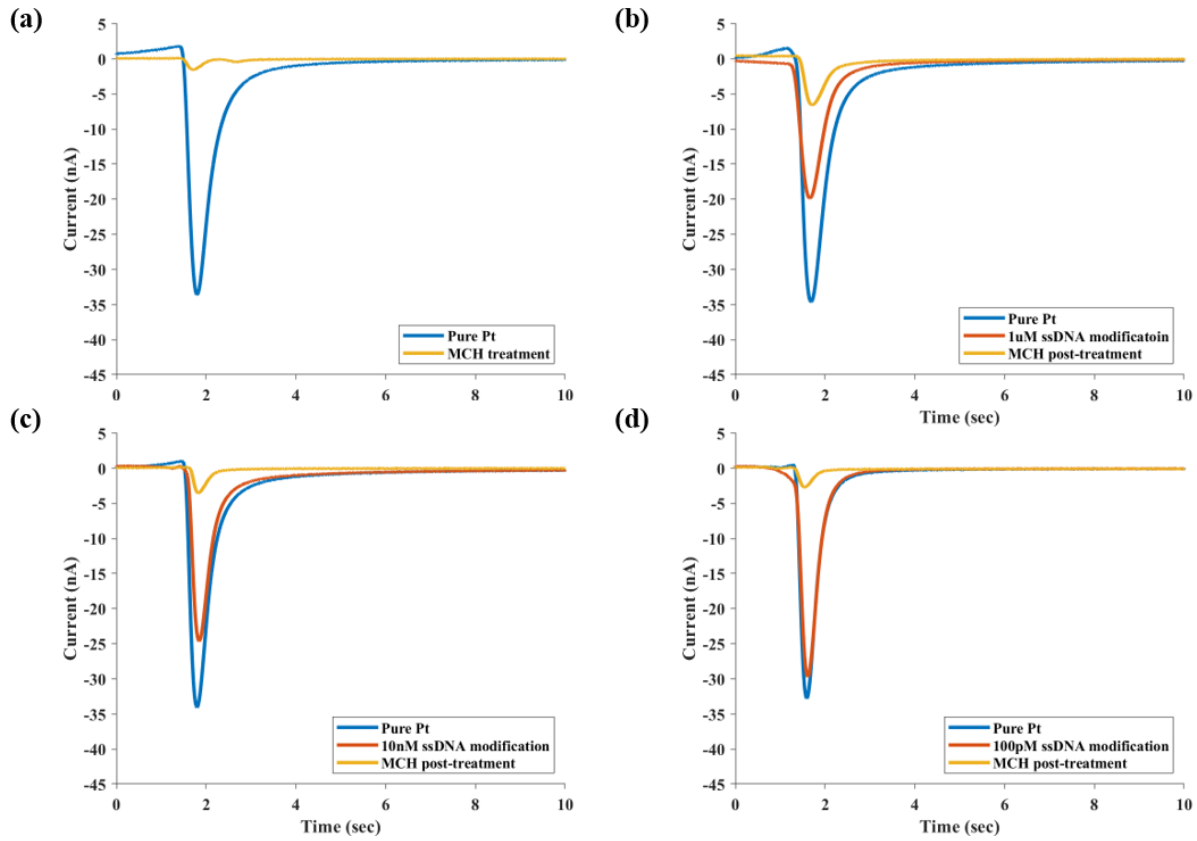

Figure 2.7. TIMES signals produced by displacing 1X PBS (pH=5.69) by 1X PBS buffer (pH=7.41) under different surface modification. (a) MCH treatment only, (b) 1μM ssDNA modification followed by MCH treatment, (c) 10nM ssDNA modification followed by MCH treatment (d) 100pM ssDNA modification followed by MCH treatment.

The fractional surface coverage by ssDNA and MCH under different conditions is listed in Table 2.1. It was found that when the ssDNA volume concentration changes from 1μM to 100pM, the surface coverage over the Pt surface changes from 48.2±3.3% to 12.2±0.8%. The results approximately follow the logarithmic relation:

$$\alpha_{DNA} \sim \alpha_{DNAo} log\left(\frac{n_{DNA}}{n_{DNAo}}\right)$$

Another interesting insight is that in all cases, the total fractional surface coverage by ssDNA and MCH is between 82.2 and 91.5% and never reaches 100%. Even with MCH alone, the surface coverage is 94.3% instead of 100%. One possible explanation for this phenomenon is that the surface molecules repel

molecules of the same charge polarity. Since thiol-modified DNA contains higher charge density in its sugar backbone than MCH molecule, we have observed higher percentage of coverage by MCH alone (94%) than by ssDNA/MCH combination (82-91%). This hypothesis is also consistent with the observation that the lowest surface coverage (82%) was obtained from the sample having the highest ssDNA coverage[32]. The above findings, made possible by the technique of measuring molecular surface coverage, shed light on the design and optimization of biosensors based on binding with surface probes.

Table 2.1. Fraction of surface coverage by MCH and ssDNA/MCH surface treatments

Condition	Surface coverage (%)		
	ssDNA	MCH	ssDNA+MCH
1 mM MCH	**-**	**94.3±0.3**	**-**
1 µM ssDNA followed by MCH	**48.2±3.3**	**33.9±3.1**	**82.2±0.9**
10 nM ssDNA followed by MCH	**22.6±1.7**	**69.0±1.6**	**91.5±0.2**
100 pM ssDNA followed by MCH	**12.2±0.8**	**78.8±0.6**	**91.1±0.7**

2.4 Conclusions

TIMES method has been proved to be capable of measuring surface charge density with high signal quality. By using the ZSC solution to the Pt electrode as a reference, we were able to measure the actual value of surface charge density for any chosen buffer suitable for biochemical applications. Using the TIMES method and the designed experimental procedures, we have shown quantitatively how the surface charge density is affected by the ionic strength, pH value and type of buffer. Taking advantage of the salient feature that any molecules, charged or not, immobilized on the surface does not contribute to the TIMES signal, we have developed schemes to measure surface coverage for immobilized molecules. We have used thiol-modified ssDNA and MCH molecules as examples to prove the concept. Finally, although in this study we have used time integrated TIMES signals for surface charge and surface coverage measurements, we should mention that rich information is also contained in the temporal waveform of the TIMES signal, which may provide insight about kinetics and charge transport at the solid/liquid interface, as an interesting subject for future study.

2.5 Acknowledgement

Chapter 2 is a reprint material as it appears in *Scientific Report*s, 2019, Ping-Wei Chen, Chi-Yang Tseng, Fumin Shi, Bo Bi, Yu-Hwa Lo. Measuring electric charge and Molecular coverage on electrode Surface from transient induced Molecular electronic Signal (TIMES). *Scientific Reports,* 9, 1-10, 2019. The dissertation author contributed the work evenly as co-author.

Chapter 3

Protein-Ligand Interaction Measurement

3.1 Introduction

Determining the binding affinity between proteins and ligand molecules is essential for drug discovery and studies of bio-chemical reactions[33-34]. To obtain such important information, numerous techniques have been developed to measure the dissociation constant (K_D) for protein ligand reactions, including sur-face plasmon resonance (SPR)[35-38], isothermal calorimetry (ITC)[39-41], fluorescence resonance energy transfer (FRET)[42-44], biologically modified field-effect-transistors (BioFET)[45-48] and electrophoretic mobility shift assay (EMSA)[49-51]. However, these existing techniques have their limitations. The SPR and BioFET techniques measure reactions with surface immobilized ligands, affecting the reaction entropy and 3D configurations of protein. Also, the effects of surface steric hindrance as well as molecular transport from solution to surface can affect both the kinetics and thermodynamics of the reaction[27-28]. For FRET, the fluorescent labeling of molecules could interfere with the active sites of the molecules, thus disrupting interactions with small molecules[52]. Also, the chemistry of FRET pairs imposes constraints and adds costs to the reactions. For EMSA, it requires labeling and detects mobility change of the molecules under an

external electric field. The non-equilibrium state of molecules during the electrophoretic process could result in underestimating of the binding affinity[53]. To eliminate molecular labeling and immobilization, ITC has become a commonly used technique to characterize protein-ligand interactions by measuring reaction heat. Nevertheless, ITC is a slow technique with relatively low throughput, and consumes a large amount of reagents[54]. It also has difficulties in detecting non-covalent complexes exhibiting rather small binding enthalpy.

Some time ago, we invented the method of transient induced molecular electronic signal (TIMES) to measure protein-ligand reactions in a label-free and immobilization-free manner[29-30]. In the TIMES technique, the reaction occurs in solution, and the reaction products are brought to an electrode surface via a microfluidic channel. The molecular constituents in the laminar flow approach the electrode by diffusion and induce changes in the surface charge on the electrode surface, generating a transient current that is amplified by a transimpedance amplifier connected to the electrode. By analyzing the transient current signal, the TIMES technique has shown the ability of measuring reaction K_D. Like the ITC technique, the TIMES method measures the quintessential K_D for reactions in solution. It also has the advantages of high throughput and low reagent consumption in a microfluidic environment. However, later studies found the analysis of transient current signals can suffer from reproducibility problems due to signal-to-noise limits, amplifier bandwidth limit, and external interfaces (e.g. syringe pumps or control valves). Another limit is that the mathematical model used to extract K_D is based on the assumption of superposition, which means the surface concentration of one constituent is not affected by the surface concentration of another constituent. This condition is met only when the overall surface concentration is low or the dwelling time for each molecule (i.e. the amount of time the molecule is in contact with the electrode surface) is short. Otherwise, the measured reaction K_D can be erroneous. To overcome this limit, in this paper we have modified the TIMES method by (a) integrating the current signal to obtain the change of surface charge density relative to the sur-face charge in contact with a reference buffer and (b) measuring the signal when the temporarily adsorbed molecules leave the electrode surface instead of approaching the electrode surface.

The former removes the effect of current fluctuations and results in excellent signal-to-noise ratio. The latter improves the measurement reproducibility and controllability since the measurement is made during buffer wash when no molecule of interest is present in the flow, a condition we can confidently establish and repeat. In addition, by measuring only the adsorbed molecules leaving the electrode surface (i.e. a reversible process), the current method is no longer affected by any residual irreversible reactions occurred between the surface and our molecules of interest. Finally, without analyzing the transient current, the physical model can be simplified without the assumption of superposition. In fact, one can obtain K_D by visualization of the data without going through detailed models, making the method more intuitive and user friendly. To distinguish the method from the previous approach, we name the method presented here i-TIMES.

3.2 Experimental setup and procedures

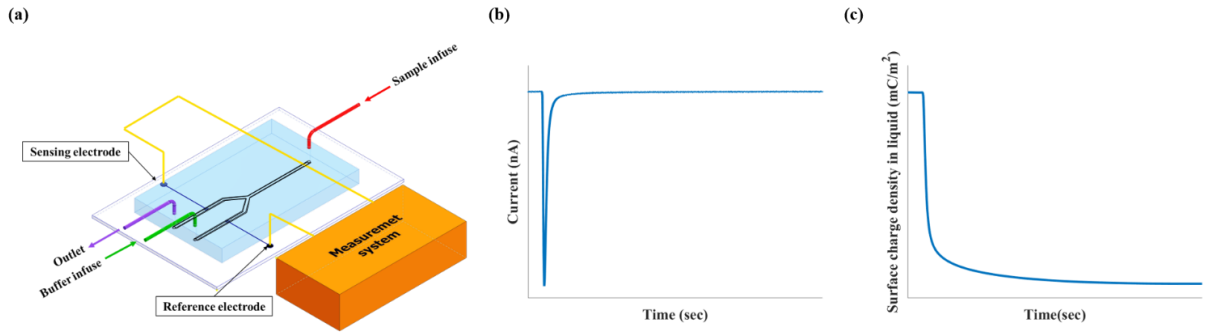

Figure 3.1. (a) Schematic of device design and i-TIMES setup. (b) A typical i-TIMES signal produced by displacing the bio-sample with a reference buffer over the sensing electrode. (c) The surface charge density versus time after integration of the current signal.

The i-TIMES system setup is shown in Figure 3.1a. Two Pt electrodes, one being sensing electrode and another being reference electrode, are in each branch of a Y-shaped microfluidic channel. Each Pt electrode has an area of 1x1 mm2 and each branch of the Y-shaped microfluidic channel is 1 mm wide and 30μm high, made of PDMS bonded to a glass substrate where the Pt electrodes are fabricated. The two electrodes are connected to the inputs of a transimpedance amplifier (TIA) that turns the current signal into

a voltage output. The output voltage of the TIA is amplified by a voltage amplifier and digitized by a data acquisition board (DAQ). By reversing the above signal path, one can find the actual magnitude and polarity of current signal induced by the molecules near the sensing electrode. By integrating the current signal over time, the surface charge induced by the molecules is obtained.

We used the following procedure to conduct the experiment. At first, we filled both branches of microfluidic channels with reference buffer (1X PBS, pH = 7.41). Then the reference buffer in the channel with the sensing electrode is replaced by the solution containing the molecules under test (i.e. ligand and/or protein). The pH value of the solution was adjusted to assure that in all tests with different molecular concentrations, the pH value of the solution remains the same. This step is important in order to remove the pH effect from the i-TIMES signal. The sensing electrode was soaked in the solution for 3 minutes to reach equilibrium between the molecules in the solution and the molecules on the electrode surface. Then we displaced the solution above the sensing electrode with reference buffer (1X PBS, pH =7.41). The current signal was measured during this "washing" process. Such current signal was produced by washing off the molecules that were adsorbed to the electrode surface or in close proximity (within the Debye length) to the electrode. Therefore, the integrated current signal during the washing process results from the change of surface charge induced by molecules that move away from the sensing electrode, subtracted by ions that take the place left by the departing molecules. The typical current signal and surface charge density from the above procedure are shown in Figure 3.1b and 3.1c. Here we are most interested in the change in surface charge represented by the equation shown in below:

$$\boldsymbol{Q_T = \int_0^t I(\tau) d\tau = Q_{sample} - Q_{reference}} \quad (1)$$

where Q_T is the charge density integrated from the current signal, Q_{sample} is the surface charge in the double layer of the sample solution and $Q_{reference}$ is the corresponding quantity for the reference buffer.

In the following we report a series of tests using various protein ligand pairs to assess the performance and feasibility of the i-TIMES method. We also design negative control experiment with non-reacting protein and ligand. For all the measurements reported in the paper, we first measure the dependence

of sur-face charge density on the protein concentration and ligand concentration separately. Then we measure the surface charge density when the protein and ligand are mixed with a 1:1 ratio. To assure reaction equilibrium, all protein ligand mixture solutions are left for 2 hours with gentle agitation before test. In all the measurements, we keep the pH value of the solution constant (within±0.01), which can be done by adding a very small amount of NaOH or HCl in the solution with negligible effect on the ionic strength of the solution.

All experimental data presented in this paper as well as the results in our earlier publication show the surface charge signal have piecewise linear dependence on the logarithmic molecular concentration[55]. The slope of the curve and the turning point(s) of the piecewise linear curve contain important information about the molecular behaviors on the electrode surface, which we will use to determine the K_D. We can treat the slopes and the turning points between sections of different slopes as the fingerprint of each type of molecule. When two reacting molecules are mixed in a 1:1 ratio and the equilibrium state is established, a significant amount of the protein-ligand complex is formed if the initial concentration of each molecule is near or above the K_D. Simple analysis shows that if the initial protein and ligand concentration is close to K_D, the complex:protein:ligand volume concentration ratio is approximately 7:4:4. The presence of significant amount of “new” molecule (i.e. protein-ligand com-plex) gives rise to different slopes and turning points for the piecewise linear curve of surface charge density, from which one can directly find the K_D.

3.3 Results and discussions

Measurements with lysozyme, TriNAG and their mixture

Lysozyme is an antimicrobial enzyme that forms part of the innate immune system. TriNAG is an inhibitor which binds to the active site of lysozyme with a dissociation constant of 10-30 µM according to literatures[30, 56-57]. Fig. 3.2a and 3.2b show the lysozyme measurement in the concentration range from 200uM to 0.3nM. Fig. 3.2c is the integral of signal for each concentration from Fig. 3.2a and 3.2b. Each data shown in Fig 3.2c is average of 3 measurements, and the deviation is nearly Indistinguishable, showing the excellent repeatability. The piecewise linear characteristic is shown clearly in Fig. 3.2c, two turning points are observed at around 10nM and 90uM, respectively.

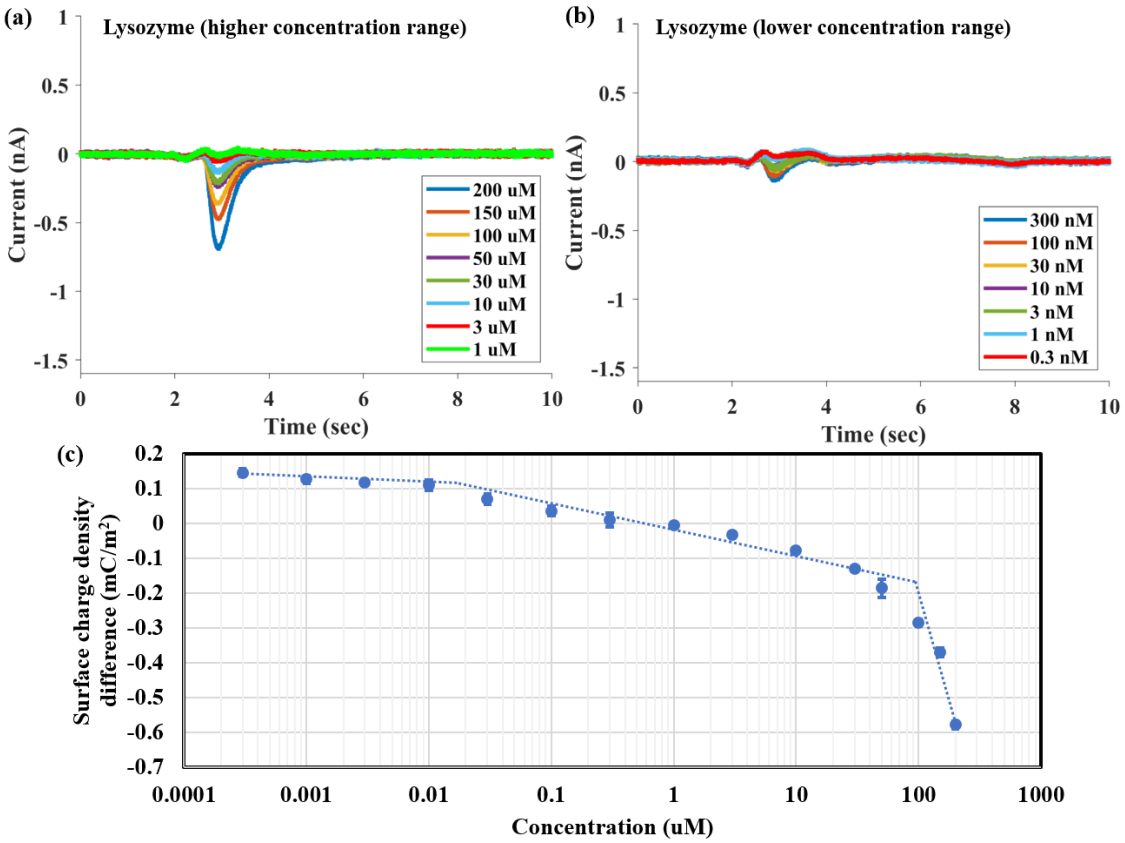

Figure 3.2. i-TIMES signal of (a) lysozyme (higher concentration), (b) lysozyme (lower concentration) and (c) dependence of surface charge density on lysozyme concentration (blue). The error bars show the range of 3 measurements.

A similar characteristic is observed for TriNAG measurement. Fig. 3.3a and 3.3b show the current signal of TriNAG and 1:1 Lysozyme/TriNAG mixture, and Fig. 3.3c shows the integral signal for Lysozyme, TriNAG, and mixture. Again, all curves show piecewise linear characteristics. Compared to the data with Lysozyme alone and TriNAG alone, the curve for mixture shows a distinct turning point at 10uM, which is close to the KD of the reaction.

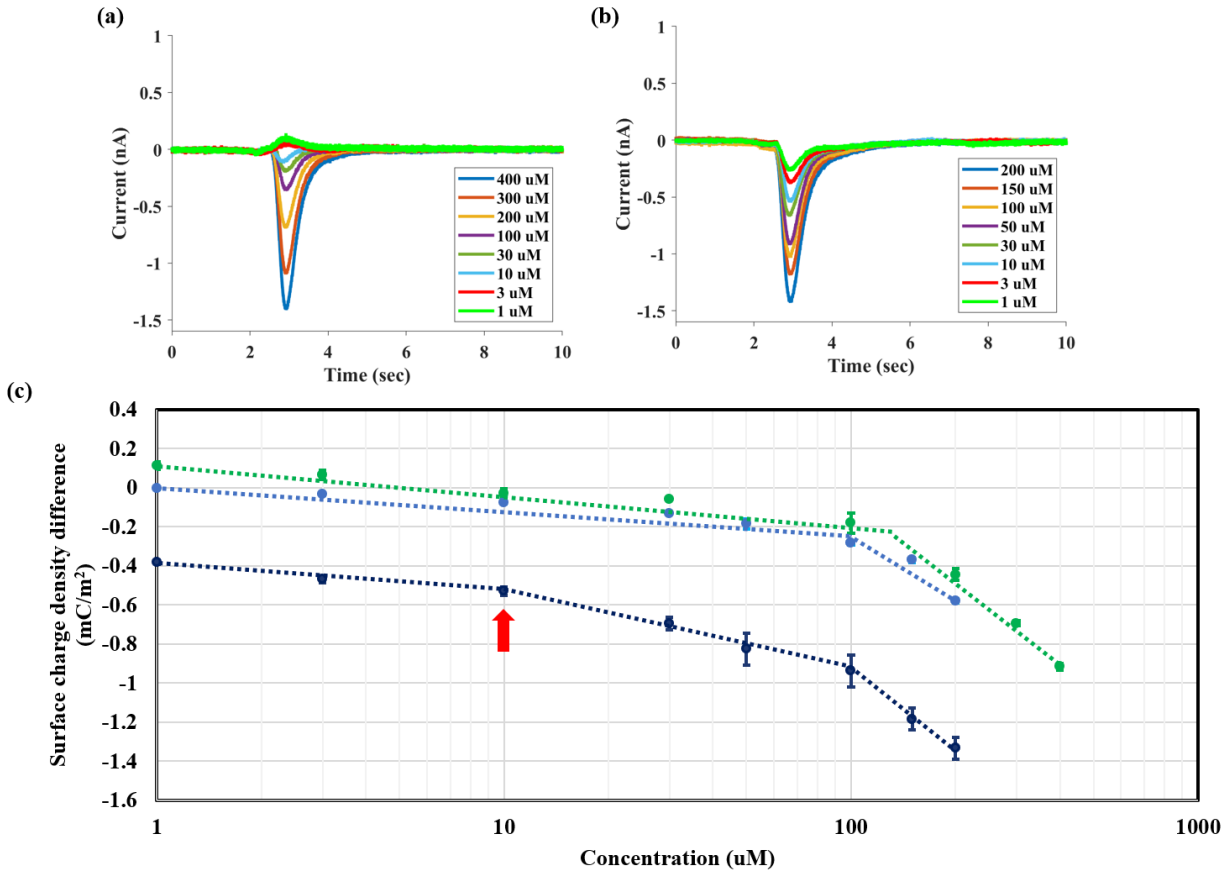

Figure 3.3. i-TIMES signal for (a) TriNAG, (b) 1:1 mixture of TriNAG and lysozyme. (c) Surface charge density of Lysozyme (blue), TriNAG (green) and the TRiNAG/Lysozyme 1:1 mixture (dark blue). The red arrow indicates the turning point that is approximately equal to the reaction dissociation constant KD.

Measurement with lysozyme, aptamer, and their mixture

In another experiment, we applied the i-TIMES method to measure protein-aptamer interaction. Aptamers are single-stranded oligonucleotides that can be folded into unique conformations and show high binding affinity to specific target molecule. Using aptamers as ligands for target proteins can be attractive because aptamers can work with a wide range of targets, have high binding affinity and stability, and are easy and inexpensive to produce by polymerase chain reaction (PCR). Literatures have shown several aptamers can react with lysozyme[58]. In our experiment, we use the aptamer sequence GCA GCT AAG CAG GCG GCT CAC AAA ACC ATT CGC ATG CGG C for lysozyme binding, which is reported to produce a K_D of around 3nM.

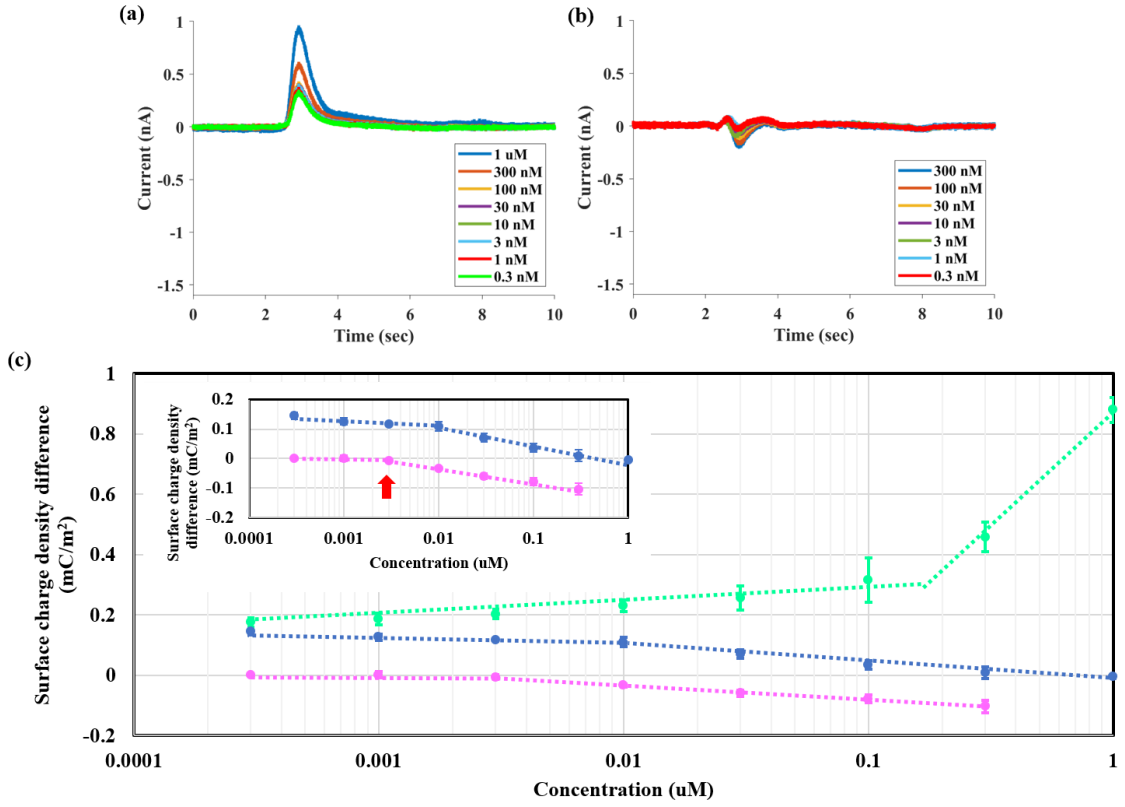

Figure 3.4. i-TIMES signal of (a) Aptamer molecule and (b) 1:1 mixture of aptamer and lysozyme. (c) Surface charge density of Lysozyme (blue), Aptamer (light green) and 1:1 mixture of aptamer and lysozyme (pink). The inset shows the detailed surface charge density of lysozyme (blue) and 1:1 mixture of aptamer and lysozyme (pink). The red arrow indicates the turning point that is approximately equal to K_D.

Fig. 3.4a and 3.4b show the aptamer and 1:1 Lysozyme/aptamer mixture signal curve, and Fig. 3.4c shows the charge density with lysozyme alone, aptamer alone, and mixture curve. A notable feature can be observed that the aptamer curve is totally different from the other two curve. Aptamer is negative charged, so the sign of charge is not the same as lysozyme. For the curve of mixture, the trend is close to the curve of lysozyme alone, which is significantly different from the curve of aptamer, showing that the charge property of mixture changed. In the closer look at mixture curve, in the insert plot of Fig. 3.4c. a turning point can be observed, which is located at around 3nM and is close to the KD value for lysozyme and aptamer interaction.

Measurements with lysozyme, pABA and their mixture for negative control

A negative control is performed. The molecule p-aminobenzamidine (p-ABA) is chosen as non-reactive ligand with lysozyme. Fig. 3.5a and 3.5b show the signal for p-ABA alone and 1:1 p-ABA/lysozyme mixture measurement. With the same strategy to plot the charge density with concentration cure, as shown in Fig. 3.5c, the curve for mixture is very close to the curve of lysozyme alone. The additional turning point or slope changing is absence in mixture curve, indicating the lack of new molecules produced with this reaction. This result shows no interaction between lysozyme and p-ABA.

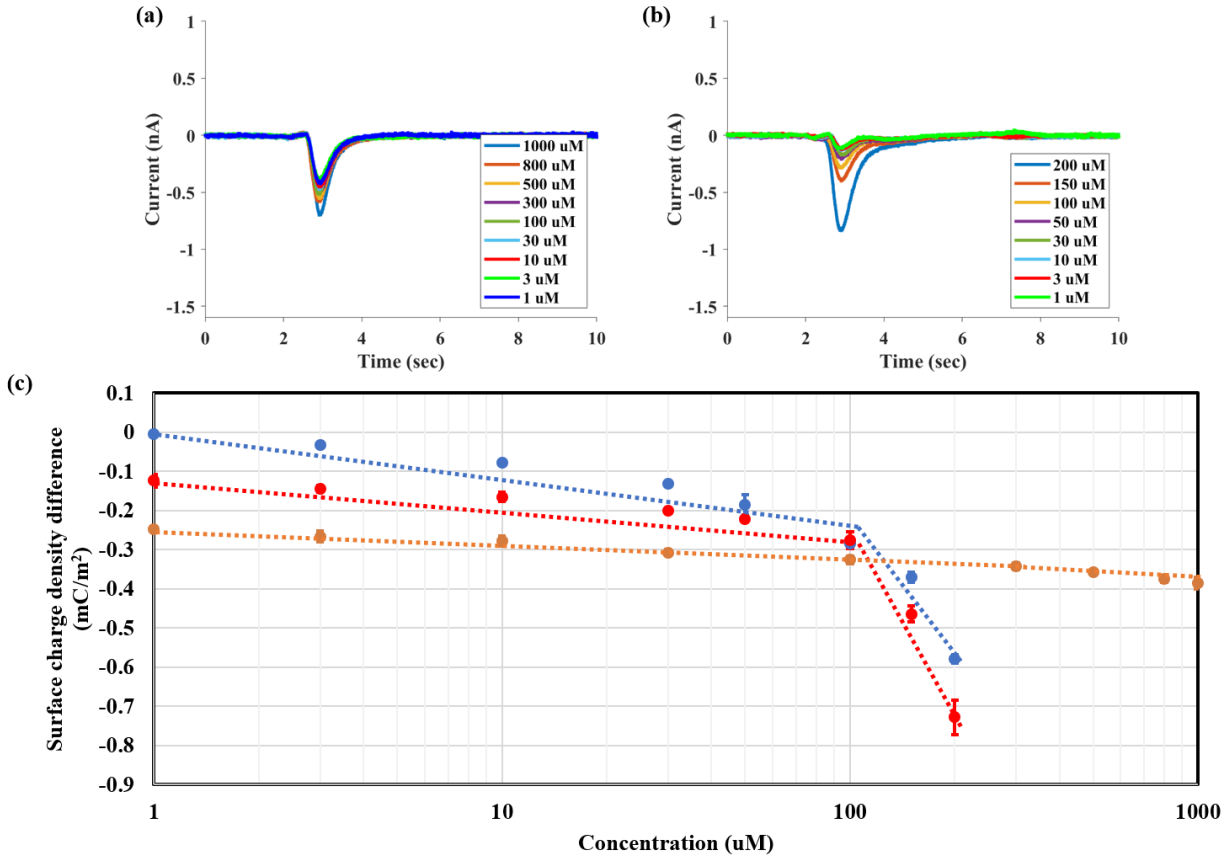

Figure 3.5. i-TIMES signal of molecule (a) pABA (b) its complex with Lysozyme. (c) Surface charge density of Lysozyme (blue), pABA (orange) and its complex (red).

Measurements with RNaseA, 3'-UMP and their mixture

In another experiment to demonstrate the utility of i-TIMES technique for label-free detection of molecular interactions, we characterized the reaction of RNaseA and its ligand. RNaseA plays an important role in cleaving single-stranded RNA and its property as an enzyme has been studied extensively. The dissociation constant K_D between RNaseA and its ligand, 3'-UMP, has been reported to be 9.7±0.9 μM[59].

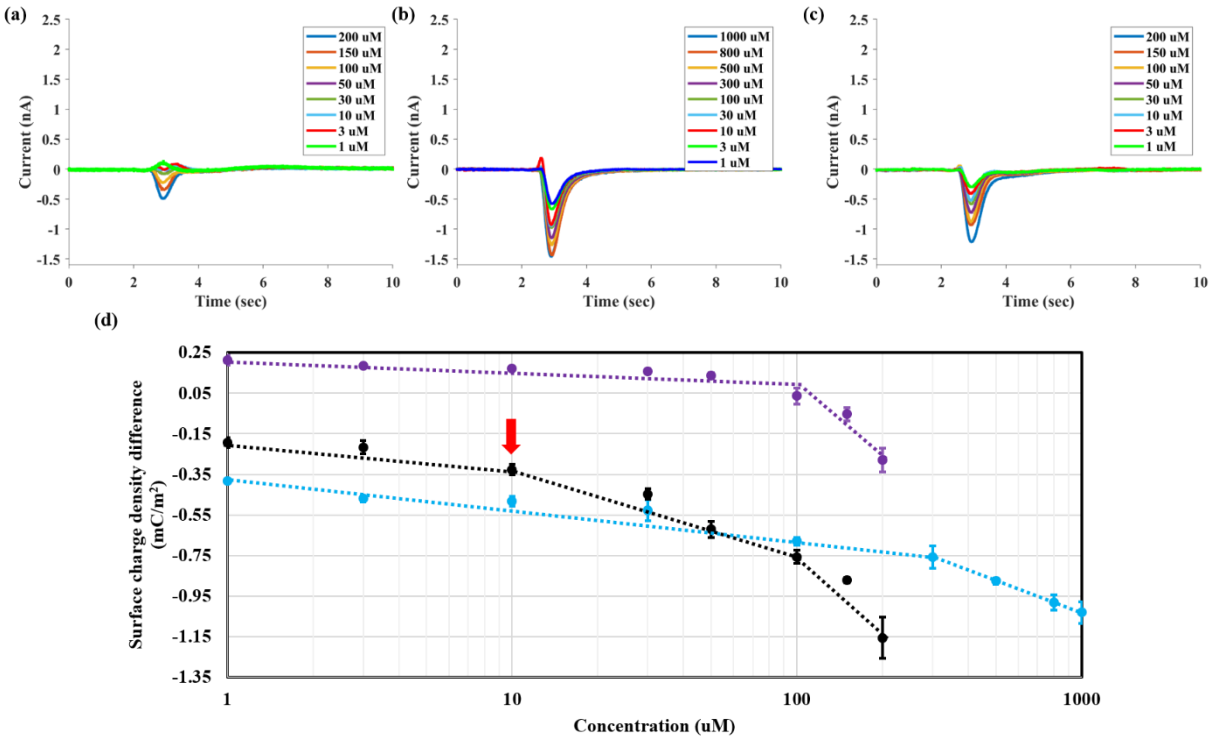

Figure 3.6. i-TIMES signal of molecule (a) RNaseA, (b) 3'-UMP, (c) its complex. (d) Surface charge density of RNaseA (purple), 3'-UMP (light blue) and its complex (black). The red arrow indicates the turning point at the concentration of K_D value.

Fig. 3.6a, 3.6b, and 3.6c show the signal for RNaseA alone, 3'-UMP alone and 1:1 RNaseA/3'-UMP mixture. The integral charge versus concentrations for each sample measurement is plot in Fig. 3.6d. As the same characteristic observed earlier, the piecewise linear relation can be seen. From Fig. 3.6d, an additional turning point is shown, and it is located around at 10uM, which is very close the K_D value for RNaseA and 3'-UMP interaction.

3.4 Physical model of i-TIMES

In this section we propose a physical model to describe the piecewise linear characteristics of surface charge density and molecular concentration in logarithmic scale. We stress that the measured current signal comes from the mobile charge that leaves the electrode surface during washing. These mobile charges, present in the so-called double layers at the electrode liquid interface, are established when the

electrode in the microfluidic channel is immersed in the solution that contains the molecule. When the solution is displaced by the washing buffer, a new equilibrium state between the washing buffer and the electrode is established and the motions of charges in the double layer to establish the new equilibrium state gives rise to the current signal. When integrated, we obtain the total amount of change in surface charge.

We assume that when the electrode is immersed in the solution containing a given kind of molecule, the surface concentration, n_s, and the volume concentration, n, of the molecule follow the relation,

$$\boldsymbol{n_s = \left(\frac{k_a}{k_d}\right) n e^{-q\zeta/kT}} \quad (\mathbf{2})$$

Where k_a and k_d are the adsorption and desorption coefficients of the molecule at the electrode surface, ζ is the zeta potential, k is Boltzmann constant, T is absolute temperature, and q is the "effective charge" of the molecule. Here effective charge can be different than the actual charge of the molecule in the buffer due to (partial) charge screening (meaning the molecule is "dressed" by ions around it) and the local change in the pH value. Since proton distribution near the liquid/electrode interface is affected by the potential profile within the Debye length, the molecule at the electrode surface could experience a different local pH value and subsequently, a different charge than it does in the bulk. All these effects determine the effective charge of the molecule near the electrode surface. We further hypothesize that the zeta potential is affected by the surface charge density according to Equation (3),

$$\boldsymbol{\zeta = \zeta_o - \frac{1}{C_T} Q_T} \quad (\mathbf{3})$$

Where Q_T is the change in surface charge, the quantity we measure as i-TIMES signal. C_T is the effective capacitance experienced by Q_T. Equation (3) can also be viewed as the first term in the Taylor series expansion of zeta potential over the surface charge density. Physically, we can represent C_T by the series of two capacitances, the capacitance associated with the Debye length and the capacitance due to the (partial) layer deposition of the molecule.

$$\frac{\mathbf{1}}{\boldsymbol{C_T}} = \frac{\mathbf{1}}{\boldsymbol{C_D}} + \frac{\mathbf{1}}{\boldsymbol{C_M}} \sim \frac{\mathbf{1}}{\boldsymbol{C_M}} \quad (\mathbf{4})$$

We can write $\frac{\mathbf{1}}{\boldsymbol{C_D}} = \frac{\boldsymbol{L_D}}{\boldsymbol{A\epsilon_o\epsilon_{H2O}}}$ (A: area of electrode, $\boldsymbol{L_D}$: Debye length, $\boldsymbol{\epsilon_o}$: permittivity in vacuum, and $\boldsymbol{\epsilon_{H2O}}$: dielectric constant of water) and $\frac{\mathbf{1}}{\mathbf{C_M}} = \frac{\mathbf{d_M}}{\mathbf{A_M\epsilon_o\epsilon_M}}$ (AM: effective area covered by the molecule, $\mathbf{d_M}$: effective thickness of the molecular deposition, and $\boldsymbol{\epsilon_M}$: dielectric constant of molecule). For typical ionic strength of the buffer, $\mathbf{C_D} \gg \mathbf{C_M}$, thus leading to the approximation in (4). We can further model $\mathbf{C_M}$ as below

$$\mathbf{C_M} = \mathbf{C_{Mo}}[\boldsymbol{\alpha}\,\mathbf{u}(\mathbf{n_{th}} - \mathbf{n}) + \boldsymbol{\beta}\mathbf{u}(\mathbf{n} - \mathbf{n_{th}})] \quad \textbf{when} \quad \mathbf{n} > \mathbf{n_o}$$

$$= \boldsymbol{\alpha}\mathbf{C_{Mo}}\left(\frac{\mathbf{n}}{\mathbf{n_o}}\right) \quad \textbf{when} \quad \mathbf{n} < \mathbf{n_o} \quad (\mathbf{5})$$

Where $\mathbf{C_{Mo}} = \frac{\mathbf{A\epsilon_o\epsilon_M}}{\mathbf{d_M}}$ is the capacitance of adsorbed molecules over the entire area of electrode. $\mathbf{n_o}$ is the concentration above which the linear relation between the surface coverage and the molecular concentration ceases to hold. In most of our measurements, the molecular concentration is actually greater than $\mathbf{n_o}$. $\mathbf{u}$ is the unit step function. $\mathbf{n_{th}}$ denotes the threshold molecular volume concentration above which the capacitance $\mathbf{C_M}$ experiences a sudden change from $\boldsymbol{\alpha}\mathbf{C_{Mo}}$ to $\boldsymbol{\beta}\mathbf{C_{Mo}}$likely due to molecular structural change on the electrode surface (e.g. protein denature or collapse on the metal surface).

Separately, we approximate the relation between $\mathbf{Q_T}$ and the surface molecular concentration with Equation (6),

$$\mathbf{Q_T} = \mathbf{q'n_s}\left(\mathbf{1} - \frac{\mathbf{n_s}}{\mathbf{n_{sa}}}\right) \quad (\mathbf{6})$$

Where $\boldsymbol{q'}$ is the change in the surface charge due to departure of a single molecule from the electrode surface. The value or even the sign of $\boldsymbol{q'}$ can be different from the actual charge because ions may take the place left by the molecule and the value of $\boldsymbol{q'}$ depends on the ionic strength, buffer concentration, and pH value of the solution besides the charge of the molecule itself. In other words, $\boldsymbol{q'}$ may not be zero even for a charge neutral molecule. Here we introduce a parameter, $\boldsymbol{n_{sa}}$, above which the sign of the signal may even change. Part of the reason is that even though we control the pH value of the solution to be constant for solutions of different molecular concentration, the actual pH value (i.e. proton concentration profile) near the electrode surface is affected by the zeta potential. As zeta potential changes, the "local" pH value changes and this can alter the magnitude and even polarity of the charge contained by the molecule. Hence, we introduce an empirical relation in Equation (6) to model this effect. Later on, we will find that the detailed relation in Equation (6) will not affect our ability to fit the experimental results.

From Equations. (2) and (3), we have

$$\mathbf{n_s = \left(\frac{k_a}{k_d}\right) n e^{-q\zeta_o/kT} e^{qQ_T/C_T kT}} \quad (7)$$

The relation between the surface charge at two volume concentrations can be represented as

$$\mathbf{\log\left(\frac{n_2}{n_1}\right) = \log\left(\frac{n_{s2}}{n_{s1}}\right) - 0.434\frac{q}{kTC_T}(Q_{T2} - Q_{T1})} \quad (8)$$

From Equation (6), $\boldsymbol{Q_T \sim q' n_s \; if \; n_s \ll n_{sa} \quad and \quad Q_T \sim -q'\frac{n_s^2}{n_{so}} \quad if \; n_s \gg n_{sa}}$. Therefore,

$$\mathbf{\frac{n_{s2}}{n_{s1}} \sim \frac{Q_{T2}}{Q_{T1}} \;\; if \; n_{s1,2} \ll n_{sa} \quad or}$$

$$\mathbf{\frac{n_{s2}}{n_{s1}} \sim \sqrt{\frac{Q_{T2}}{Q_{T1}}} \;\; if \; n_{s1,2} \gg n_{sa}} \quad (9)$$

Substituting Equation (9) into Equation (8), we obtain

$$\log\left(\frac{n_2}{n_1}\right) = -0.434\frac{q}{kTC_T}(Q_{T2} - Q_{T1}) + \frac{1}{\gamma}\log\left(\frac{Q_{T2}}{Q_{T1}}\right) \quad (10)$$

where $\gamma = 1$ if $n_{s1,2} \ll n_{sa}$ and $\gamma = 2$ if $n_{s1,2} \gg n_{sa}$.

Since the $log\left(\frac{Q_{T2}}{Q_{T1}}\right)$ term is much smaller and changes much slowly than the $(Q_{T2} - Q_{T1})$ term unless the value Q_{T1} and Q_{T2} are both very small, we can ignore the second term in most cases of our measurements. Then Equation (10) can be reduced to Equation (11) using the relation in Equation (5),

$$\frac{Q_{T2} - Q_{T1}}{\log\left(\frac{n_2}{n_1}\right)} \cong -\alpha\frac{kTC_{Mo}}{2.3q} \equiv P_\alpha \text{ when } n_o < n_{1,2} < n_{th} \quad (11a)$$

$$\frac{Q_{T2} - Q_{T1}}{\log\left(\frac{n_2}{n_1}\right)} \cong -\beta\frac{kTC_{Mo}}{2.3q} \equiv P_\beta \text{ when } n_{1,2} > n_{th} \quad (11b)$$

The model describes the piecewise linear characteristics between the surface charge density change and the logarithmic concentration.

To summarize, in a semi-empirical model, we can describe the general behaviors of the i-TIMES signal over a wide concentration range. For each kind of molecule, its i-TIMES signal can be depicted by a set of parameters: $P_\alpha, P_\beta, n_{th}$. The turning point of piecewise linear curve occurs at the concentration n_{th}. All three key parameters in the model can be directly obtained experimentally and are summarized in Table 3.1. When a new type of molecule is present in a significant amount, its features appear in the i-TIMES and are most distinctly represented by the turning points, enabling us to tell the dissociation constant

directly from the i-TIMES signal. Finally, observing the ratio of the slopes $\boldsymbol{\gamma = \frac{P_\beta}{P_\alpha}}$ in Table 3.1, we find that the slope ratio, $\boldsymbol{\gamma}$, is related to the molecular weight or the size of the molecule. Larger molecules tend to have a greater value of $\boldsymbol{\gamma}$, which seems to suggest that when denatured or collapsed to the electrode surface, the effective thickness of the molecule, $\boldsymbol{d_M}$, decreases and the effective dielectric constant, $\boldsymbol{\epsilon_M}$, increases, causing significant increase in the capacitance in Equation (5). Future work with molecular dynamic simulations may provide insight for this interesting trend that seems to provide a good intuitive explanation for the experimental observations from the i-TIMES data.

Table 3.1. Parameters of each molecule obtained from i-TIMES measurements

Molecule	Molecular weight (Da)	P_α (mC/m²)	P_β (mC/m²)	$\gamma = \frac{P_\beta}{P_\alpha}$	n_{th} (μM)	n_{sa} (μM)
Lysozyme	14300	-0.09	-1.14	12.67	93.41	0.50
TriNAG	627	-0.15	-1.14	7.60	103.18	5.33
pABA	135	-0.035	-0.11	3.14	325.75	$5.71*10^{-8}$
Aptamer	18587	0.035	0.59	16.86	0.1143	$1.01*10^{-8}$
RNaseA	13700	-0.035	-1.06	30.29	92.08	120.59
3'UMP	322	-0.16	-0.58	3.63	278.77	0.0058

3.5 Conclusions

By integrating the transient induced molecular electronic signals, we have demonstrated the i-TIMES technique for label-free, immobilization-free detection of protein-ligand interactions to measure the reaction KD. To evaluate the viability of the technique, we have used lysozyme protein with TriNAG and aptamer ligands for positive control and pABA for negative control and used RNaseA and 3'UMP as another set of protein-ligand pair. The results show the existence of clear features in the i-TIMES signal at

concentrations that are very close to the reaction KD. We have also developed a semi-empirical model to elucidate the physical process giving rise to the i-TIMES signal.

Overall, our results indicate that the i-TIMES technique is highly sensitive to the physical and chemical properties of large and small molecules and each type of molecule can produce a unique footprint in its i-TIMES signal. Although the work is exploratory, the results we have demonstrated are highly encouraging and there are evidences that i-TIMES signal contains rich information awaiting us to decipher. Technologically, i-TIMES provides an accurate and convenient tool for quantitative study of molecular interactions without molecular labeling or immobilization. The technique can be attractive to many applications including drug discovery.

3.6 Acknowledgement

Chapter 3 is a reprint of the material as it appears in *Analytical Chemistry* 2020, Ping-Wei Chen, Chi-Yang Tseng, Fumin Shi, Bo Bi, Yu-Hwa Lo. Detecting Protein–Ligand Interaction from Integrated Transient Induced Molecular Electronic Signal (i-TIMES). *Analytical Chemistry,* 92 (5), 3852–3859, 2020. The dissertation author contributed the work evenly as co-author.

Chapter 4

Paper-Based TIMES Measurement

4.1 Introduction

Paper-based analytical devices (PAD) have attracted attention in recent years, especially in the area of point-of-care (POC) clinical diagnostics, owing to several advantages including low cost, simple operation, low sample consuming, and disposability.[60] Variety of fabrication techniques were developed to expand the utilization of paper-based devices in environmental monitoring, biomedical applications, and applications in the energy sector, showing high potential in being an alternative sensor device[61-62].

Detection is an important consideration in the development of PADs, especially in clinical diagnostics studies - the high accuracy of target detection is always one of the first priorities. Colorimetric readout is the most common method used for qualitative or quantitative measurement.[63] The chemical reaction on paper is accompanied with the color change, and it is proportional to the quantity of the chemicals that are present on the paper. However, colorimetric readout is limited by its low sensitivity. The poor sensitivity is attributed to the uneven colorimetric distribution of substance and background noise coming from the environment illumination, leading the result to be prone to fault.

Electrochemical readout provides an alternative method for PAD detection. The first electrochemical PAD was developed by Whitesides *et al.* in 2007[64], and more related works were developed subsequently[65-67]. The redox active compound, such as metals[68-69] and redox active small molecules[70], can be directly detected by chronoamperometry[65, 67] or variety of voltammetry measurements, such as the anodic stripping voltammetry (ASV)[71] and square wave voltammetry are commonly used[72]. Detection of analytes that are not redox active can be done with potentiometry measurement, such as ion selective sensing[73].

Biomedical detections are getting more attention because of the interest in enzymatic reactions. Enzymatic detection is based on the detection of an electroactive enzymatic by-product or redox mediator to quantify the presence of targeted material. The concept of utilization of electrochemical detection in enzyme-linked immunosorbent assays (ELISAs) was first introduced by Li et al. in 2010[74]. The detection of antibody-antigen binding events is based on the redox of conjugated enzyme on the reporter molecule[75], in which the charge transfer generated along with the presence of enzyme active product. Most enzymatic reactions generate current and can be detected through chronoamperometry measurement[76], and still other types of voltammetry are used to improve the sensitivity[70].

The elements of paper-based devices include not only paper substrate, but also embedded electrodes for detection. Most recent studies focus on the strategy of improving fabrication of the electrode to improve analyte detection. The strategies rely on fabricating electrodes that are patterned on the paper by using such techniques, screen printing[77], inject-ink printing[78-79] or metal sputtering[80]. In the current strategy for target detection, the interested analytes are needed to be immobilized on the electrode surface, leading the consequence for selecting material of electrode and chemical reaction of immobilization are taken into considerations. Those limitations reduce the scope of application for electrochemical PAD.

Instead of the usual amperometry or voltammetry measurement, we present a novel paper-based electrochemical detection method that directly measures analyte reaction without any electrode modification or complicated process, which improves the limitations from previous measurement methods.

This feasible measurement is done by directly measuring a chemical reaction on pre-wetted paper, which is directly attached to a metal electrode where the current response can then be directly recorded in real time. As the paper is made of cellulose fibers, the crossed-stacked and interconnected structure provides not only flexibility but also mechanical stability[61-62]. The porous structure of paper is considered an ideal medium for analyte molecules contained in the water phase. A thin liquid layer formed in the pre-wetted paper-to-electrode interface offers a pass for the analyte molecule to deliver through the porous structure of paper to the electrode surface. The analyte can then be detected by current response, and the current is amplified by the external equipment.

We present our work by studying amino acid detection under ninhydrin reaction, and IgG detection through antibodies binding reaction. These two well-known reactions have been applied to many techniques; however, they have seldom been studied in the field of paper-based electrochemical reading. Here, we present those reactions not only because they are the most commonplace form of study, but also to introduce the possibility of novelty in future applications.

The most common amino acid detection is through a ninhydrin reaction - producing Ruhemann's purple in the process - commonly used in protein chromatography and fingerprint detection. In our study, we recorded the electronic response that occurred when binding ninhydrin with varying amino acid concentrations. Without any manipulation of the electrode, we established a consistent trend based on the various concentrations that we used.

IgG is the most common biomarker used for clinical diagnostics, where extensive studies have been developed for a variety of research areas, especially used for lateral flow assay (LFA)[63]. In our work, the Goat-antibody and Goat-IgG were used as an example to demonstrate the antibody binding interaction. The binding event that occurs on paper can be directly recorded with current response without immobilization of the antibody on the electrode surface or the use of a blocking reagent that is presented in ELISA base measurement. Here, we reduce the elaborate work on electrode fabrication, since the reaction is directly

measured by using disposable paper. Besides, no immobilization or modification of the electrode is needed during the measurement. The kinetics analysis is developed in our methodology, along with a comparison with surface plasmon resonance (SPR) analytics. This immobilized free detection method provides a kinetic study which introduces a much more feasible and portable way for further applications, with an especially high potential towards an alternative readout for LFA detection.

4.2 Results and discussions

Experiment setup

Fig. 4.1(a) Shows the overall setup of paper-based TIMES system. The two Pt electrodes are sputtered onto the glass slide, one serves as reference electrode, the other serves as sensing electrode. These two electrodes are circular shape with 4mm diameter, and the extended wire of each electrode is connected to inputs of transimpedance amplifier (TIA, SR-570, Stanford Research system, Inc, USA), in which the input current signal will be transferred into voltage output. The output voltage signal then be amplified by amplifier and digitized by the connected data acquisition board (DAQ, USB-6251, National Instrument, USA). The digitized signal is recorded by LabView Signal Express.

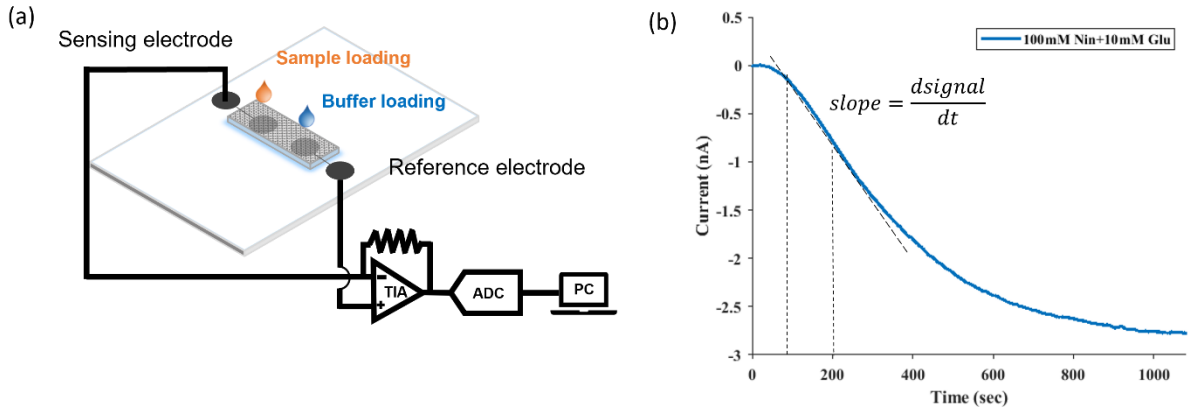

Figure 4.1. (a) Setup for paper-based TIMES measurement (b) TIMES current response waveform.

When conducting the measurement, the 5X20mm^2 filter paper is placed on the glass substrate and cover the electrodes. The chosen of filter paper for measurement is important, because the absorbance of water for paper would affect the measurement. Specifically, we use 750um thick blotting paper (Whatman® gel blotting paper) and 180um 3MM-chromatography filter paper (Whatman® cellulose chromatography paper) for Ninhydrin reaction measurement and antibody affinity measurement respectively, since these two types of paper provide good water absorbance and ideal thickness.

The reactant solution or buffer that is compatible with the solution used to store analyte targets then add onto the paper so that the paper is soaked. To have a better control of wettability of paper, the volume of added reactant solution or buffer is fixed to the same amount and that amount saturates the paper enough to form a thin liquid layer. The thin film liquid phase is established around the paper and between the interface of the electrode surface, so the analyte of the molecule can be delivered to the electrode surface and the reaction can be sensed. The data is recorded when a sample/analyte solution is added onto the paper where the sensing electrode is located, so the reaction will be recorded. On the other side, to avoid the dilution effect, the same reactant solution or buffer is added on the site of the paper where the reference electrodes are located, while no reaction occurs at this position. The current response is recorded in around 15 min, and the typical signal waveform is shown in Fig. 4.1(b). The current signal can be generated directly from the redox current due to the chemical reaction, or it can be the induced charge generated from the interface where the surface charge density near on the electrode surface is changed by the formation of complex molecules, as the previous work we have done on microfluidic TIMES measurements[29-30, 55, 81]. No matter which case is, the measured current is created from the molecular interaction event. Therefore, we can analyze the measured signal to estimate the reaction kinetics. In the typical signal curve, we can observe that around 100sec mark, the curve starts decreasing, representing the reaction occurs at electrode surface and the initial reaction rate can be determined within the first 100 to 200 sec by fitting the slope from linear fitting. The initial rate determined by the slope of measured signal can be used to represent in the simple equation shown below. A and B represent the two species of reactants in the reaction, m and n

represents the reaction order for each reactant respectively, and k is the reaction constant. The estimation of overall reaction order can be estimated under this simple form of reaction kinetic formula. If pseudo-first order reaction is considered, assuming reactant A is greater than reactant B, the first two terms in reaction formula (k and $[A]^m$), will altogether be considered as a constant.

$$Initial\ Rate\ (slope) = \frac{dSignal}{dt} \propto k[A]^m[B]^n$$

Ninhydrin reaction with Glutamine

The kinetics of Ninhydrin reaction with amino acids is overall second order, first order in ninhydrin and first order in amino acid[82-83]. Ninhydrin reacts together with amino acids to create a reaction that eventually creates the products: CO2, an aldehyde, and Ruhamann's purple. The rate determining step in the mechanism involves a non-protonated amino group causing a nucleophilic-type displacement of an OH group of ninhydrin hydrate. Overall, this leads to the requirement of two ninhydrin molecules per one molecule of amino acid to form the final product. The overall chemical reaction mechanism is shown below in Fig. 4.2. [82-84]

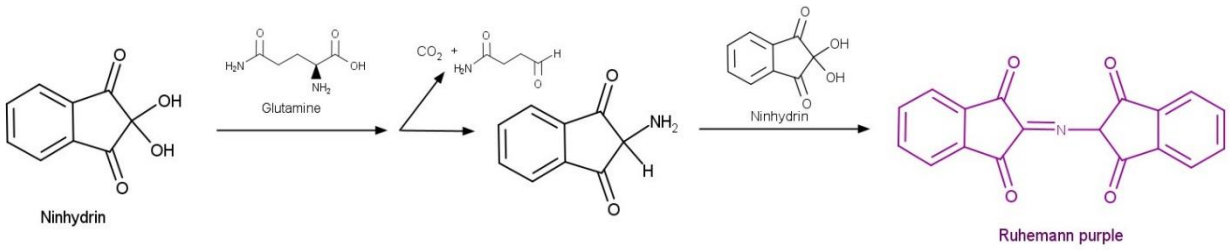

Figure 4.2. Ninhydrin reaction mechanism with amino acids.

In the measurement process of ninhydrin reaction with glutamine, the ninhydrin solution is prepared with 1X PBS from 50mM to 200mM concentrations, and glutamine solution is prepared with 1X PBS from 0.5mM to 2mM. Prior to measuring the signal, 80uL of ninhydrin solution is added to saturate

the paper. The use of paper for this measurement is 750um thick blotting paper (Whatman® gel blotting paper) because of good solution absorbent. When paper is completely soaked with ninhydrin solution, 2uL of glutamine solution is added on the site of paper where sensing electrode is located, while 2uL of 1X PBS buffer is added on the site of paper where reference electrode is located. By doing so, the dilution effect of reactant can be avoided. Since the concentration of Ninhydrin is much greater than glutamine, the pseudo-first order reaction is valid to further analysis.

The negative control experiments are performed. First of all, the ninhydrin solution is added to saturate the paper, and 2uL of 1X PBS are added on both sides of the paper. As shown in blue lines in both Fig 4.3. and Fig 4.4., the signal shows no reaction response during the buffer addition. This result provides that the dilution effect is small and can be ignored. Secondly, 2uL of 1mM glucose solution are added on the ninhydrin-saturated paper, where no reaction would occur between glucose and ninhydrin. The signal is shown as red lines in Fig. 4.3 and Fig. 4.4. The signal changes little, meaning that no reaction occurs with glucose and ninhydrin, and just molecule transportation occurs and can be sensed. This small change of signal is still too small and can be ignored. In the above experiments, the true chemical reaction response can be measured in real-time.

Two experimental sets are done with ninhydrin reaction measurement:

The first experiment was done by keeping the same concentration of ninhydrin but adding different glutamine concentration. The same 100mM ninhydrin solution is added as a base solution on paper, and the glutamine is added from 0.5mM, 0.7mM, 1mM, 1.4mM and 2mM, respectively. The overall signals are shown in Fig. 4.3. The signal starts decreasing at around 100sec, in which the glutamine molecules may transport from top to bottom of the paper and react with ninhydrin molecules which the electrodes sense the signal change. The reaction can last longer than 15min since the current response has not reached back to the original baseline, but given that the restoration back to the baseline would take a significant amount of time, we opted to have the recording duration in our measurement be only 15min. For kinetic study, the

signal from the first 100-200sec was selected to calculate the initial rate, and the pseudo first order reaction is considered. The slope within this 100sec was fitted by linear fitting, and the reaction rate is determined by slope, the result is shown in Table 4.1. As concentration of glutamine is increasing by 1.4 times, the ratio of slope between each condition is increasing around 1.4 times, which means that the reaction rate is linearly proportional to glutamine, and we can determine that the reaction order of glutamine is first order, which is consistent with the previous study[83].

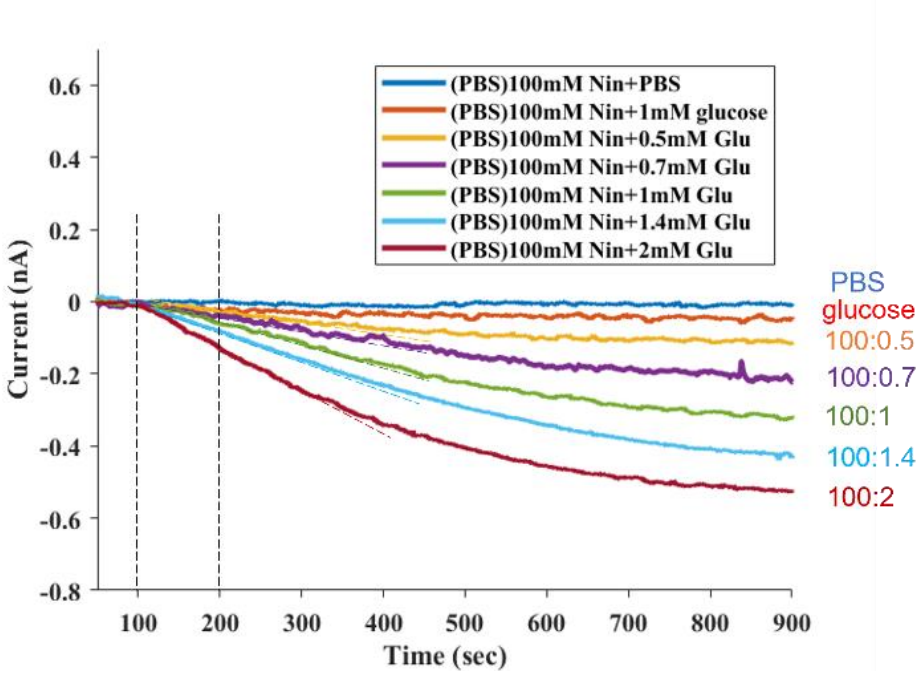

Figure 4.3. Ninhydrin reaction overall signals for experiment set 1.

Table 4.1. Initial reaction rate comparison for experiment set

Ninhydrin	Glutamine	Initial Rate (dS/dt) (slope 100-200s)	Slope ratio
100mM	0.5mM	-2.673 x10^{-4}	1.43
100mM	0.7mM	-3.832 x10^{-4}	1.58
100mM	1mM	-6.087 x10^{-4}	1.31
100mM	1.4mM	-8.015 x10^{-4}	1.52
100mM	2mM	-12.239 x10^{-4}	
	(~1.4x increasing)		**Avg: 1.46**

The second experiment was done by changing the ninhydrin concentration and keeping the same concentration of addition of glutamine. The same 1mM of glutamine is added to the base ninhydrin solution that changes from 50mM, 70mM, 100mM, 140mM, to 200mM. The overall signals are shown in Fig. 4.4. Similar observations appeared as compared to the first experiment set; the 1.4 times increase of ninhydrin gives the very close reaction rate ratio, which is 1.5 times between each slope. The overall slope ratio is shown in Table 4.2. This result is considered a pseudo-first order reaction and validates that the reaction rate is proportional to ninhydrin concentration. The first reaction order of ninhydrin and overall second order reaction can be determined, and this is still consistent with the previous study[83].

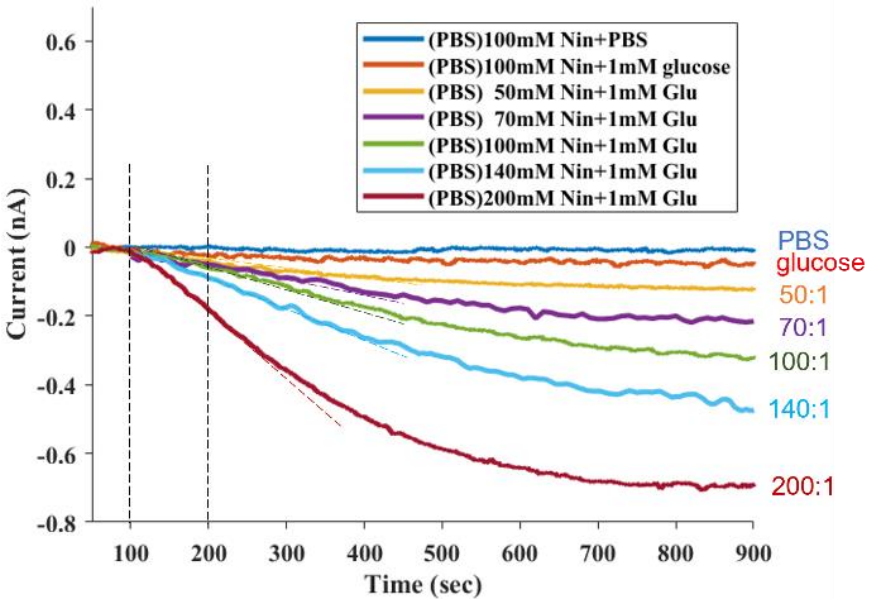

Figure 4.4. Ninhydrin reaction overall signals for experiment set 2.

Table 4.2. Initial reaction rate comparison for experiment set 2

Ninhydrin	Glutamine	Initial Rate (dS/dt) (slope 100-200s)	Slope ratio
50mM	1mM	-2.778 x10^{-4}	1.34
70mM	1mM	-3.736 x10^{-4}	1.63
100mM	1mM	-6.087 x10^{-4}	1.53
140mM	1mM	-9.312 x10^{-4}	1.77
200mM	1mM	-16.513 x10^{-4}	
(~1.4x increasing)			**Avg: 1.56**

Antibodies binding reaction (Goat IgG-Ab/Goat IgG)

To conduct the antibody affinity measurement, instead of using standard antibody-antigen binding, we chose to utilize the binding mechanism of primary and secondary antibodies, which helps to demonstrate our technique is applicable in ELISA electrical detection. The antibodies used in our measurement are polyclonal, like in most ELISA studies, polyclonal antibodies were used to increase sensitivity and amplify the signal as they allow for multiple binding sites. The primary antibody is Goat anti-Rabbit IgG which will be an immobilized antibody onto the paper, and Donkey anti-Sheep/Goat IgG is the secondary antibody that works as an analyte antibody. By utilizing the same host species of animal - goat - we were able to increase the specificity of the binding to ensure that the data was representative of the binding kinetics of the primary and secondary antibodies.

First of all, the immobilization of the primary antibody was performed by adding 2uL of 0.5mg/mL IgG on dry filter paper. The use of paper is 180um 3MM-chromatography filter paper (Whatman® cellulose chromatography paper) for this measurement because of ideal thickness so that the primary antibody is immobilized evenly in the inner portion of the paper. After the immobilization spot is dry, the paper strip is placed on the electrodes plate, in which the immobilization spot is placed on the sensing electrode, while the other side where no immobilization site is placed on the reference electrode. Then 40uL of 1X PBS was added to saturate the paper. When recording the signal, 2uL of secondary anti-IgG was added on both sides of the paper; this procedure provides the true response coming from the reaction that occurs on the sensing site. The overall workflow procedure is illustrated in Fig. 4.5. A negative control experiment is performed, in which a secondary anti-IgG was loaded on the paper where no primary IgG was immobilized on either site of the paper strip. The negative control signal is shown in blue line in Fig. 4.6, showing the signal changes little and no response or reaction occurs. While the reaction responses are also shown in Fig. 4.6. As presented, different concentrations of secondary antibodies were loaded from 0.25mg/mL to 1mg/mL and reacted with the same concentration (0.5mg/mL) of primary antibody immobilized into paper. As seen

in overall signal response, the measured current signal is coming from the binding event that occurs between those two antibodies.

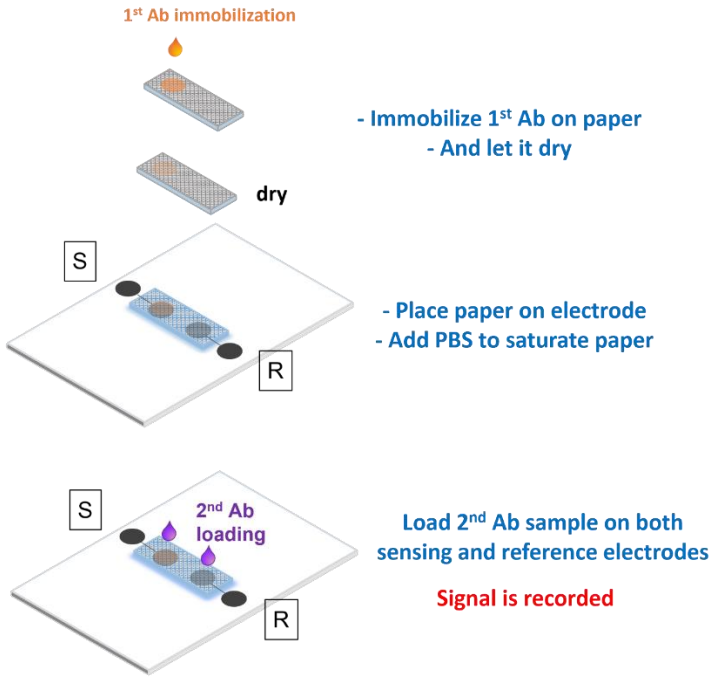

Figure 4.5. Working procedure for antibodies interaction measurement.

The initial binding rates were obtained by linear fitting the slope of the first 100-200sec, as shown in the dashed lines in Fig. 4.6, and fitting values are list in Table 4.3 for each condition. As the concentration of the 2nd antibody increases by 1.4 times, the slope ratio between each condition increases close to 1.2 times, which is close to the root-square of 1.4. The surface plasmon resonance (SPR) measurement was carried out to demonstrate the affinity kinetics of these two antibodies. The analysis of the initial binding rate can be simply measured by the tangent of slope at the first signal section where association binding occurs[85-86], as shown in Sup Fig. 4.1 to Sup Fig. 4.3. The result of SPR analysis is shown in Sup Table 4.1, displaying that the initial binding rate that occurs at the first 30-120 sec is increasing 1.4 times as the 2nd concentration increases by 2 times. The root-square rule is observed at these two antibodies binding events from our TIMES measurement and SPR analysis, showing the binding kinetics for these two antibodies can

be first order for 1st antibody, and half-order for 2nd antibody, and overall is one and a half reaction order. The assumption of half reaction order was made by multivalence of antibodies[87] due to the characteristic of polyclonal antibodies that were chosen in our measurement. Even though the complexity of binding kinetics for polyclonal antibody cannot be easily analyzed, here, we provide an estimation of binding kinetics for biomolecules affinity measurement, and this could help for determination for the occurrence of binding event between antibody-antigen, protein-ligand, or any kind of chemical reaction.

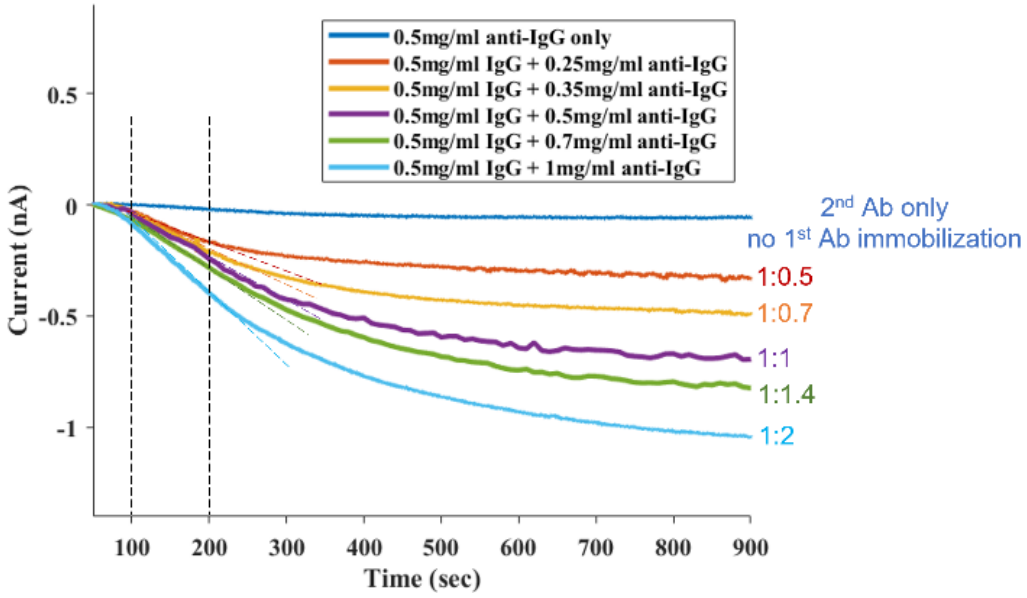

Figure 4.6. Overall signals of antibodies binding response

Table 4.3. Overall initial rate comparison for antibodies binding reaction

1st IgG Ab	2nd IgG Ab	Initial Rate (dS/dt) (slope 100-200s)	Slope ratio
0.5 mg/ml	0.25 mg/ml	-14.39 x10^{-4}	1.26
0.5 mg/ml	0.35 mg/ml	-18.13x10^{-4}	1.06
0.5 mg/ml	0.5 mg/ml	-19.13 x10^{-4}	1.14
0.5 mg/ml	0.7 mg/ml	-21.75x10^{-4}	1.43
0.5 mg/ml	1 mg/ml	-31.19 x10^{-4}	
	(~1.4x increasing)	$* \sqrt{1.4} = 1.18$	**Avg: ~1.22**

4.3 Conclusions

In this work, we demonstrate the chemical and molecular interaction on paper by measuring ninhydrin-glutamine reaction and antibodies binding interaction. The current response generated from the biological event can directly measured through our TIMES system, and the kinetics of reaction can be analyzed through initial rate calculation. But the comprehensive analysis is still under development to enhance its compatibility to more study measurement, so more insightful information we can obtain, such as reaction constant, association and dissociation constant. Especially for protein-ligand or antibody-antigen study, we are aiming to develop a methodological measurement for those binding interaction and its association and dissociation reaction. Overall, the current results with this paper-based measurement is promising, and would have potential on more applications based on this method is immobilization free on electrode surface and the paper is disposable, providing a feasible way for alternative readout of LFA research area.

4.4 Acknowledgement

Chapter 4, in part, is a reprint of the material as it to be published later: Chi-Yang Tseng, Alex Zhang, Yu-Hwa Lo. Paper-Based Transient Induced Molecular Electronic Signal (TIMES) on Reaction Kinetic Study. The dissertation author was the first author of this paper.

4.4 Supplement:

Surface Plasmon Resonance measurement:

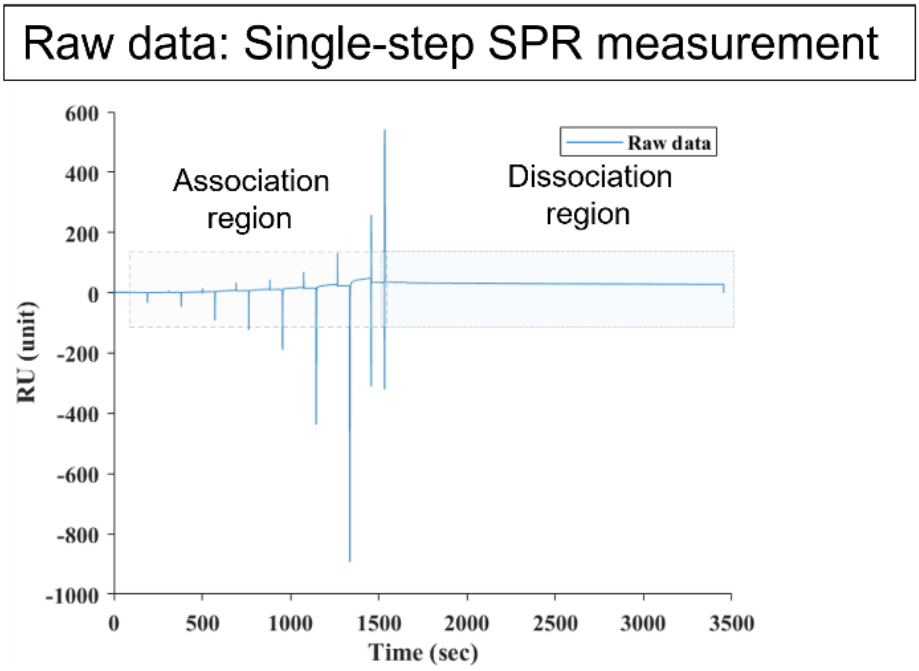

Sup Figure 4.1. Raw data of SPR measurement

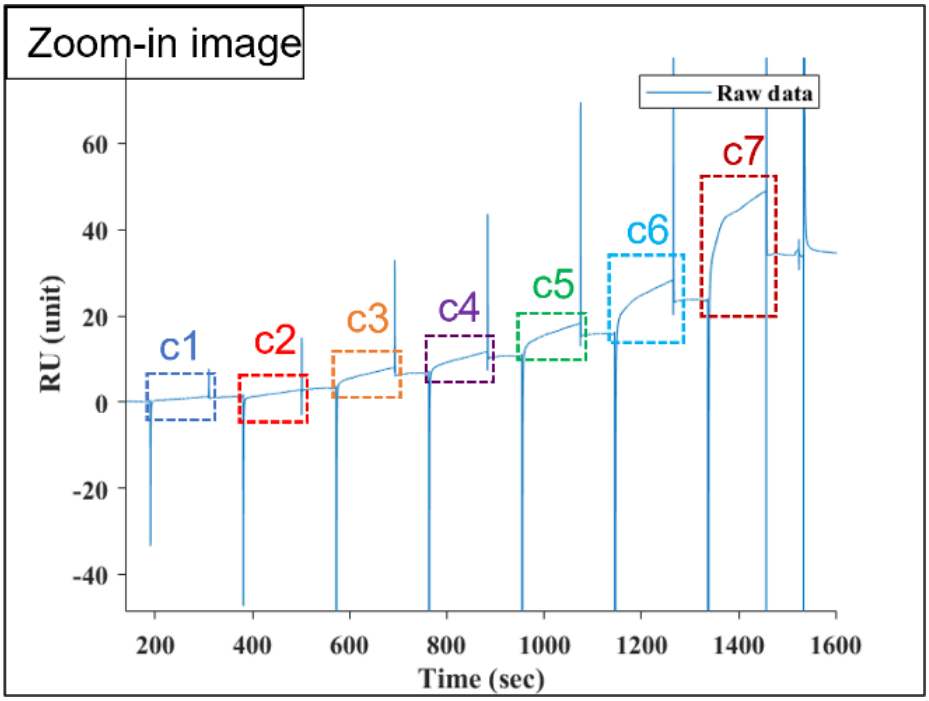

Sup Figure 4.2. Closer image of association region

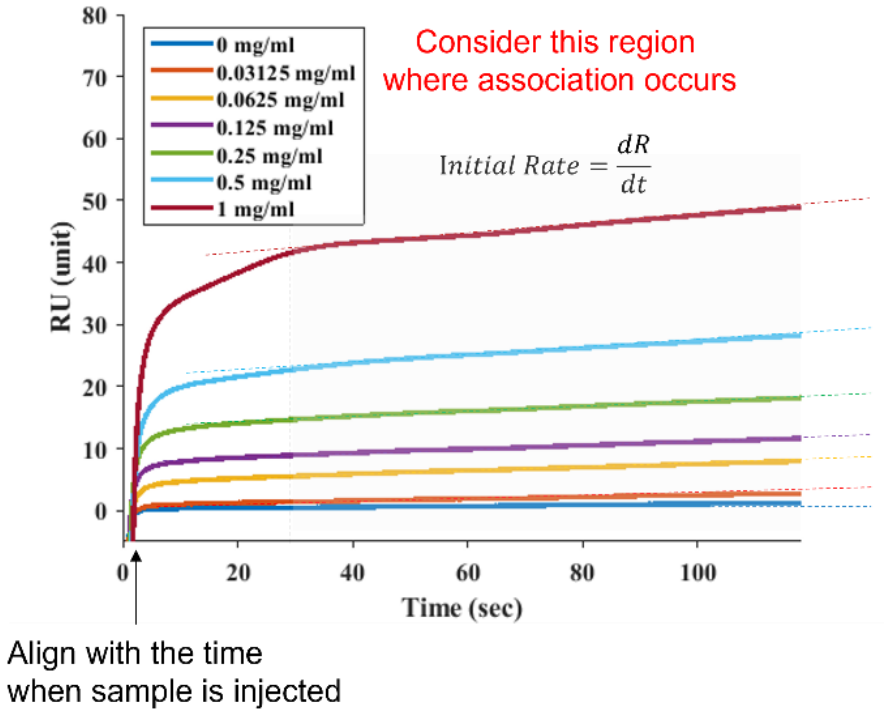

Sup Figure 4.3. Initial binding rate dR/dt analysis

Sup Table 4.1. Slope of Initial rate comparison for SPR.

1st IgG Ab	2nd IgG Ab	Initial rate (dR/dt) (slope ~80s)	Slope ratio
0.5 mg/ml	1 mg/ml	0.07654	1.35
0.5 mg/ml	0.5 mg/ml	0.0568	1.44
0.5 mg/ml	0.25 mg/ml	0.03939	1.27
0.5 mg/ml	0.125 mg/ml	0.03111	1.12
0.5 mg/ml	0.0625mg/ml	0.02776	1.79
0.5 mg/ml	0.03125 mg/ml	0.01553	1.86
0.5 mg/ml	0 mg/ml	0.008332	
	(2x increasing)	$* \sqrt{2} = 1.41$	**Avg: ~1.47**

Chapter 5

Droplet Based Neuronal Enhancer Screening

5.1 Introduction

5.1-1 Introduction - Neuronal nuclei enhancer screening

Neurons are biological cells that work like a circuit in human brain to transmit and process external information and work like a bridge to communicate each part of human body so to make different functionalities work well, such as neurons in visual system and olfactory system, they play unique roles to functionalize the body's activity. The diversity and specialized function of neurons have been intensively studied. Particularly previous studies have shown that different types of cortical neurons play distinct role in regulations of brain function.[88] The cortical neurons extract sensory information and regulate cognitive function, thus determine human's behavior output. Once those functions are disrupted by out of regulation of neurons, disorders would occur in human's behavior, such as schizophrenia and autism.[89-90]

In order to understand the role of specific neuron type, in particular, to know how different types of neurons contribute to the brain circuit, we need to identify them and manipulate their activity. Currently, the well-known techniques to identify cell types are electromyogram (EMG), in which the cells are

simulated, and the signals are recorded from the electrode[91], and by using the expressing of light-activated ion channels (opsins) in mouse cell lines to identify the cell populations[92]. But such methods are either slow and specific, or high-throughput but not specifically target highly specific cell type. Therefore, the most interested part of this study is to develop a tool with high-throughput and highly specific cell type targeting.

Enhancers are short genomic sequences on DNA to regulate transcription from nearby genes. Many studies have shown that enhances are regulating cell-type-specific gene expression by using a combination of chromatin modification and epigenetic marks mainly generated from histone modifications and DNA methylation to identify active enhancer, such methods are ATAC-seq[93], REPTILE[94], and SingleCellFusion[95]. The active enhancers are highly correlated with specific gene expression for different type of cells on both major neuron cell classes and specific subtype of those classes, so it can be high potential tool for cell type identity.

Therefore, in our project goals, we aim to:

1. Screen candidate cell type-specific enhancer in vivo.
2. Identify major cell type enhancers using transgenic mouse lines.
3. Identify more specific sub-type enhancer using fluorescent droplet RT-PCR.

To screen the candidate enhancers, we first use such methods, ATAC-seq, REPTILE, and SingleCellFusion to select the major cell type of interest. These enhancers of major classes (Pv, SSt, and Vip) are PCR amplified from mouse genomic DNA and are cloned with 11nt barcodes into an AAV plasmid to create a plasmid dictionary. Those plasmid dictionaries are then inserted with a reporter, mCherry-KASH, to produce AAv viral libraries for each interneuron class. To create a dictionary/look-up table, we added illumine adaptors to each plasmid dictionary by PCR and perform paired end sequencing to associate enhancers to barcodes. The look-up table helps to identify the enhancer to the relative barcode and evaluate the enhancer representation in each library. We perform retro-orbital injection using transgenic mouse line to identify the major cell type enhancer. We used Pv/SSt/Vip-Cre lines crossed to INTACT/Sun-1 GFP mice to express nuclear-GFP in major inhibitor neuron class. The AAv libraries we created above were

injected to the brain by retro-orbital injection in each AAv matching reporter mouse line. After 3 weeks post-injection, the brain tissue was collected, and the On-target (GFP+/mCh+) and Off-target (mCh-) nuclei can be sorted by FACS. The mRNA of those sorted nuclei were isolated, and the barcodes were PCR and sequenced. After sequencing, we can then identify the enhancers by looking up the dictionary table. The main workflow of this procedure is shown in Fig. 5.1.

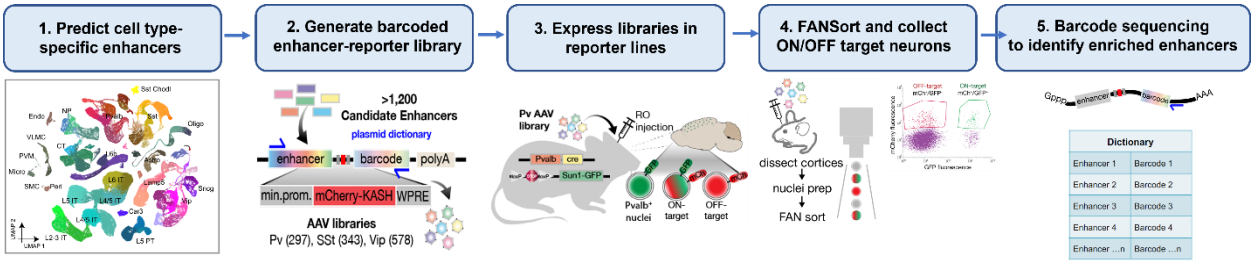

Figure 5.1. Main workflow for identifying major cell type.

There are two main workflows to perform single cell analysis:

1.) Plate-based method, such as Smart-seq2[96] and CEL-seq2[97].

2.) Droplet-based method , such as 10X Chromium Genomics and in-Drop[98].

In the first workflow, cells are sorted by FACS into individual wells of a 384-well plate that contains barcodes and lysis buffer, then the cells are lysed, RNA is captured and barcoded in the well. While in the second workflow, the cells are encapsulated with lysis buffer and barcodes into small droplet. The cells are lysed, RNA is captured and barcoded in the droplet. The droplets are then broken, RNA from all cells are pooled and converted to cDNA, then amplified to make the library. The pooling is key because the total volume of the enzyme reaction is 100-200uL and can process up to 10,000 cells in one reaction. In the plate-based method, the cDNA conversion is done in the individual wells where the minimum volume is 3-5uL, so to process the same number of cells would require about 100x more enzyme.

The previous transcriptional analysis belongs to the plate-based workflow as described in Fig. 5.1, and it works well to identify cell major types. However, when applied to millions of single cell analysis, this analysis method is extremely expensive, especially the targeted cell is in 1-2% of population. Therefore, instead of using transgenic mouse line to identify major cell type enhancer, we are going to use droplet microfluidic device to encapsulate single cell, and the specific RNA sequence in single cell can be detected through reverse transcription polymerase chain reaction (RT-PCR). The fluorescent-droplet can be sorted and used to identify more specific sub-type enhancers where no mouse line exists. The droplet-based single cell analysis has greater benefits than transcriptional analysis because it is high throughput, low cost, and low reagent consumption.

In this droplet-based method, we first retro-orbital inject each AAV library as we prepared before. After 3 weeks post injection, the cortical tissue was collected, and the nuclei were prepared for use. To perform fluorescent TaqMan RT-PCR for marker gene of subtype in droplets, we need to process two main steps. First, the lysis buffer and single cell are encapsulated in one droplet, so the RNA will be released. Second, the first droplet needs to inactivate the lysis buffer and then to be merged with second droplet that contains TaqMan RT-PCR reagent. The RNA in the merged droplet will be amplified and the interested marker gene will be fluorescent expression, and then followed by FACS to isolate the interested droplet. The main workflow for this droplet-base method is shown in Fig. 5.2 below.

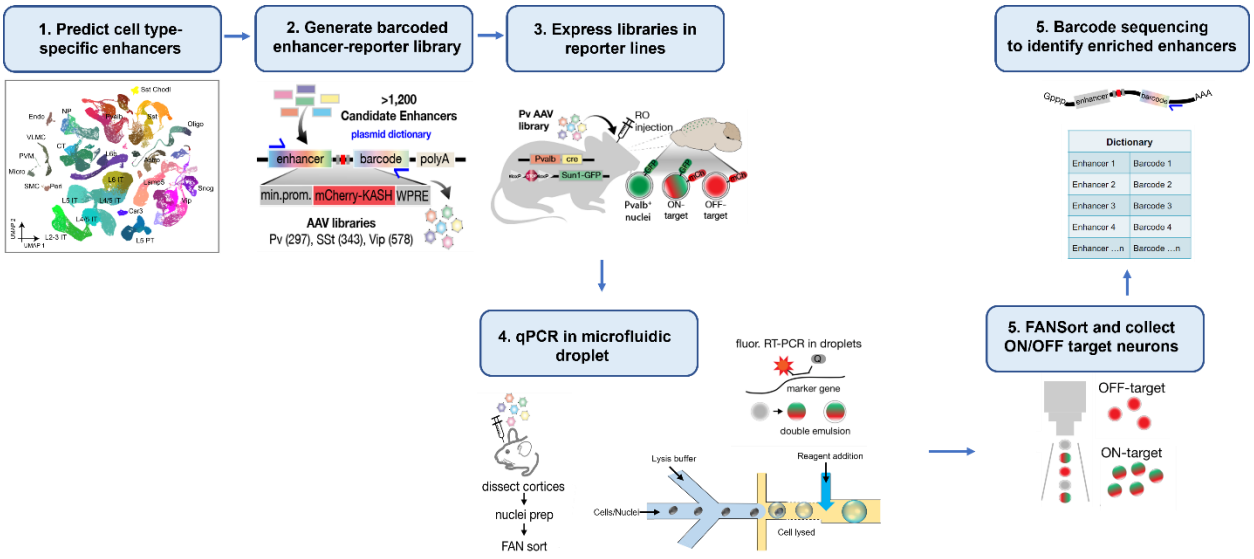

Figure 5.2. Main workflow for identifying cell subtype by using droplet-based analysis.

Beside the necessary droplet merging step, fluorescent-active sorting is also a key procedure in droplet-based single cell analysis. The conversion of droplets from oil phase to water phase so the targeted analytes are compatible to FAC sorting is essential. Because the fluorescent droplets are normally suspended in oil phase, to sort these droplets, the conversion to water phase is needed. Therefore, in the droplet-based workflow, multiple technologies and considerations are involved. In this section, I am going to present our work on droplet-based single cell analysis from the aspects of experimental development and front-end device design. To be specific, our main goal is to develop front-end techniques using microfluidic device to achieve droplet merging and double emulsion formation. The discussions will be separated into two sections, one is focusing on droplet merging and the other is on application of double emulsion.

5.1-2 Introduction - Droplet merging platform

The droplet-based single cell analysis is difficult, because merging two different droplet is not easy. Several merging methods were developed, such as manipulating microfluidic channel[99], chemically induced merging[100], and applying high electric field[101]. And one of the aims in this research is to integrate cell lyse and reagent addition steps in one device. However, there are still some limitations exist in these technologies, such as the very high voltage is needed for external voltage induced droplet merging, and the fluidic condition is not fit to all the case if we use chemical induced merging. Therefore, we present an alternative way for droplet-based single cell analysis with easier device design and better mobility of device using.

Reagent adding is a necessary step in the process of droplet-based single cell analysis. The strategies of reagent addition can be achieved by direct addition or droplet fusion. The Abate group developed a pico-injection system by using high electric field to directly inject solution into droplet[102]. The accurate injection with precisely controlled timing is needed in this method, so the operation cannot be easy, and the complicated setup is a limitation to make it widely used. The droplet fusion has wider application since the better control the volume of added solution and better device operation. Droplet fusion/coalescence mechanism can be separated into two steps, first step is droplet contact, and the second is destabilization of interface between droplets. Several studies have shown different ways to control the coalescence of droplet, and we can classify into two main mechanisms: active and passive mechanisms.

In active coalescence, droplets merging can be achieved by applying external force, such as electro-coalescence[101], laser-induced coalescence[103], and acoustic wave induced coalescence[104]. The advantage of this method is using the external force to make the interface of droplet unstable and merge quickly. The most common used technique is electro-coalescence, in which the droplet merging achieved by using high electric field to induce opposite electrical charge on droplet surface to destabilize the interface of droplet and make them merge. A better coalescence control in the applied voltage range is from 1V to several kV, and frequency is from DC to several kHz[105]. Even the active coalescence method has better control on droplet fusion, the requirement of external electrode and instrument make this method more complicated.

Different from active coalescence, passive coalescence does not require external forces. Variety of passive merging mechanisms have been developed, such as designing different geometry of microfluidic channel[99, 106-107], using chemical inducer[100], or by changing surfactant concentration[108]. Changing microfluidic channel design is the earliest finding to make droplet merged, for example, the expanding channel can enhance the collision of two droplets and further make them merge[106], the micro columns in channel can trap the droplets then the droplets are merged[107], and the zigzag channel design can enhance the adjacent two droplets to merge[99]. Chemical induced droplet merging is one of the merging methods, the Weitz group used perfluorobutanol (PFB) as a destabilizer to reduce the tension in interface between droplets so the droplet can merge[100]. In addition, droplet merging can also be done by adding lower concentration of surfactant oil phase, this is the same concept by reducing the tension of droplets interface[108]. From above studies, we can find that, the key parameter for passive merging is to reduce the stability of the interface between droplets. But this is a trade-off, since we need the droplet become robust to environment for bio-application, but at the same time, we need to lower down the stability to make droplet merged. Even external forces are not required for those passive coalescence and make them easier to operate, how to control the concentration of surfactant in merging mechanism is the main consideration. Therefore, in our study, we are going to develop a new method to avoid complicated setup use, and the working condition can fit to all of the application case.

5.2 Experiment results and discussions

Merging device design

In our device design, we are using pillar structure that located in the microfluidic channel to make the droplet merge. We fabricate the pillar structure on the glass slide and will bind with PDMS microfluidic channel. The pillar is aligned well on the middle of the channel right behind the junction where two droplets meet. Once the droplets attach each other at the Y-junction, they will flow together and pass through this pillar. The pillar is 1/3 of channel height and is high enough to contact the droplets. So once the droplets are passing through the pillar, and pillar contact the interface of droplets, the interface will become unstable, and two droplets then be merged. The main concept is the same, to make droplet merge by using destabilization of interface of droplets. The image of pillar structure located at microfluidic channel is shown in below Fig. 5.3.

This pillar-induced merging method can belong to passive merging mechanism. Even we know in passive merging mechanism, the lower concentration of surfactant in oil phase give us better merging efficiency, this is not good for bio-application, especially in qPCR procedure. Because lower surfactant is not stable under higher temperature and would cause more droplet coalescence during the thermal cycle step. So in droplet-based single cell analysis, we need to maintain the droplet stability with high enough surfactant concentration. Therefore, in our device operation, we use the oil phase that directly purchase from Bio-Rad, and this is the oil that fit to PCR thermal cycle experiment. We adjust the oil phase concentration (fluorinated oil based) from 20X diluted to original 1X by using HFE-7500 oil, we found that, the merging efficiency do not affect by concentration changing. This shows that our pillar-induced merging method does not have limitations on concentration of surfactant controlling and has wider range of application.

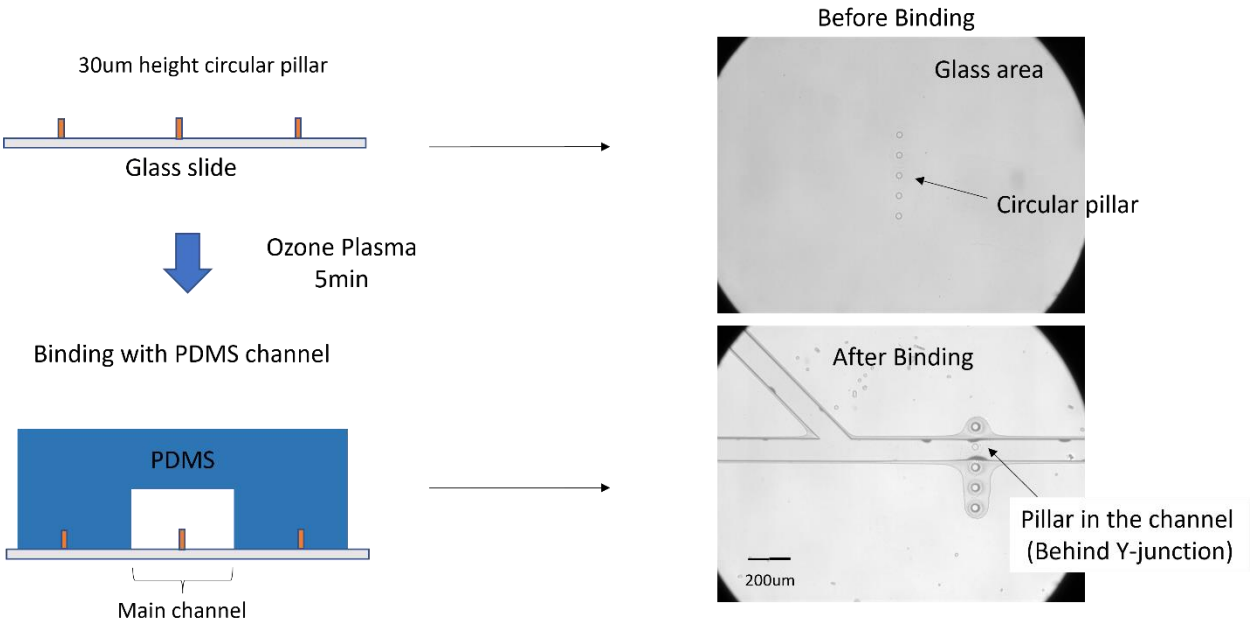

Figure 5.3. Merging device with pillar structure. Pillar is located at Y-junction where droplets meet.

Droplet merging using color dye as example

To demonstrate the capability of pillar induced merging platform, we first use the merging device and single droplets that are generated from the same device and contain color dye or water.

As shown in Fig. 5.4, the blue color dye and Bio-Rad oil were introduced in 1st single droplet Generation channel to create the 1st single droplets. At the same time, the DI water was introduced from the upper inlet, where Buffer/Reagent injection channel. The 1st single droplet (dark blue) can meet the second droplet (white) in the Y-junction and merge after passing through the pillar structure. The Zigzag channel is for enhancing the solution mixing inside the merged droplets. The Other channels, stabilization oil channel and double emulsion channels were not using at this time.

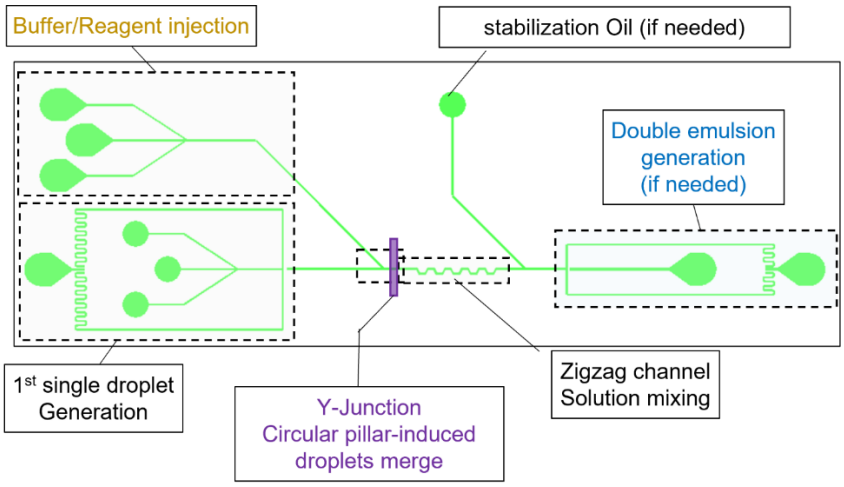

Figure 5.4. Channel design and operation of merging.

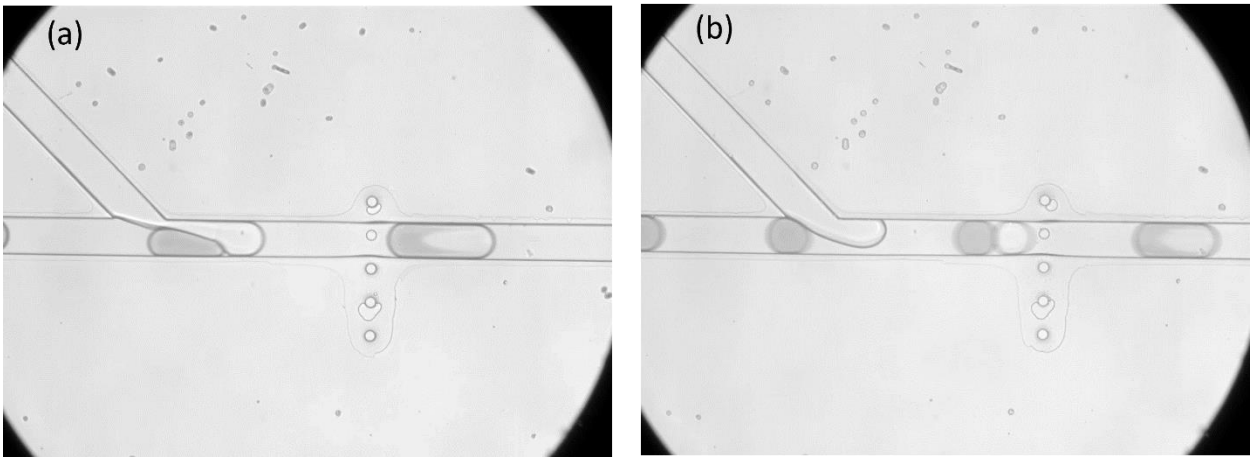

Figure 5.5. (a) larger size droplet merging with lower frequency. (b) smaller size of droplet with higher frequency.

We are trying to create a working condition range of this technique. We adjusted the flow rates for each fluid (blue dye solution, oil, and DI water) to control the size and droplet generation frequency. By doing this adjustment, we can compare the size ratio of droplets before and after merged under different frequency, and also find out the merging efficiency for each working condition. As shown in Fig. 5.5(a) and 5(b), different size and generation speed of droplet can be controlled, and the merging is working in certain operation range. We list the overall result in Table 5.1. And we can find out the working rage is wide, that fit to larger to smaller size of droplets.

Table 5.1. Conditions for droplet merging

Blue@H2O (uL/min)	Diluted 20X-oil (uL/min)	H2O (uL/min)	Frequency (# droplet/sec)	Single droplet Volume (nL)	Merged droplet Volume (nL)	Yield
5	10	5	~32	2.3	4.38 ±0.25	99%
5	15	5	~92	0.91	1.69±0.24	82%
5	20	5	~122	0.48	1.32±0.00	100%
5	25	5	~133	0.32	1.07±0.00	100%
5	30	5	~141	0.27	0.90 ±0.00	77%
3	10	5	~54	0.91	2.56 ±0.48	86%
3	15	5	~70	0.66	1.88 ±0.21	68%
3	20	5	~78	0.57	1.82 ± 0.00	83%
3	25	5	~85	0.32	1.66±0.00	96%
3	30	5	~100	0.23	1.41 ±0.00	96%
Blue@H2O (uL/min)	Diluted 20X-oil (uL/min)	H2O (uL/min)	Frequency (# droplet/sec)	Single droplet Volume (nL)	Merged droplet Volume (nL)	Yield
3	10	1	~49	1.72	2.63±0.40	36%
3	15	1	~75	0.82	2.11±0.18	26%
3	20	1	~100	0.38	1.47±0.16	25%
3	25	1	~145	0.36	1.53±0.19	28%
3	30	1	~75	0.27	1.52±0.21	27%
1	10	1	~30	0.59	1.84±0.12	90%
1	15	1	~32	0.49	1.91±0.24	52%
1	20	1	~37	0.43	1.76±0.08	50%
1	25	1	~44	0.38	1.65±0.16	50%
1	30	1	~47	0.27	--	<10%
Blue@H2O (uL/min)	Diluted 20X-oil (uL/min)	H2O (uL/min)	Frequency (# droplet/sec)	Single droplet Volume (nL)	Merged droplet Volume (nL)	Yield
3	10	1	~49	1.72	2.63±0.40	36%
3	15	1	~75	0.82	2.11±0.18	26%
3	20	1	~100	0.38	1.47±0.16	25%
3	25	1	~145	0.36	1.53±0.19	28%
3	30	1	~75	0.27	1.52±0.21	27%
1	10	1	~30	0.59	1.84±0.12	90%
1	15	1	~32	0.49	1.91±0.24	52%
1	20	1	~37	0.43	1.76±0.08	50%
1	25	1	~44	0.38	1.65±0.16	50%
1	30	1	~47	0.27	--	<10%

$$Yield = \left({}^{\#\ Merged\ droplet}/_{\#\ total\ single\ droplet\ produced}\right) \times 100\%$$

Re-injection merging using color dye as example

After using color dye droplet to demonstrate the capability of droplet merging, we need to do another demonstration to simulate the condition when we do the real experiment with cells and nuclei sample. Because the overall workflow for cells/nuclei experiment, we have three main separate steps: 1. Cell encasulated in singel droplet with lysis buffer, then cell lysed and RNA released. 2. Inactivate lysis buffer under higher temperature, then introduce 1st single droplet to merging device to merge the droplets that contain RT-PCR reagent. The RT-PCR cycles are done after droplets merged. 3. The fluoresent droplet can be produced during RT-PCR step. Then we create double emulsion formation for the droplets, and those fluoresent droplet can be sorted via FACS.

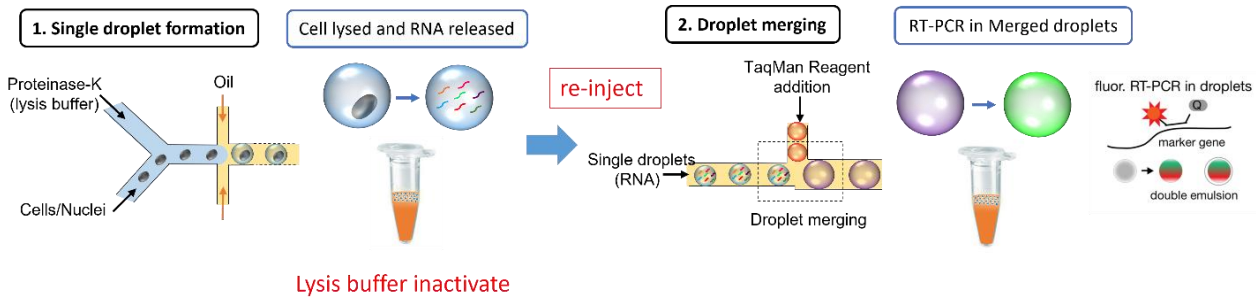

Figure 5.6. Separate operation between each steps, and re-injection of droplets is needed.

The previous three main steps are separate, that means, we need to collect the droplets in the tube and let it react in the tube. Taking for example, from the first step, after droplte capture cell and lysis buffer inside, the droplets are collected in the tube, and need operate separatly. After lysis buffer is inactivated in the tube, we need a re-inject those drplets to the device again, like shown in Fig. 5.6. Therefore, we need to demonstartion the re-injection step to see if it is still working for droplet merging. To demonstrate the capability of re-injection, we use 1st device as shown in Fig. 5.4, to create single droplet that contain blue dye, the droplet size is around 90um in diameter, which we found is ideal size that fit to our expection on

creating 1:10 merging size ratio. Because we need to create 10X volume after merging to dilute the lysis buffer (proteinase-K) to make it totally inactivated so the enzymatic reaction for RT-PCR reagent (TaqMan probe) would work properly. The collected single droplets were collect in 1.5mL eppendorf tube, and will be re-injected through the air-driven adopter to the merging device. The overall experiment setup is shown below in Fig. 5.7.

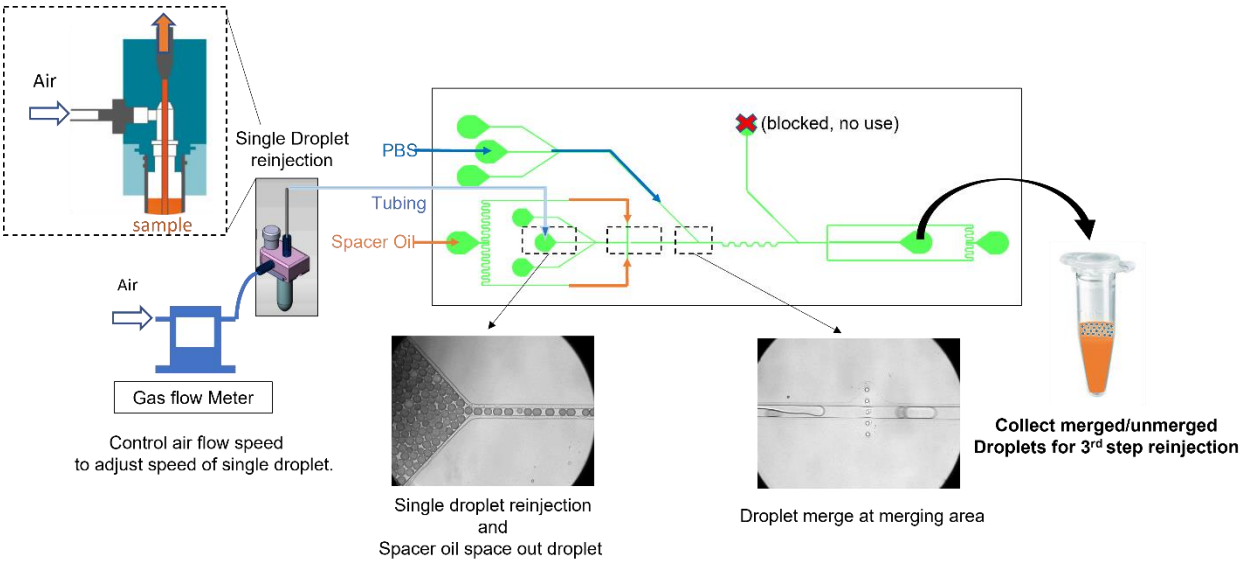

Figure 5.7. Overall setup for re-injection droplet merging.

We adjust each parameters to optimize the working condition, such as adjusting the flow speed of air controller to control the re-injection rate of 1st single droplet (blue), and oil flow rate to control the generation frequencey of 2nd droplet (white). The oil phase also used for spacing out the 1st single droplet, so by adjusting the oil phase speed, we can have a better synchronization of two droplets meet. The overall table show the testing conditions, and to achieve 1:10 ratio, we can see a ideal operation condition, the results are listed in Table 5.2.

In this Table 5.2, we can found some conditions are good to achieve above 1:10 size ratio with high merging efficiency, but we did not consider those conditions are good operation parameters because those

conditions would produce more 2nd droplets (white), and this is not good for cell/nuclei experiments. We want to save more reagent using. Besides, we want to noted that the calculation of yeild in the table does not include the amount of 2nd droplet, only the 1st droplet is considered.

Table 5.2. Re-injection working condition to achive 1:10 merging ratio.

Air flow (slpm)	Reinject Frequency (# droplet/sec)	Diluted 20X-oil (uL/min)	H2O (uL/min)	Single droplet Volume (nL)	Merged droplet Volume (nL)	Yield	Merging ratio
0.005	~8	10	2	0.22	2.27±0.54	85%	1 : 10.3
0.008	~6	10	3	0.22	2.61±0.70	87%	1 : 11.7
0.010	~2	10	4	0.22	2.91± 1.04	80%	1 : 13.2
0.012	~24	10	5	0.23	1.89±0.82	78%	1 : 8.2
0.015	~12	10	6	0.22	3.23±1.22	98%	1 : 14.7
0.007	~9	15	2	0.22	1.71±0.48	66%	1 : 7.8
0.011	~5	15	3	0.23	2.14±0.49	73%	1 : 9.3
0.010	~8	15	4	0.22	2.31± 0.60	87%	1 : 10.5
0.014	~11	15	5	0.23	2.40±0.65	84%	1 : 10.4
0.025	~12	15	6	0.22	2.73±1.01	88%	1 : 12.4

Good condition

Double emulsion formation

In 3rd step of overall workflow, the double emulsion formation is needed. Here, we follow the same strategy, using merged droplet (containing blue color dye) to demonstrate the double emulsion operation. To create double emulsion, the re-injection of merged droplets is needed, and spacer oil will also introduce to space out the re-injected droplets. The working setup for double emulsion is shown as Fig. 5.8. We also conduct multiple working conditions by adjusting the flow rate and air pressure to summarize the operation range. The Table 5.3 shown below lists the testing conditions we consider, and the optimal condition is marked.

Table 5.3. Double emulsion formation testing conditions.

Condition	Droplet reinjection (#/sec)	Spacer oil (uL/min)	Continuous phase (uL/min)	Double emulsion diameter (um)	Single droplet @double emulsion	Multiple droplets @double emulsion	Total droplets counted
1	~15	5	15	~180	2.5%	1%	453
2	~30	10	30	~170	16.5%	0.2%	496
3	~20	15	40	~180	4.9%	0%	612

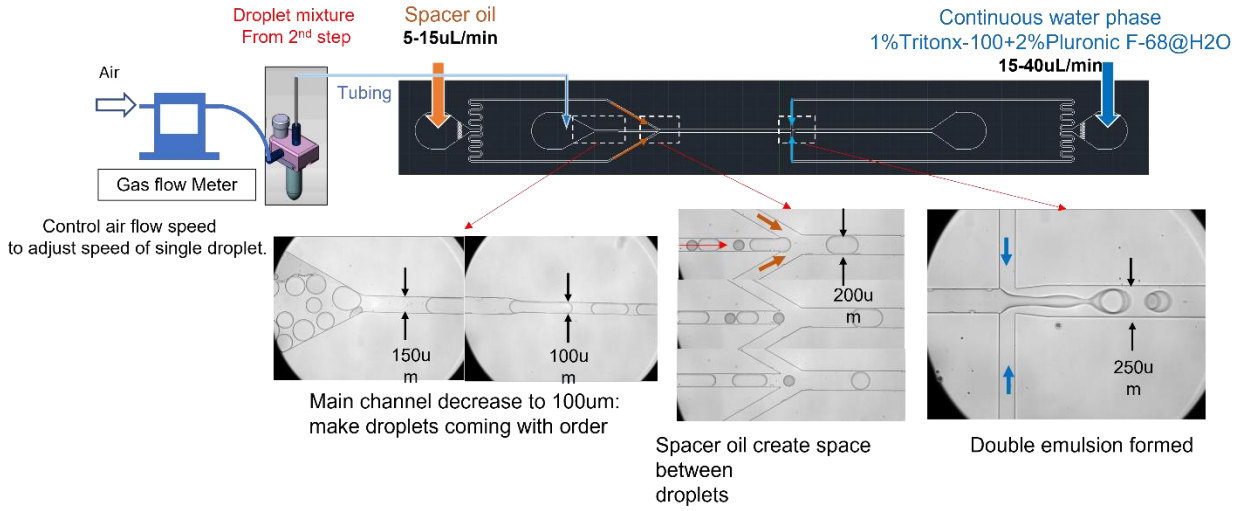

Figure 5.8. Setup for re-injection of merged droplets for double emulsion formation.

Nuclei and cells experiment

To conduct the experiments with biological samples and prove the capability of our technique, three samples were used:

1. DI water as negative control sample.

2. Whole HEK cell sample as positive control sample.

3. HEK cell nuclei as targeted sample experiment.

Those three samples were introduced separately with Proteinase-K lysis buffer and were encapsulated into single droplet. The cell or nuclei will be lysed, and RNA were released inner the droplet. After 20min lysis at 37ºC, the temperature was increased to 55ºC to inactivate the Prot-K buffer. Because we used the thermolabile lysis buffer, the operation of temperature is relatively low. After that, the droplets were re-injected to merging device, and flow TaqMan reagent altogether to make the droplet merge. Those merged droplet were collected and followed by RT-PCR thermal cycles. The detailed description of experiment procedure is in experimental method section. During the RT-PCR cycles, we can observe if the fluorescent signal occurs. Typically, after 45X cycles we can see fluorescent response. To make sure the RNA is amplified large enough, we did 60X cycles in this step. The overall experiment procedure is illustrated in Fig. 5.9.

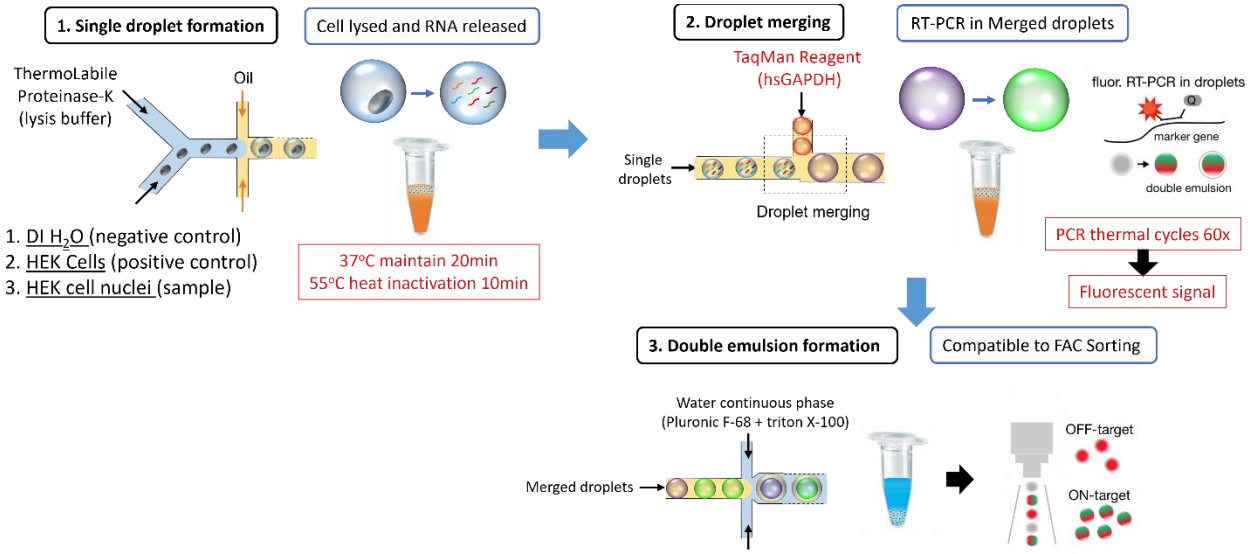

Figure 5.9. Experiment procedure with HEK cells and nuclei samples.

As shown in Fig. 5.10, after 60X cycles, the fluorescent signal response in whole cell samples and nuclei samples are clearly seen after 45Xcycles. Compared to cells and nuclei samples, we can see the signal of cells is stronger than nuclei, this is because whole cells contain more RNA, so the intensity is stronger. The result showing both signals are large enough meaning the amplification is working properly. On the other hand, the DI water sample shows no fluorescent signal, that is valid to our estimation, meaning no reaction occurs during RT-PCR step and no other contaminations exist during the experiment process.

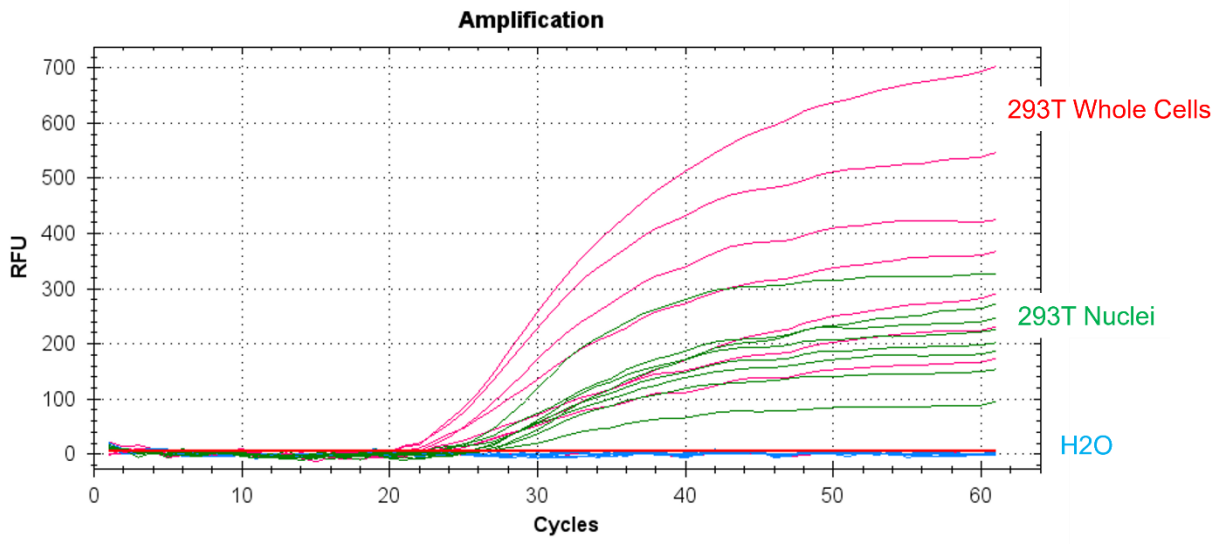

Figure 5.10. RT-PCR results with three samples: 1.DI water, 2. HEK whole cell, and 3. HEK cell nuclei.

The microscopic images are showing in Fig. 5.11, showing the fluorescent signal is strong for whole cell and nuclei droplets, but no fluorescent droplet observe for DI water droplets. Those results prove that our merging design is working and ready for further experiment.

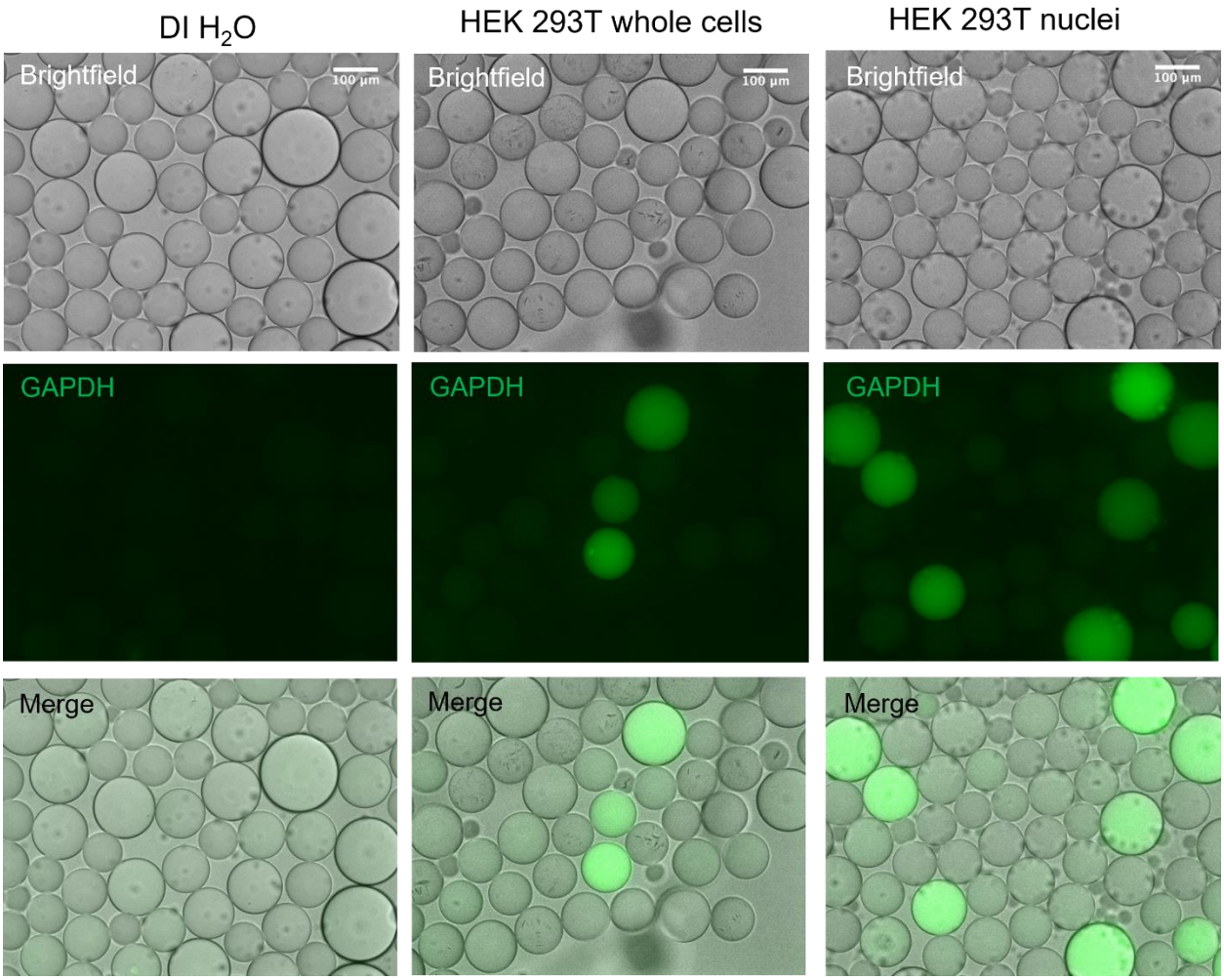

Figure 5.11. Microscopic images for three sample droplets after RT-PCR cycles.

5.3 Fabrication of device and experimental methods

Silicon wafer mold for PDMS microfluidic channel.

1. Silicon wafer is cleaned with acetone, methanol, IPA, and DI water.

2. NR9-3000PY photoresist was spung coating on silicon wafer with 500rpm 10sec, 800rpm 40sec.

3. 150^{o}C soft bake for 1min.

4. Expose with patterned mask (MA6) or using mask-less laser writing machine (MLA150).

5. 100^{o}C post bake for 1min.

6. RD6 developer is used for developing pattern with 1min.

7. Descum the surface with PE100, 200W 1min.

8. Silicon etching with Oxford P100 to etch the silicon to certain height.

9. Using acetone to liftoff the photoresist.

10. Using silane to coat silicon wafer to make surface hydrophobic.

11. Pour PDMS to silicon mold and incubate under 65^{o}C overnight to make it fully cured.

Single droplet generation device

The first device is to create the water-in-oil single droplet that encapsulate DI water, single HEK whole cell or HEK cell nuclei with thermolabile Proteinase-K lysis buffer inside. The single nuclei/cell is operated under density of 200-500/uL to avoid multiple cells in one droplet, and the 1X PBS buffer was used for dilution. The inlet of device for nuclei/cell channel was treated with 1% BSA solution to make it hydrophilic before use, so that the nuclei/cell will not easily precipitate on channel walls. The Bio-Rad or 10X fluorinated oil was used as oil phase. When operating the droplet creation, the flow of nuclei/cell is 0.5uL/min, the thermolabile Proteinase-K lysis buffer was flow with 0.5uL/min, and oil phase flow is 15uL/min. The size of droplet is 90um in average. The channel image is shown in Fig. 5.12.

The droplets are collected in Eppendorf tube, and the nuclei/cell will be lysed and RNA release inside the droplet. The droplets maintain at 37°C in 20min and then heat up at 55 °C in 10min for Proteinase-K inactivation. This process is be done Bio-Rad C1000 Touch thermal cycler with CFX96 Real-Time System.

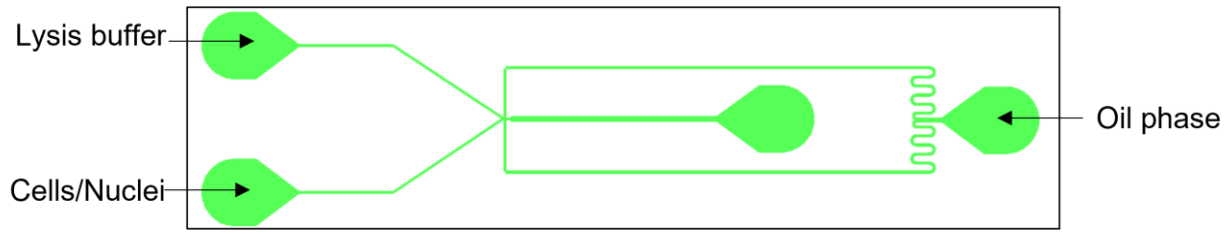

Figure 5.12. Single droplet formation device

Droplet merging device

To fabricate the pillar-driven merging device, two-step process is needed.

First of all, the pillar structure is developed by SU-8 2025 photoresist by photolithography process. Generally, SU-8 2025 was spun coating on glass slide with 3000rpm, followed by 65 °C to 95 °C to 65 °C soft bake process. The Heidelberg 150 (MLA 150) was used to mask-less pattering on glass slide and followed by 65 °C to 95 °C to 65 °C post bake process. Then the glass slide was developed by SU-8 developer to remove the un-patterned region. The slide was heated up with 150°C back heat process to fully develop the pillar structure (30um in diameter and 30um height). After the slide is finished, the microfluidic channel patterned PDMS was bound to the pillar-structure glass slide by using ozone-UV treatment and 100 °C heat enhancement. The Design is as same as Fig. 5.4.

To operate the droplet merging with re-injection procedure. The collected single droplets are stored in Eppendorf tube, and installed in re-injector adopter, as shown in Fig. 5.7. The re-injected droplets were

driven by air pressure, the air flow is controlled by SmartTrak50 (Sierra, C50L-AL) under 0-0.2 standard litter per min (splm) range. The droplets were re-injected into device for merging, and spacer oil is also introduced for spacing out the re-injected droplet. The spacer oil is adjusted from 20-fold diluted to original oil by using HFE-7500 oil. The TaqMan reagent (IDT, PrimeTime® Mini qPCR Assay, Assay ID: Hs. PT. 58. 40035104, Gene Name: GAPDH, Probe: 5'-/56- FAM/CCGTTGACT/ZEN/CCGACCTTCACCTT/3I ABkFQ/-3', Primer 1: 5'-CTCTCTGCTCCTCCTGTTC-3', Primer 2: 5'-GCGCCCAATACGACCAA-3') was injected from the Buffer/Reagent injection channel and will meet the 1st droplet at Y junction, and merged after passing through the pillar, as shown in Fig. 5.7.

The merged droplets were also collected in Eppendorf tube. The PCR cycles was performed under below procedures: reverse transcription (RT) at 48 ºC in 45min, poly chain reaction (PCR) denature step at 94 ºC 1min, followed by 60cyles of 94 ºC to 55 ºC to 68 ºC, then keep 68 ºC for 5min.

Double emulsion device

To compatible to FACS, droplets are needed to be encapsulated into water-in-oil-in-water double emulsions. The double emulsion formation device is used for this procedure. The 2nd junction channel where double emulsion will be formed was treated with 1% PVA (polyvinyl alcohol) to make the channel wall hydrophilic. The re-injected droplets were processed like the step describe in previous re-injection method. The spacer oil is also needed to space out the droplets. The water continuous phase was prepared by 1% Triton-X 100 +2% Pluronic F-68 and was injected with 50 uL/min to encapsulate the single droplet to become double emulsion. The setup for this process is shown in Fig. 5.13.

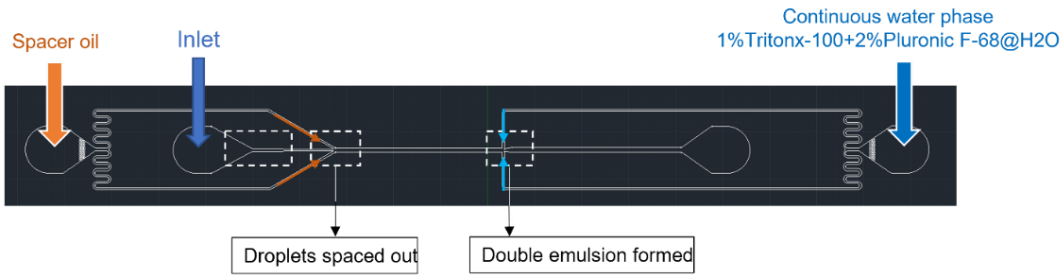

Figure 5.13. Setup for re-injection with double emulsion formation.

5.4 Conclusions

In this project goal, we are trying to study neuron subtype by using droplet-based enhancer screening. The main core of this work is to develop a microfluidic technique to achieve droplet merging so we can operate the biological reaction in those tiny droplets.

In device development, we successfully fabricated merging device to achieve droplet merging by using pillar-induced mechanism. The two different droplets can be created or introduced to the microfluidic device and merged after passing through the pillar structure located at the channel. This feasible merging provides many advantages, the easy fabrication, no complicated setup needed, and fit to all working condition. The droplet merging is demonstrated by using droplet creation in microfluidic device or droplet re-injected by air-driven adaptor. Both working conditions are showing good merging efficiency and showing its capability on droplet-based single-cell study. Even though this is a long-term project on enhancer screening experiment, this technique is ready to apply for experiment workflow.

5.5 Acknowledgement

Chapter 5, in part, is a reprint of the material as it is to be published later as, Chi-Yang Tseng, Zhilin Guo, Celine Vuong, Edward Callaway, Yu-Hwa Lo. Enhancer Screening Using Single-Nuclei Droplet RT-PCR. The dissertation author contributed to the fabrication of device.

Chapter 6

Double Emulsion with 2D Image-Guided Sorting System

6.1 Introduction

In droplet-based single cell analysis, the fluorescent activated cell sorting (FACS) is the essential step. Unlike cell sorting, fluorescent droplet sorting is not simply sorted with common FACS instrument since the incompatibility aqueous phase. The common flow cytometer sorters operate the sample particles suspended in aqueous phase. The water-in-oil fluorescent droplet, however, is oil-phase and immiscible to aqueous sheath fluids in flow cytometer. Even though some works enable single-droplet sorting operating under oil-phase by using embedded electrode[109-110] or optical assembly[111], these works are not commonly used due to complicated equipment setup and lack of sorting functions for different fluorescence wavelength readout channels. Compared to common FACS instrument, those technics remain low throughput and low accuracy. The commercial FACS instrument is still considered as main tool for sorting because of the high sorting efficiency >70% and multiple fluorescence readout channels[112-114]. Sorting

fluorescent droplet via FACS would be the most feasible way for further downstream qPCR or sequencing analysis. However, sorting single droplets via FACS is difficult due to the incompatible phases. To address this challenge, the formation of water-in-oil-in-water double emulsion is needed in the workflow. The formation of double emulsion allows the fluorescent single droplet encapsulated into droplet in oil-in-water phase, which is able to suspend in aqueous and compatible to FACS instrument.

Sorting double emulsion has been demonstrated in many works[115-118]. However, many of them show poor post sorting result and efficiency, which might be due to unstable double emulsion and breakage occurs during sorting with high sheath flow. In our work, the double emulsion formation is achieved, and the stability was tested, showing good uniformity and maintain good shape after a few days storage. For the application of double emulsion, we are trying to combine this technique with the 2D-image guided sorting flow cytometry system that developed in our research group to cell phenotype and genotype study.

As the advance of droplet-based single cell analysis, high-throughput single cell RNA sequencing (scRNA-seq) have been achieved to identify cellular heterogeneity[119-121]. The popular droplet-based technologies include 10X Chromium Genomics, Drop-seq, and in Drop[98]. These platforms create water-oil droplets that contain cell and barcoded gel beads, resulting in highly efficient interrogation of thousands of cells. The gel barcoded beads are designed with rarely identical barcodes, and are able to study gene expression and protein markers simultaneously with the capture sequences which share same barcode as the poly(dT) probe on beads[122-125].

A highly potential application of droplet-based technique is to relate cell phenotype to cell genotype through variety of measurements from the same cell. Capturing cell image provides insightful information of cell, such as cell's transition sate, cell-cell interaction, and rare cell subtype. If those transcriptomic, genomic, epigenetic, lineage states and microscopic image of a single cell can be obtained in a time, we are able to identify the cell type that we did not discover before[126-128]. A numbers of multiplexed barcoding technologies have been proposed to correlate cell image and cell genome information[129-130]. Generally, the cell microscopic images taken from these technologies are created when the cells were placed on the well

plate or substrate before cell suspension and droplet formation, and the position of cell was located by using secondary barcode. The limitation existed in these technics is that the nonadherent cell type is not suitable for these applications, such as blood and immune cells, which have important implications in immunology, oncology, organ transplant, autoimmunity, and infectious disease[131-140]. However, some works show that the flow cytometry can be applied to study multiple biomarkers simultaneously[141-152].

In our work, we propose a technique based on flow cytometry to link cell phenotype to cell genotype by capturing 2D/3D image of non-adherent cells and their mRNA profile. The "2D/3D image guided flow cytometry" systems were emerged in 2018 from collaboration between Lo Research Lab and NanoCellect[153]. Those systems can generate 2D/3D image of each cell and sort that to be sequenced. Our technology is also available to be coupled with droplet-based single analysis by utilizing the formation of double emulsion that encapsulate single cell and barcoded beads inside. The double emulsion is compatible to flow cytometry guided fluid and contains the 1). a cell to be sequenced, 2). 10X Genomics gel beads, 3). a plurality of InSight beads from NanoCellect Biomedical, Inc., which express fluorescence detectable by the imaging flow cytometry, as well as a unique molecular barcode which can be linked to the fluorescent barcode post-scRNA-seq. The proposed idea and workflow are shown in Fig. 6.1.

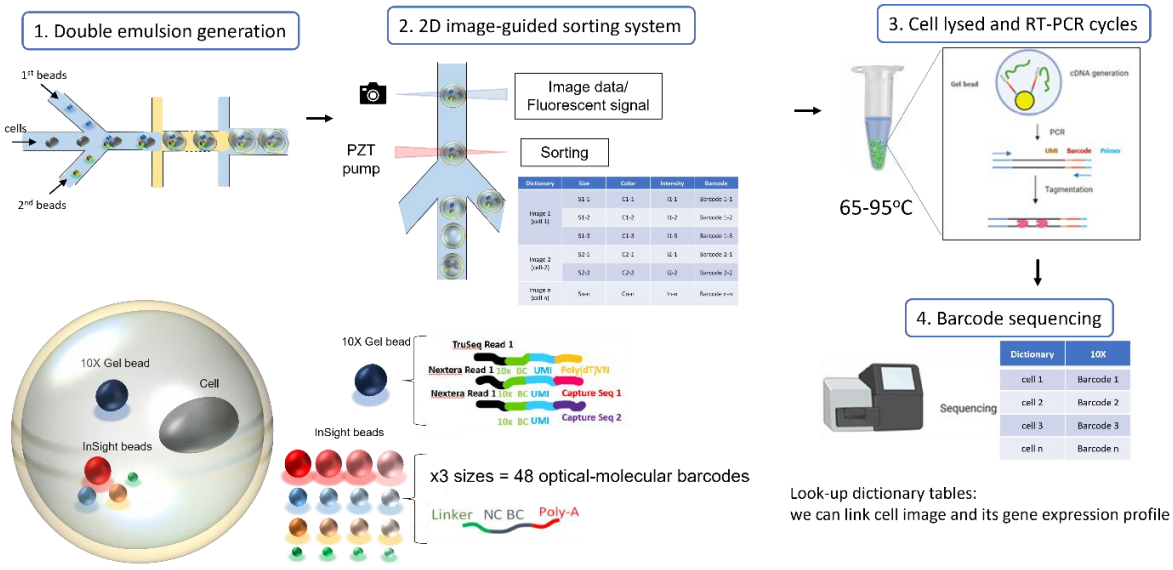

Figure 6.1. Workflow of double emulsion application on cell phenotype-genotype study with TIGS system

A brief introduction on workflow showing in Fig.6.1: the cell and barcoded beads are first encapsulated into double emulsion. In double emulsion, we can have different combination of beads with cell by using different fluorescent colors and size. When introduced to 2D-image flow cytometry system, the image of double emulsion that contains cell and different size or color of beads as recorded. After sorting, the cells are lysed followed by qPCR procedure to amplify the RNA. Finally, the barcode sequence is performed, and a look-up table is generated. We can use the table as index to link the previous image table, and to relate the cell genotype to its phenotype.

6.2 Fabrication of microfluidic device

Double emulsion device

To create double emulsion, the 1% PVA is first prepare in distilled water, which is used for hydrophilic treatment to PDMS channel wall. To dissolve PVA in DI water, PVA was stirred in water in room temperature for 40mins, and gradually increase the temperature to 100 ^{o}C then keep for another 40min. Then decrease the temperature to 65 ^{o}C and left the solution overnight. Now the PVA is totally dissolved in water and ready to use.

The 1% PVA solution is injected into the channel region where double emulsion will be generated. Let the channel filled with 1%PVA and stay 20min. Then using syringe to blow air pressure into the channel to remove the PVA solution in channel. To totally remove the PVA liquid solution, place device on hot plate and heat up at 80 ^{o}C for 15min. Repeat above processes three times then the coating of PVA on PDMS channel wall is finished.

The device design is shown in below as Fig. 6.2. The inlets are used for introducing cells solution or beads solution, typically the operation flow rate is around 1-10uL/min. The oil phase is flowing Bio-Rad-oil or 10X Genomics oil, which are fluorinated oil, and are operated in 10-20uL/min. The above rate range can generate ~30-50um wide single droplet at the first T-junction. This region for first single droplet

formation is under hydrophobic environment, in which PDMS channel wall is not treated with PVA. On the other side, the single droplets flow to second T-junction, where the channel is treated with 1% PVA and droplets can be formed into double emulsion by using ~40-60uL/min sheath flow of water detergent solution, which contains 1% Triton-X 100+2%% Pluronic F-68 in DI water. The size of double emulsion is around 50-70um in diameter.

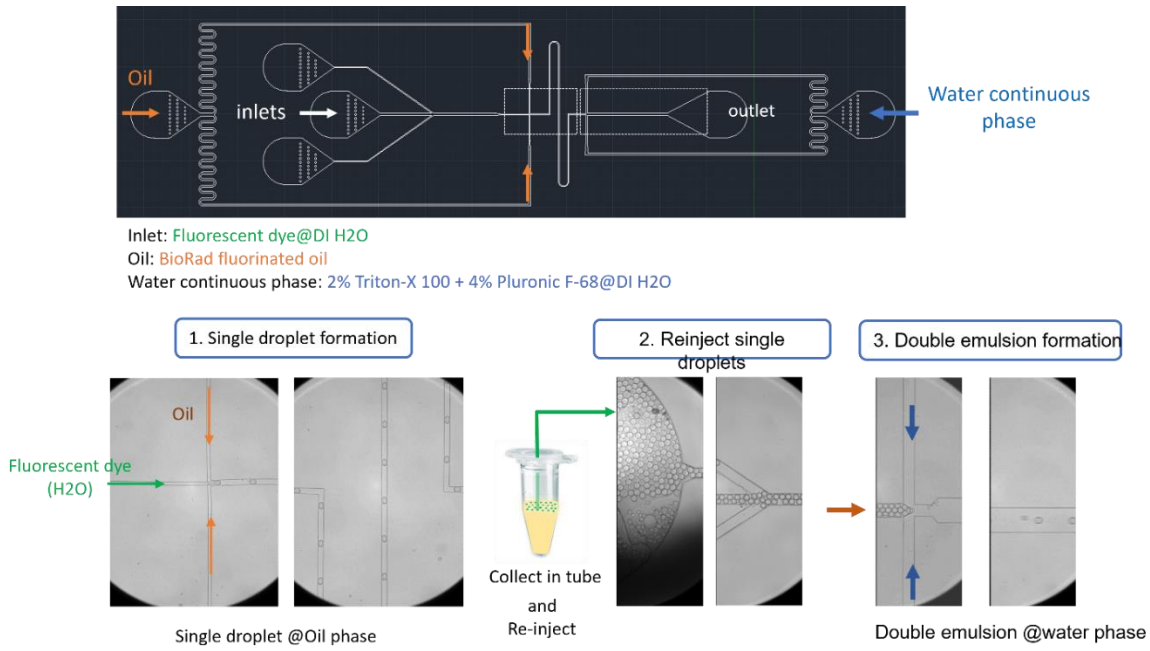

Figure 6.2. Image for double emulsion formation under microfluidic operation.

Fig. 6.3 is microscopic images for double emulsion as we used fluorescent dye as sample solution to demonstrate the uniformity and stability of double emulsion. The re-inject method can provide better uniformity of droplet because less oil containing between droplets, the oil layer of double emulsion is also thinner. The stability of double emulsion is staying a good shape with surfactant added water continuous phase as shown in Fig. 6.4(b), the stability is good after second day observation. Also in Fig. 6.5, we can observe the double emulsion remain the good shape when introduced in flow cytometry under high sheath flow (120uL/min) even though the high fluidic pressure makes the shape become ellipsoid.

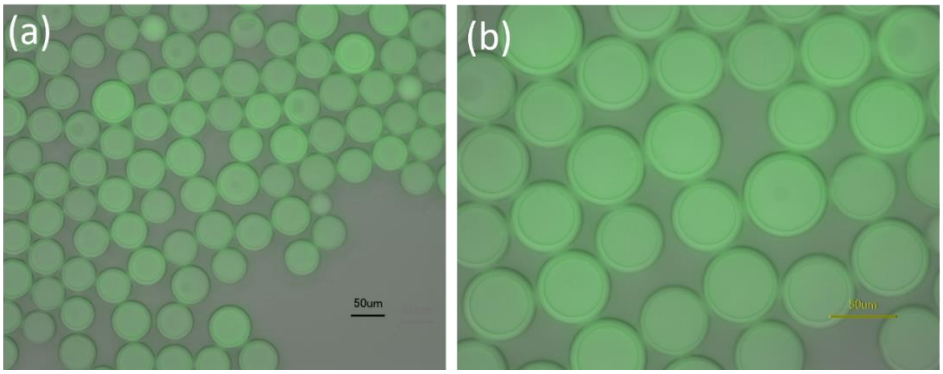

Figure 6.3. Microscopic image of double emulsion (merged with fluorescent signal)

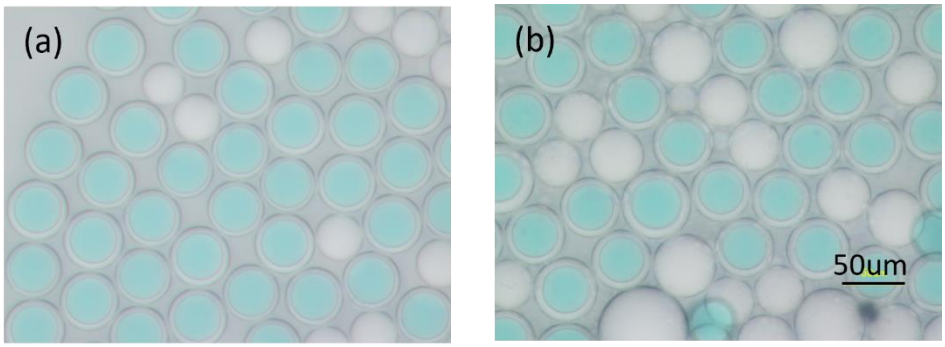

Figure 6.4. Double emulsions are remained in good shape after 2nd day observation. (a) The 1st day observation. (b) The 2nd day observation. (Store in water continuous phase in tube)

6.3 Experiment results and discussions

Double emulsion (cells/beads) applied with 2D image-guided sorting system

To demonstrate the capability of double emulsion can applied with 2D-imgage guided sorting system, we encapsulate different type of cells with different size of dragon green beads inside double emulsion to show that we are able to identify the cell type by image and beads with color or size, and it is able to be created into a library table for index of cell gene expression. First of all, the cell and beads image are shown in Fig. 6.5, the cell image under double emulsion is still clear, and we are able to observe the difference of morphology in different cell type. The blue column in Fig. 6.5 is CHO-GFP cell, we can clear

see its cell appearance of transmission image is different from Hela cell presented in red column. The cell size and appearance is distinguishable under transmission image comparison, even encapsulated in double emulsion that has an oil layer that we consider the high index of oil would affect the image formation. Besides, if the cell is GFP expressing, or colored with dye, the 2D sorting system still form the fluorescent image to recognize the cell position, as shown in the most upper three images in blue column in Fig. 6.5.

The images of beads are promising, because the color and size are distinguishable, and that would help us to create a table for multiple combination of cell and beads in record. As shown in Fig. 6.5, the smaller size is 5um beads, and the other is 7um. We can see the difference of beads and cells in transmission image by different contrast, and really tell the size of beads in difference. The clear comparison of bead size is also can be seen in fluorescent image, and different combination of beads are presented. One thing would mention here is that the fluorescence of cell and beads in this experiment is emitting around in the same wavelength range, green 508-520nm, and the intensity of dragon green beads is much stronger than GFP expressing, so we can only see the fluorescence from beads not from cell. In the 2D image sorting system, we have one PMT channel to receive transmission signal, and two PMTs fluorescent channel to receive different wavelength fluorescence signals by using different dichroic mirrors with different reflection bands. Therefore, the future experiment we can do is to use different color of beads to create more combination of beads type with cell, and it would enhance the comparison to cell's image and position as well as the informative index library table for cell phenotype to genotype connection.

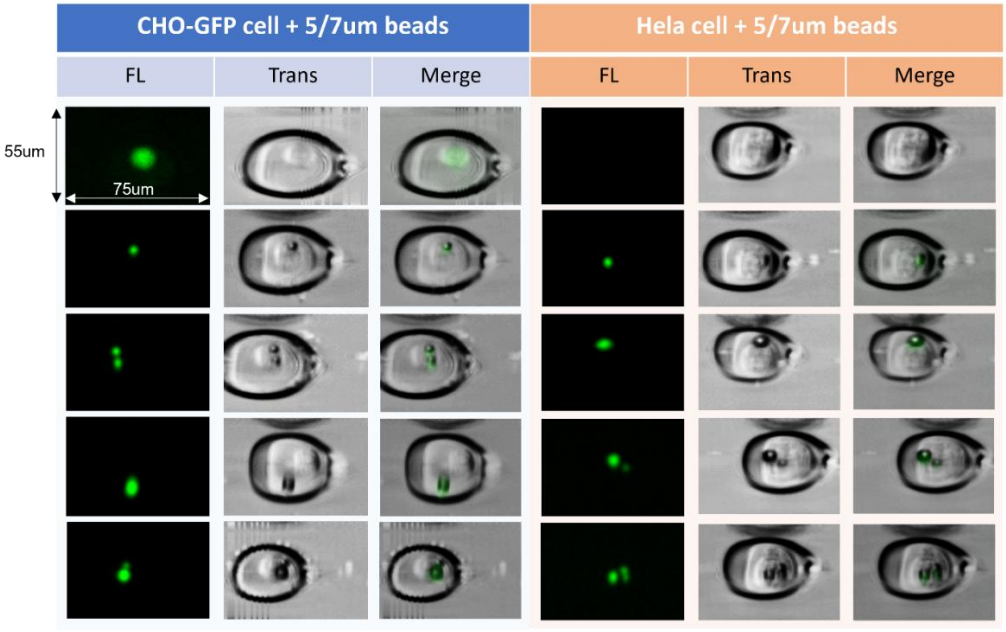

Figure 6.5. Double emulsion image with different cell type (blue column: CHO-cell, red column: Hela-cell) and beads with different size (5 and 7um).

6.4 Conclusions

The double emulsion technique is achieved to create uniform and size-controllable double droplets. The application of double emulsion is wide. In our study, we are combing this technique with 2D-image guided sorting system to create a informative index table for connecting cell morphology to its gene expression. The current results show the capability of our technique is ready for further study, even the long-term work is still undergoing. In those results, we can clearly observe the droplet contains different combination of cell and beads image: the different morphology occurs with different cell type, and the distinguishable beads' fluorescent color and size can be seen. Those informative image provide us as a record for further usage when we apply barcode sequence. We believe this work will provide unique and insightful information on connection of cell phenotype to genotype study.

6.5 Acknowledgement

Chapter 6, in part, is a reprint of the material as it is to be published later as: Chi-Yang Tseng, Zhilin Guo, Rui Tang, Lauren Waller, Yu-Hwa Lo. Single-Cell Sequencing Using Imaging-Compatible Double Emulsion Sorting. The dissertation author was the first author.

Chapter 7

Outlooks

In TIMES study, we first demonstrated the surface charge measurement, the charge density for different conditions of buffer can be quantified. Especially we successfully applied this methodology to molecular surface coverage measurement, which provides insightful information for sensor probe study, such as DNA hybridization and immunoassay on sensor surface study. Secondly, the protein-ligand interaction measurement was performed. The promising result shows that we can directly observe the dissociation constant from the data set without further data processing. This study provides unique method for molecular interaction measurement without surface modification, as well as gives insightful information for drug discovery study. Lastly, the paper-based measurement is developed. As most current works are based on colorimetric readout, this would cause false result, and the enzymatic reaction for color changing reaction is needed, leading some drawbacks on lateral flow assay study. This electrical readout method provides an alternative way for measuring reaction on paper, and it is also based on the strategy of labeling free and immobilization free.

Even we do show some advantages of our TIMES technique, some limits still exist and need to be improved. In protein-ligand interaction study, the protein-ligand complex is pre-mixed before the measurement, that is, the signal is not a real-time response from the molecular reaction. The much more insightful information from molecular interaction is hardly obtained through our measurement. Same as in paper-based measurement, we hardly obtain an ideal methodology for post analysis and have access to more insightful information to kinetic study. Such association and dissociation constants for different molecular interactions are currently hard to be obtained from our present work. To become a powerful technique that can be comparable to standard tool, such as SPR, we need keep working on improving those limits and enhancing TIMES capability.

In droplet-based single cell study, we successfully demonstrated the droplet-merging and double emulsion formation based on our microfluidic design. The droplet-merging device is different from other mechanisms, it is much feasible and portable. Our main goal is to identify neuron subtype using enhancer screening, and we are confident that we can achieve by using our droplet-merging design. This front-end technology application is one of the topics in this project, the main goal for specific-cell subtype identity study would have more impacts on biological and neurological research. Hopefully we will have more promising results in the future. On the other hand, the double emulsion technique that combined with our 2D-image guided sorting system also provides insightful information on single cell study. This is a unique platform that is able to relate cell gene expression to cell morphology and would provide information on cell genotype to phenotype study. Currently the progress of this project is in very preliminary stage, many situations we have not think of now may take into considerations in the future. We need to do more physical tests on cell lyse step and qPCR step in droplet-base operation to see if the condition we designed works or not. However, the current result shows our capability, and we are able to expand our idea on single-cell study using double emulsion technique.

Overall, either TIMES or droplet-based platform we developed has potential for many uses. With more effort input, we are able to expand their applications in more research area.

References

1. Naresh, V.; Lee, N., A Review on Biosensors and Recent Development of Nanostructured Materials-Enabled Biosensors. Sensors 2021, 21 (4), 1109.

2. Luka, G.; Ahmadi, A.; Najjaran, H.; Alocilja, E.; DeRosa, M.; Wolthers, K.; Malki, A.; Aziz, H.; Althani, A.; Hoorfar, M., Microfluidics Integrated Biosensors: A Leading Technology towards Lab-on-a-Chip and Sensing Applications. Sensors 2015, 15 (12), 30011-30031

3. Zhou, Q.; Kwa, T.; Gao, Y.; Liu, Y.; Rahimian, A.; Revzin, A., On-chip regeneration of aptasensors for monitoring cell secretion. Lab Chip 2014, 14 (2), 276-279.

4. Hellmann, J., Deciding to resuscitate extremely premature babies: How do parents and neonatologists engage in the decision? Yearbook of Neonatal and Perinatal Medicine 2008, 2008, 334-336.

5. Gu, S.; Lu, Y.; Ding, Y.; Li, L.; Song, H.; Wang, J.; Wu, Q., A droplet-based microfluidic electrochemical sensor using platinum-black microelectrode and its application in high sensitive glucose sensing. Biosensors and Bioelectronics 2014, 55, 106-112.

6. Grahame, D. C., The Electrical Double Layer and the Theory of Electrocapillarity. Chemical Reviews 1947, 41 (3), 441-501.

7. Parsons, R., The electrical double layer: recent experimental and theoretical developments. Chemical Reviews 1990, 90 (5), 813-826.

8. Glosli, J. N.; Philpott, M. R., Molecular dynamics simulation of adsorption of ions from aqueous media onto charged electrodes. The Journal of Chemical Physics 1992, 96 (9), 6962-6969.

9. Wang, S.; Li, S.; Cao, Z.; Yan, T., Molecular Dynamic Simulations of Ionic Liquids at Graphite Surface. The Journal of Physical Chemistry C 2010, 114 (2), 990-995.

10. Biesheuvel, P. M.; van Soestbergen, M., Counterion volume effects in mixed electrical double layers. Journal of Colloid and Interface Science 2007, 316 (2), 490-499.

11. Jing, D.; Bhushan, B., Quantification of Surface Charge Density and Its Effect on Boundary Slip. Langmuir 2013, 29 (23), 6953-6963.

12. Butt, H. J., Measuring local surface charge densities in electrolyte solutions with a scanning force microscope. Biophysical journal 1992, 63 (2), 578-82.

13. Ishino, T.; Hieda, H.; Tanaka, K.; Gemma, N., Imaging charged functional groups with an atomic force microscope operated in aqueous solutions. Journal of Electroanalytical Chemistry 1997, 438 (1), 225-230.

14. Larson, I.; Pugh, R. J., Qualitative Adsorption Measurements with an Atomic Force Microscope. Langmuir 1998, 14 (20), 5676-5679.

15. Wu, Y.; Gupta, C.; Shannon, M. A., Effect of Solution Concentration, Surface Bias and Protonation on the Dynamic Response of Amplitude-Modulated Atomic Force Microscopy in Water. Langmuir 2008, 24 (19), 10817-10824.

16. Wu, Y.; Misra, S.; Karacor, M. B.; Prakash, S.; Shannon, M. A., Dynamic Response of AFM Cantilevers to Dissimilar Functionalized Silica Surfaces in Aqueous Electrolyte Solutions. Langmuir 2010, 26 (22), 16963-16972.

17. Shan, X.; Huang, X.; Foley, K. J.; Zhang, P.; Chen, K.; Wang, S.; Tao, N., Measuring surface charge density and particle height using surface plasmon resonance technique. Analytical chemistry 2010, 82 (1), 234-40.

18. Shan, X.; Wang, S.; Tao, N., Study of single particle charge and Brownian motions with surface plasmon resonance. Applied Physics Letters 2010, 97 (22), 223703.

19. Afonso, M. D.; Hagmeyer, G.; Gimbel, R., Streaming potential measurements to assess the variation of nanofiltration membranes surface charge with the concentration of salt solutions. Separation and Purification Technology 2001, 22-23, 529-541.

20. Datta, S.; Conlisk, A. T.; Kanani, D. M.; Zydney, A. L.; Fissell, W. H.; Roy, S., Characterizing the surface charge of synthetic nanomembranes by the streaming potential method. Journal of Colloid and Interface Science 2010, 348 (1), 85-95.

21. Kim, K. J.; Fane, A. G.; Nystrom, M.; Pihlajamaki, A.; Bowen, W. R.; Mukhtar, H., Evaluation of electroosmosis and streaming potential for measurement of electric charges of polymeric membranes. Journal of Membrane Science 1996, 116 (2), 149-159.

22. Molina, C.; Victoria, L.; Arenas, A.; Ibáñez, J. A., Streaming potential and surface charge density of microporous membranes with pore diameter in the range of thickness. Journal of Membrane Science 1999, 163 (2), 239-255.

23. Peeters, J. M. M.; Mulder, M. H. V.; Strathmann, H., Streaming potential measurements as a characterization method for nanofiltration membranes. Colloids and Surfaces A: Physicochemical and Engineering Aspects 1999, 150 (1), 247-259.

24. Chvedov, D.; Logan, E. L. B., Surface charge properties of oxides and hydroxides formed on metal substrates determined by contact angle titration. Colloids and Surfaces A: Physicochemical and Engineering Aspects 2004, 240 (1-3), 211-223.

25. Horiuchi, H.; Nikolov, A.; Wasan, D. T., Calculation of the surface potential and surface charge density by measurement of the three-phase contact angle. Journal of Colloid and Interface Science 2012, 385 (1), 218-224.

26. Hurwitz, G.; Guillen, G. R.; Hoek, E. M. V., Probing polyamide membrane surface charge, zeta potential, wettability, and hydrophilicity with contact angle measurements. Journal of Membrane Science 2010, 349 (1-2), 349-357.

27. Ahmed, F. E.; Wiley, J. E.; Weidner, D. A.; Bonnerup, C.; Mota, H., Surface plasmon resonance (SPR) spectrometry as a tool to analyze nucleic acid-protein interactions in crude cellular extracts. Cancer genomics & proteomics 2010, 7 (6), 303-9.

28. Helmerhorst, E.; Chandler, D. J.; Nussio, M.; Mamotte, C. D., Real-time and Label-free Bio-sensing of Molecular Interactions by Surface Plasmon Resonance: A Laboratory Medicine Perspective. The Clinical biochemist. Reviews 2012, 33 (4), 161-73.

29. Zhang, T.; Ku, T.-H.; Han, Y.; Subramanian, R.; Niaz, I. A.; Luo, H.; Chang, D.; Huang, J.-J.; Lo, Y.-H., Transient Induced Molecular Electronic Spectroscopy (TIMES) for study of protein-ligand interactions. Scientific Reports 2016, 6 (1).

30. Zhang, T.; Wei, T.; Han, Y.; Ma, H.; Samieegohar, M.; Chen, P.-W.; Lian, I.; Lo, Y.-H., Protein–Ligand Interaction Detection with a Novel Method of Transient Induced Molecular Electronic Spectroscopy (TIMES): Experimental and Theoretical Studies. ACS Central Science 2016, 2 (11), 834-842.

31. Rizo, R.; Sitta, E.; Herrero, E.; Climent, V.; Feliu, J. M., Towards the understanding of the interfacial pH scale at Pt(1 1 1) electrodes. Electrochimica Acta 2015, 162, 138-145.

32. Steel, A. B.; Levicky, R. L.; Herne, T. M.; Tarlov, M. J., Immobilization of nucleic acids at solid surfaces: effect of oligonucleotide length on layer assembly. Biophysical journal 2000, 79 (2), 975-81.

33. Drews, J., Drug discovery: a historical perspective. Science 2000, 287 (5460), 1960-4.

34. Neužil, P.; Giselbrecht, S.; Länge, K.; Huang, T. J.; Manz, A., Revisiting lab-on-a-chip technology for drug discovery. Nature Reviews Drug Discovery 2012, 11 (8), 620-632.

35. Fägerstam, L. G.; Frostell-Karlsson, A.; Karlsson, R.; Persson, B.; Rönnberg, I., Biospecific interaction analysis using surface plasmon resonance detection applied to kinetic, binding site and concentration analysis. Journal of chromatography 1992, 597 (1-2), 397-410.

36. Di Primo, C.; Lebars, I., Determination of refractive index increment ratios for protein–nucleic acid complexes by surface plasmon resonance. Analytical Biochemistry 2007, 368 (2), 148-155.

37. Mayer, K. M.; Hafner, J. H., Localized Surface Plasmon Resonance Sensors. Chemical Reviews 2011, 111 (6), 3828-3857.

38. Cooper, M. A., Optical biosensors in drug discovery. Nature Reviews Drug Discovery 2002, 1 (7), 515-528.

39. Leavitt, S.; Freire, E., Direct measurement of protein binding energetics by isothermal titration calorimetry. Current Opinion in Structural Biology 2001, 11 (5), 560-566.

40. Keller, S.; Vargas, C.; Zhao, H.; Piszczek, G.; Brautigam, C. A.; Schuck, P., High-Precision Isothermal Titration Calorimetry with Automated Peak-Shape Analysis. Analytical chemistry 2012, 84 (11), 5066-5073.

41. Holdgate, G., Isothermal Titration Calorimetry and Differential Scanning Calorimetry. 2009, 572, 101-133.

42. Mocz, G.; Ross, J. A., Fluorescence Techniques in Analysis of Protein–Ligand Interactions. 2013, 1008, 169-210.

43. Endoh, T.; Funabashi, H.; Mie, M.; Kobatake, E., Method for Detection of Specific Nucleic Acids by Recombinant Protein with Fluorescent Resonance Energy Transfer. Analytical chemistry 2005, 77 (14), 4308-4314.

44. Lee, M. M.; Peterson, B. R., Quantification of Small Molecule–Protein Interactions using FRET between Tryptophan and the Pacific Blue Fluorophore. ACS Omega 2016, 1 (6), 1266-1276.

45. Star, A.; Gabriel, J.-C. P.; Bradley, K.; Grüner, G., Electronic Detection of Specific Protein Binding Using Nanotube FET Devices. Nano Letters 2003, 3 (4), 459-463.

46. Maehashi, K.; Katsura, T.; Kerman, K.; Takamura, Y.; Matsumoto, K.; Tamiya, E., Label-Free Protein Biosensor Based on Aptamer-Modified Carbon Nanotube Field-Effect Transistors. Analytical chemistry 2007, 79 (2), 782-787.

47. Schöning, M. J.; Poghossian, A., Recent advances in biologically sensitive field-effect transistors (BioFETs). The Analyst 2002, 127 (9), 1137-1151.

48. Münzer, A. M.; Seo, W.; Morgan, G. J.; Michael, Z. P.; Zhao, Y.; Melzer, K.; Scarpa, G.; Star, A., Sensing Reversible Protein–Ligand Interactions with Single-Walled Carbon Nanotube Field-Effect Transistors. The Journal of Physical Chemistry C 2014, 118 (31), 17193-17199.

49. Pan, Y.; Duncombe, T. A.; Kellenberger, C. A.; Hammond, M. C.; Herr, A. E., High-Throughput Electrophoretic Mobility Shift Assays for Quantitative Analysis of Molecular Binding Reactions. Analytical chemistry 2014, 86 (20), 10357-10364.

50. Pan, Y.; Sackmann, E. K.; Wypisniak, K.; Hornsby, M.; Datwani, S. S.; Herr, A. E., Determination of equilibrium dissociation constants for recombinant antibodies by high-throughput affinity electrophoresis. Scientific Reports 2016, 6 (1).

51. Garner, M. M.; Revzin, A., A gel electrophoresis method for quantifying the binding of proteins to specific DNA regions: application to components of the Escherichia coli lactose operon regulatory system+. Nucleic Acids Research 1981, 9 (13), 3047-3060.

52. Preus, S.; Wilhelmsson, L. M., Advances in Quantitative FRET-Based Methods for Studying Nucleic Acids. ChemBioChem 2012, 13 (14), 1990-2001.

53. Hellman, L. M.; Fried, M. G., Electrophoretic mobility shift assay (EMSA) for detecting protein–nucleic acid interactions. Nature Protocols 2007, 2 (8), 1849-1861.

54. Du, X.; Li, Y.; Xia, Y.-L.; Ai, S.-M.; Liang, J.; Sang, P.; Ji, X.-L.; Liu, S.-Q., Insights into Protein–Ligand Interactions: Mechanisms, Models, and Methods. International Journal of Molecular Sciences 2016, 17 (2), 144.

55. Chen, P.-W.; Tseng, C.-Y.; Shi, F.; Bi, B.; Lo, Y.-H., Measuring Electric Charge and Molecular Coverage on Electrode Surface from Transient Induced Molecular Electronic Signal (TIMES). Scientific Reports 2019, 9 (1).

56. Jecklin, M. C.; Touboul, D.; Bovet, C.; Wortmann, A.; Zenobi, R., Which electrospray-based ionization method best reflects protein-ligand interactions found in solution? A comparison of ESI, nanoESI, and ESSI for the determination of dissociation constants with mass spectrometry. Journal of the American Society for Mass Spectrometry 2011, 19 (3), 332-343.

57. Svobodová, J.; Mathur, S.; Muck, A.; Letzel, T.; Svatoš, A., Microchip-ESI-MS determination of dissociation constant of the lysozyme-NAG3 complex. Electrophoresis 2010, 31 (15), 2680-2685.

58. Tran, D. T.; Janssen, K. P. F.; Pollet, J.; Lammertyn, E.; Anné, J.; Van Schepdael, A.; Lammertyn, J., Selection and Characterization of DNA Aptamers for Egg White Lysozyme. Molecules 2010, 15 (3), 1127-1140.

59. Doucet, N.; Jayasundera, T. B.; Simonović, M.; Loria, J. P., The crystal structure of ribonuclease A in complex with thymidine-3´-monophosphate provides further insight into ligand binding. Proteins: Structure, Function, and Bioinformatics 2010, 2459-68.

60. Hu, J.; Wang, S.; Wang, L.; Li, F.; Pingguan-Murphy, B.; Lu, T. J.; Xu, F., Advances in paper-based point-of-care diagnostics. Biosensors and Bioelectronics 2014, 54, 585-597.

61. Cate, D. M.; Adkins, J. A.; Mettakoonpitak, J.; Henry, C. S., Recent Developments in Paper-Based Microfluidic Devices. Analytical chemistry 2014, 87 (1), 19-41.

62. Shen, L. L.; Zhang, G. R.; Etzold, B. J. M., Paper-Based Microfluidics for Electrochemical Applications. ChemElectroChem 2019, 7 (1), 10-30.

63. Yetisen, A. K.; Akram, M. S.; Lowe, C. R., Paper-based microfluidic point-of-care diagnostic devices. Lab on a Chip 2013, 13 (12), 2210.

64. Martinez, A. W.; Phillips, S. T.; Butte, M. J.; Whitesides, G. M., Patterned Paper as a Platform for Inexpensive, Low-Volume, Portable Bioassays. Angewandte Chemie International Edition 2007, 46 (8), 1318-1320.

65. Cinti, S.; Minotti, C.; Moscone, D.; Palleschi, G.; Arduini, F., Fully integrated ready-to-use paper-based electrochemical biosensor to detect nerve agents. Biosensors and Bioelectronics 2017, 93, 46-51.

66. Dungchai, W.; Chailapakul, O.; Henry, C. S., Electrochemical Detection for Paper-Based Microfluidics. Analytical chemistry 2009, 81 (14), 5821-5826.

67. Nie, Z.; Nijhuis, C. A.; Gong, J.; Chen, X.; Kumachev, A.; Martinez, A. W.; Narovlyansky, M.; Whitesides, G. M., Electrochemical sensing in paper-based microfluidic devices. Lab Chip 2010, 10 (4), 477-483.

68. Kokkinos, C.; Economou, A.; Giokas, D., Paper-based device with a sputtered tin-film electrode for the voltammetric determination of Cd(II) and Zn(II). Sensors and Actuators B: Chemical 2018, 260, 223-226.

69. Sánchez-Calvo, A.; Fernández-Abedul, M. T.; Blanco-López, M. C.; Costa-García, A., Paper-based electrochemical transducer modified with nanomaterials for mercury determination in environmental waters. Sensors and Actuators B: Chemical 2019, 290, 87-92.

70. Cincotto, F. H.; Fava, E. L.; Moraes, F. C.; Fatibello-Filho, O.; Faria, R. C., A new disposable microfluidic electrochemical paper-based device for the simultaneous determination of clinical biomarkers. Talanta 2019, 195, 62-68.

71. Pungjunun, K.; Chaiyo, S.; Jantrahong, I.; Nantaphol, S.; Siangproh, W.; Chailapakul, O., Anodic stripping voltammetric determination of total arsenic using a gold nanoparticle-modified boron-doped diamond electrode on a paper-based device. Microchimica Acta 2018, 185 (7).

72. Shen, L.-L.; Zhang, G.-R.; Li, W.; Biesalski, M.; Etzold, B. J. M., Modifier-Free Microfluidic Electrochemical Sensor for Heavy-Metal Detection. ACS Omega 2017, 2 (8), 4593-4603.

73. Ruecha, N.; Chailapakul, O.; Suzuki, K.; Citterio, D., Fully Inkjet-Printed Paper-Based Potentiometric Ion-Sensing Devices. Analytical chemistry 2017, 89 (19), 10608-10616.

74. Li, X.; Nie, Z.; Cheng, C. M.; Goodale, A. B.; Whitesides, G. M., Paper-based electrochemical ELISA. 14th International Conference on Miniaturized Systems for Chemistry and Life Sciences 2010, MicroTAS 2010 2010, 3, 1487-1489.

75. Limoges, B.; Marchal, D.; Mavré, F.; Savéant, J.-M.; Schöllhorn, B., Theory and Practice of Enzyme Bioaffinity Electrodes. Direct Electrochemical Product Detection. Journal of the American Chemical Society 2008, 130 (23), 7259-7275.

76. Martínez-García, G.; Pérez-Julián, E.; Agüí, L.; Cabré, N.; Joven, J.; Yáñez-Sedeño, P.; Pingarrón, J. M., An Electrochemical Enzyme Biosensor for 3-Hydroxybutyrate Detection Using Screen-Printed Electrodes Modified by Reduced Graphene Oxide and Thionine. Biosensors 2017, 7 (4), 50.

77. Ruiz-Vega, G.; Kitsara, M.; Pellitero, M. A.; Baldrich, E.; del Campo, F. J., Electrochemical Lateral Flow Devices: Towards Rapid Immunomagnetic Assays. ChemElectroChem 2017, 4 (4), 880-889.

78. Cinti, S.; Colozza, N.; Cacciotti, I.; Moscone, D.; Polomoshnov, M.; Sowade, E.; Baumann, R. R.; Arduini, F., Electroanalysis moves towards paper-based printed electronics: carbon black nanomodified inkjet-printed sensor for ascorbic acid detection as a case study. Sensors and Actuators B: Chemical 2018, 265, 155-160.

79. Silva, M. K. L.; Sousa, G. S.; Simoes, R. P.; Cesarino, I., Fabrication of paper-based analytical devices using a PLA 3D-printed stencil for electrochemical determination of chloroquine and escitalopram. Journal of Solid State Electrochemistry 2021, 26 (2), 581-586.

80. Núnez-Bajo, E.; Blanco-López, M. C.; Costa-García, A.; Fernández-Abedul, M. T., In situ gold-nanoparticle electrogeneration on gold films deposited on paper for non-enzymatic electrochemical determination of glucose. Talanta 2018, 178, 160-165.

81. Chen, P.-W.; Tseng, C.-Y.; Shi, F.; Bi, B.; Lo, Y.-H., Detecting Protein–Ligand Interaction from Integrated Transient Induced Molecular Electronic Signal (i-TIMES). Analytical chemistry 2020, 92 (5), 3852-3859.

82. Bottom, C. B.; Hanna, S. S.; Siehr, D. J., Mechanism of the ninhydrin reaction. Biochemical Education 1978, 6 (1), 4-5.

83. Friedman, M.; Sigel, C. W., A Kinetic Study of the Ninhydrin Reaction*. Biochemistry 2002, 5 (2), 478-485.

84. Wu, Y.; Hussain, M.; Fassihi, R., Development of a simple analytical methodology for determination of glucosamine release from modified release matrix tablets. Journal of Pharmaceutical and Biomedical Analysis 2005, 38 (2), 263-269.

85. Karlsson, R.; Fägerstam, L.; Nilshans, H.; Persson, B., Analysis of active antibody concentration. Separation of affinity and concentration parameters. Journal of immunological methods 1993, 166 (1), 75-84.

86. Munoz, E. M.; Correa, J.; Riguera, R.; Fernandez-Megia, E., Real-Time Evaluation of Binding Mechanisms in Multivalent Interactions: A Surface Plasmon Resonance Kinetic Approach. Journal of the American Chemical Society 2013, 135 (16), 5966-5969.

87. Sadana, A.; Vo-Dinh, T., Antibody-antigen binding kinetics. A model for multivalency antibodies for large antigen systems. Applied biochemistry and biotechnology 1997, 67 (1-2), 1-22.

88. Wamsley, B.; Fishell, G., Genetic and activity-dependent mechanisms underlying interneuron diversity. Nature Reviews Neuroscience 2017, 18 (5), 299-309.

89. Courchesne, E.; Mouton, P. R.; Calhoun, M. E.; Semendeferi, K.; Ahrens-Barbeau, C.; Hallet, M. J.; Barnes, C. C.; Pierce, K., Neuron number and size in prefrontal cortex of children with autism. Jama 2011, 306 (18), 2001-10.

90. Ross, C. A.; Margolis, R. L.; Reading, S. A. J.; Pletnikov, M.; Coyle, J. T., Neurobiology of Schizophrenia. Neuron 2006, 52 (1), 139-153.

91. Muñoz, W.; Tremblay, R.; Levenstein, D.; Rudy, B., Layer-specific modulation of neocortical dendritic inhibition during active wakefulness. Science 2017, 355 (6328), 954-959.

92. He, M.; Tucciarone, J.; Lee, S.; Nigro, Maximiliano J.; Kim, Y.; Levine, Jesse M.; Kelly, Sean M.; Krugikov, I.; Wu, P.; Chen, Y.; Gong, L.; Hou, Y.; Osten, P.; Rudy, B.; Huang, Z. J., Strategies and Tools for Combinatorial Targeting of GABAergic Neurons in Mouse Cerebral Cortex. Neuron 2016, 91 (6), 1228-1243.

93. Graybuck, L. T.; Sedeño-Cortés, A. E.; Nguyen, T. N.; Walker, M.; Szelenyi, E.; Lenz, G.; Sieverts, L. A.; Kim, T. K.; Garren, E.; Kalmbach, B.; Yao, S.; Mortrud, M.; Mich, J.; Goldy, J.; Smith, K.; Dee, N.; Yao, Z.; Cetin, A.; Levi, B.; Lein, E.; Ting, J.; Zeng, H.; Daigle, T.; Tasic, B., Prospective, brain-wide labeling of neuronal subclasses with enhancer-driven AAVs. bioRxiv 2019, 525014.

94. He, Y.; Gorkin, D. U.; Dickel, D. E.; Nery, J. R.; Castanon, R. G.; Lee, A. Y.; Shen, Y.; Visel, A.; Pennacchio, L. A.; Ren, B.; Ecker, J. R., Improved regulatory element prediction based on tissue-specific local epigenomic signatures. Proceedings of the National Academy of Sciences 2017, 114 (9).

95. Luo, C.; Liu, H.; Xie, F.; Armand, E. J.; Siletti, K.; Bakken, T. E.; Fang, R.; Doyle, W. I.; Hodge, R. D.; Hu, L.; Wang, B.-A.; Zhang, Z.; Preissl, S.; Lee, D.-S.; Zhou, J.; Niu, S.-Y.; Castanon, R.; Bartlett, A.; Rivkin, A.; Wang, X.; Lucero, J.; Nery, J. R.; Davis, D. A.; Mash, D. C.; Dixon, J. R.; Linnarsson, S.; Lein, E.; Behrens, M. M.; Ren, B.; Mukamel, E. A.; Ecker, J. R., Single nucleus multi-omics links human cortical cell regulatory genome diversity to disease risk variants. bioRxiv 2019, 2019.12.11.873398.

96. Picelli, S.; Björklund, Å. K.; Faridani, O. R.; Sagasser, S.; Winberg, G.; Sandberg, R., Smart-seq2 for sensitive full-length transcriptome profiling in single cells. Nature Methods 2013, 10 (11), 1096-1098.

97. Hashimshony, T.; Senderovich, N.; Avital, G.; Klochendler, A.; de Leeuw, Y.; Anavy, L.; Gennert, D.; Li, S.; Livak, K. J.; Rozenblatt-Rosen, O.; Dor, Y.; Regev, A.; Yanai, I., CEL-Seq2: sensitive highly-multiplexed single-cell RNA-Seq. Genome Biology 2016, 17 (1).

98. Zhang, X.; Li, T.; Liu, F.; Chen, Y.; Yao, J.; Li, Z.; Huang, Y.; Wang, J., Comparative Analysis of Droplet-Based Ultra-High-Throughput Single-Cell RNA-Seq Systems. Molecular Cell 2019, 73 (1), 130-142.e5.

99. Mazutis, L.; Baret, J.-C.; Griffiths, A. D., A fast and efficient microfluidic system for highly selective one-to-one droplet fusion. Lab on a Chip 2009, 9 (18), 2665.

100. Akartuna, I.; Aubrecht, D. M.; Kodger, T. E.; Weitz, D. A., Chemically induced coalescence in droplet-based microfluidics. Lab on a Chip 2015, 15 (4), 1140-1144.

101. Frenz, L.; El Harrak, A.; Pauly, M.; Bégin-Colin, S.; Griffiths, A. D.; Baret, J.-C., Droplet-Based Microreactors for the Synthesis of Magnetic Iron Oxide Nanoparticles. Angewandte Chemie International Edition 2008, 47 (36), 6817-6820.

102. Abate, A. R.; Hung, T.; Mary, P.; Agresti, J. J.; Weitz, D. A., High-throughput injection with microfluidics using picoinjectors. Proceedings of the National Academy of Sciences 2010, 107 (45), 19163-19166.

103. Baroud, C. N.; Robert de Saint Vincent, M.; Delville, J.-P., An optical toolbox for total control of droplet microfluidics. Lab on a Chip 2007, 7 (8), 1029.

104. Sesen, M.; Fakhfouri, A.; Neild, A., Coalescence of Surfactant-Stabilized Adjacent Droplets Using Surface Acoustic Waves. Analytical chemistry 2019, 91 (12), 7538-7545.

105. Shen, F.; Li, Y.; Liu, Z.-M.; Cao, R.-T.; Wang, G.-R., Advances in Micro-Droplets Coalescence Using Microfluidics. Chinese Journal of Analytical Chemistry 2015, 43 (12), 1942-1954.

106. Bremond, N.; Thiam, A. R.; Bibette, J., Decompressing Emulsion Droplets Favors Coalescence. Physical Review Letters 2008, 100 (2).

107. Niu, X.; Gulati, S.; Edel, J. B.; deMello, A. J., Pillar-induced droplet merging in microfluidic circuits. Lab on a Chip 2008, 8 (11), 1837.

108. Tullis, J.; Park, C. L.; Abbyad, P., Selective fusion of anchored droplets via changes in surfactant concentration. Lab Chip 2014, 14 (17), 3285-3289.

109. Baret, J.-C.; Miller, O. J.; Taly, V.; Ryckelynck, M.; El-Harrak, A.; Frenz, L.; Rick, C.; Samuels, M. L.; Hutchison, J. B.; Agresti, J. J.; Link, D. R.; Weitz, D. A.; Griffiths, A. D., Fluorescence-activated droplet sorting (FADS): efficient microfluidic cell sorting based on enzymatic activity. Lab on a Chip 2009, 9 (13), 1850.

110. Sciambi, A.; Abate, A. R., Accurate microfluidic sorting of droplets at 30 kHz. Lab on a Chip 2015, 15 (1), 47-51.

111. Gielen, F.; Hours, R.; Emond, S.; Fischlechner, M.; Schell, U.; Hollfelder, F., Ultrahigh-throughput–directed enzyme evolution by absorbance-activated droplet sorting (AADS). Proceedings of the National Academy of Sciences 2016, 113 (47), E7383-E7389.

112. Angerer, P.; Simon, L.; Tritschler, S.; Wolf, F. A.; Fischer, D.; Theis, F. J., Single cells make big data: New challenges and opportunities in transcriptomics. Current Opinion in Systems Biology 2017, 4, 85-91.

113. Gross, A.; Schoendube, J.; Zimmermann, S.; Steeb, M.; Zengerle, R.; Koltay, P., Technologies for Single-Cell Isolation. International Journal of Molecular Sciences 2015, 16 (8), 16897-16919.

114. Saliba, A.-E.; Westermann, A. J.; Gorski, S. A.; Vogel, J., Single-cell RNA-seq: advances and future challenges. Nucleic Acids Research 2014, 42 (14), 8845-8860.

115. Bernath, K.; Hai, M.; Mastrobattista, E.; Griffiths, A. D.; Magdassi, S.; Tawfik, D. S., In vitro compartmentalization by double emulsions: sorting and gene enrichment by fluorescence activated cell sorting. Analytical Biochemistry 2004, 325 (1), 151-157.

116. Lim, S. W.; Abate, A. R., Ultrahigh-throughput sorting of microfluidic drops with flow cytometry. Lab on a Chip 2013, 13 (23), 4563.

117. Sukovich, D. J.; Lance, S. T.; Abate, A. R., Sequence specific sorting of DNA molecules with FACS using 3dPCR. Scientific Reports 2017, 7 (1).

118. Zinchenko, A.; Devenish, S. R. A.; Kintses, B.; Colin, P.-Y.; Fischlechner, M.; Hollfelder, F., One in a Million: Flow Cytometric Sorting of Single Cell-Lysate Assays in Monodisperse Picolitre Double Emulsion Droplets for Directed Evolution. Analytical chemistry 2014, 86 (5), 2526-2533.

119. Deng, Q.; Ramsköld, D.; Reinius, B.; Sandberg, R., Single-cell RNA-seq reveals dynamic, random monoallelic gene expression in mammalian cells. Science 2014, 343 (6167), 193-6.

120. Patel Anoop, P.; Tirosh, I.; Trombetta John, J.; Shalek Alex, K.; Gillespie Shawn, M.; Wakimoto, H.; Cahill Daniel, P.; Nahed Brian, V.; Curry William, T.; Martuza Robert, L.; Louis David, N.; Rozenblatt-Rosen, O.; Suvà Mario, L.; Regev, A.; Bernstein Bradley, E., Single-cell RNA-seq highlights intratumoral heterogeneity in primary glioblastoma. Science 2014, 344 (6190), 1396-1401.

121. Villani, A.-C.; Satija, R.; Reynolds, G.; Sarkizova, S.; Shekhar, K.; Fletcher, J.; Griesbeck, M.; Butler, A.; Zheng, S.; Lazo, S.; Jardine, L.; Dixon, D.; Stephenson, E.; Nilsson, E.; Grundberg, I.; McDonald, D.; Filby, A.; Li, W.; De Jager Philip, L.; Rozenblatt-Rosen, O.; Lane Andrew, A.; Haniffa, M.; Regev, A.; Hacohen, N., Single-cell RNA-seq reveals new types of human blood dendritic cells, monocytes, and progenitors. Science 2017, 356 (6335), eaah4573.

122. Bentzen, A. K.; Marquard, A. M.; Lyngaa, R.; Saini, S. K.; Ramskov, S.; Donia, M.; Such, L.; Furness, A. J. S.; McGranahan, N.; Rosenthal, R.; Straten, P. t.; Szallasi, Z.; Svane, I. M.; Swanton, C.; Quezada, S. A.; Jakobsen, S. N.; Eklund, A. C.; Hadrup, S. R., Large-scale detection of antigen-specific T cells using peptide-MHC-I multimers labeled with DNA barcodes. Nature Biotechnology 2016, 34 (10), 1037-1045.

123. Dash, P.; Fiore-Gartland, A. J.; Hertz, T.; Wang, G. C.; Sharma, S.; Souquette, A.; Crawford, J. C.; Clemens, E. B.; Nguyen, T. H. O.; Kedzierska, K.; La Gruta, N. L.; Bradley, P.; Thomas, P. G., Quantifiable predictive features define epitope-specific T cell receptor repertoires. Nature 2017, 547 (7661), 89-93.

124. Peterson, V. M.; Zhang, K. X.; Kumar, N.; Wong, J.; Li, L.; Wilson, D. C.; Moore, R.; McClanahan, T. K.; Sadekova, S.; Klappenbach, J. A., Multiplexed quantification of proteins and transcripts in single cells. Nature Biotechnology 2017, 35 (10), 936-939.

125. Stoeckius, M.; Hafemeister, C.; Stephenson, W.; Houck-Loomis, B.; Chattopadhyay, P. K.; Swerdlow, H.; Satija, R.; Smibert, P., Simultaneous epitope and transcriptome measurement in single cells. Nature methods 2017, 14 (9), 865-868.

126. Cao, J.; Packer Jonathan, S.; Ramani, V.; Cusanovich Darren, A.; Huynh, C.; Daza, R.; Qiu, X.; Lee, C.; Furlan Scott, N.; Steemers Frank, J.; Adey, A.; Waterston Robert, H.; Trapnell, C.; Shendure, J., Comprehensive single-cell transcriptional profiling of a multicellular organism. Science 2017, 357 (6352), 661-667.

127. Shahi, P.; Kim, S. C.; Haliburton, J. R.; Gartner, Z. J.; Abate, A. R., Abseq: Ultrahigh-throughput single cell protein profiling with droplet microfluidic barcoding. Scientific Reports 2017, 7 (1).

128. Smallwood, S. A.; Lee, H. J.; Angermueller, C.; Krueger, F.; Saadeh, H.; Peat, J.; Andrews, S. R.; Stegle, O.; Reik, W.; Kelsey, G., Single-cell genome-wide bisulfite sequencing for assessing epigenetic heterogeneity. Nature Methods 2014, 11 (8), 817-820.

129. Cusanovich Darren, A.; Daza, R.; Adey, A.; Pliner Hannah, A.; Christiansen, L.; Gunderson Kevin, L.; Steemers Frank, J.; Trapnell, C.; Shendure, J., Multiplex single-cell profiling of chromatin accessibility by combinatorial cellular indexing. Science 2015, 348 (6237), 910-914.

130. Vitak, S. A.; Torkenczy, K. A.; Rosenkrantz, J. L.; Fields, A. J.; Christiansen, L.; Wong, M. H.; Carbone, L.; Steemers, F. J.; Adey, A., Sequencing thousands of single-cell genomes with combinatorial indexing. Nature Methods 2017, 14 (3), 302-308.

131. Azizi, E.; Carr, A. J.; Plitas, G.; Cornish, A. E.; Konopacki, C.; Prabhakaran, S.; Nainys, J.; Wu, K.; Kiseliovas, V.; Setty, M.; Choi, K.; Fromme, R. M.; Dao, P.; McKenney, P. T.; Wasti, R. C.; Kadaveru, K.; Mazutis, L.; Rudensky, A. Y.; Pe'er, D., Single-Cell Map of Diverse Immune Phenotypes in the Breast Tumor Microenvironment. Cell 2018, 174 (5), 1293-1308.e36.

132. Chung, W.; Eum, H. H.; Lee, H.-O.; Lee, K.-M.; Lee, H.-B.; Kim, K.-T.; Ryu, H. S.; Kim, S.; Lee, J. E.; Park, Y. H.; Kan, Z.; Han, W.; Park, W.-Y., Single-cell RNA-seq enables comprehensive tumour and immune cell profiling in primary breast cancer. Nature Communications 2017, 8 (1).

133. Gubin, M. M.; Artyomov, M. N.; Mardis, E. R.; Schreiber, R. D., Tumor neoantigens: building a framework for personalized cancer immunotherapy. Journal of Clinical Investigation 2015, 125 (9), 3413-3421.

134. Hu, G.; Tang, Q.; Sharma, S.; Yu, F.; Escobar, T. M.; Muljo, S. A.; Zhu, J.; Zhao, K., Expression and regulation of intergenic long noncoding RNAs during T cell development and differentiation. Nature Immunology 2013, 14 (11), 1190-1198.

135. Lubeck, E.; Cai, L., Single-cell systems biology by super-resolution imaging and combinatorial labeling. Nature Methods 2012, 9 (7), 743-748.

136. Patel, S. J.; Sanjana, N. E.; Kishton, R. J.; Eidizadeh, A.; Vodnala, S. K.; Cam, M.; Gartner, J. J.; Jia, L.; Steinberg, S. M.; Yamamoto, T. N.; Merchant, A. S.; Mehta, G. U.; Chichura, A.; Shalem, O.; Tran, E.; Eil, R.; Sukumar, M.; Guijarro, E. P.; Day, C.-P.; Robbins, P.; Feldman, S.; Merlino, G.; Zhang, F.; Restifo, N. P., Identification of essential genes for cancer immunotherapy. Nature 2017, 548 (7669), 537-542.

137. Savas, P.; Virassamy, B.; Ye, C.; Salim, A.; Mintoff, C. P.; Caramia, F.; Salgado, R.; Byrne, D. J.; Teo, Z. L.; Dushyanthen, S.; Byrne, A.; Wein, L.; Luen, S. J.; Poliness, C.; Nightingale, S. S.; Skandarajah, A. S.; Gyorki, D. E.; Thornton, C. M.; Beavis, P. A.; Fox, S. B.; Darcy, P. K.; Speed, T. P.; Mackay, L. K.; Neeson, P. J.; Loi, S., Single-cell profiling of breast cancer T cells reveals a tissue-resident memory subset associated with improved prognosis. Nature Medicine 2018, 24 (7), 986-993.

138. Shalek, A. K.; Satija, R.; Adiconis, X.; Gertner, R. S.; Gaublomme, J. T.; Raychowdhury, R.; Schwartz, S.; Yosef, N.; Malboeuf, C.; Lu, D.; Trombetta, J. J.; Gennert, D.; Gnirke, A.; Goren, A.; Hacohen, N.; Levin, J. Z.; Park, H.; Regev, A., Single-cell transcriptomics reveals bimodality in expression and splicing in immune cells. Nature 2013, 498 (7453), 236-240.

139. Zhang, S.-D.; Zhao, S.; Fung-Leung, W.-P.; Bittner, A.; Ngo, K.; Liu, X., Comparison of RNA-Seq and Microarray in Transcriptome Profiling of Activated T Cells. PLoS ONE 2014, 9 (1), e78644.

140. Zheng, C.; Zheng, L.; Yoo, J.-K.; Guo, H.; Zhang, Y.; Guo, X.; Kang, B.; Hu, R.; Huang, J. Y.; Zhang, Q.; Liu, Z.; Dong, M.; Hu, X.; Ouyang, W.; Peng, J.; Zhang, Z., Landscape of Infiltrating T Cells in Liver Cancer Revealed by Single-Cell Sequencing. Cell 2017, 169 (7), 1342-1356.e16.

141. Choi, H.; Wadduwage, D. N.; Tu, T. Y.; Matsudaira, P.; So, P. T. C., Three-dimensional image cytometer based on widefield structured light microscopy and high-speed remote depth scanning. Cytometry Part A 2015, 87 (1), 49-60.

142. Goda, K.; Ayazi, A.; Gossett, D. R.; Sadasivam, J.; Lonappan, C. K.; Sollier, E.; Fard, A. M.; Hur, S. C.; Adam, J.; Murray, C.; Wang, C.; Brackbill, N.; Di Carlo, D.; Jalali, B., High-throughput single-microparticle imaging flow analyzer. Proceedings of the National Academy of Sciences 2012, 109 (29), 11630-11635.

143. Goda, K.; Filby, A.; Nitta, N., In Flow Cytometry, Image Is Everything. Cytometry Part A 2019, 95 (5), 475-477.

144. Gu, Y.; Zhang, A. C.; Han, Y.; Li, J.; Chen, C.; Lo, Y. H., Machine Learning Based Real-Time Image-Guided Cell Sorting and Classification. Cytometry Part A 2019, 95 (5), 499-509.

145. Han, Y.; Gu, Y.; Zhang, A. C.; Lo, Y.-H., Review: imaging technologies for flow cytometry. Lab on a Chip 2016, 16 (24), 4639-4647.

146. Han, Y.; Lo, Y.-H., Imaging Cells in Flow Cytometer Using Spatial-Temporal Transformation. Scientific Reports 2015, 5 (1).

147. Martin, C.; Li, T.; Hegarty, E.; Zhao, P.; Mondal, S.; Ben-Yakar, A., Line excitation array detection fluorescence microscopy at 0.8 million frames per second. Nature Communications 2018, 9 (1).

148. Merola, F.; Memmolo, P.; Miccio, L.; Savoia, R.; Mugnano, M.; Fontana, A.; D'Ippolito, G.; Sardo, A.; Iolascon, A.; Gambale, A.; Ferraro, P., Tomographic flow cytometry by digital holography. Light: Science & Applications 2016, 6 (4), e16241-e16241.

149. Quint, S.; Christ, A. F.; Guckenberger, A.; Himbert, S.; Kaestner, L.; Gekle, S.; Wagner, C., 3D tomography of cells in micro-channels. Applied Physics Letters 2017, 111 (10), 103701.

150. Sung, Y.; Lue, N.; Hamza, B.; Martel, J.; Irimia, D.; Dasari, R. R.; Choi, W.; Yaqoob, Z.; So, P., Three-Dimensional Holographic Refractive-Index Measurement of Continuously Flowing Cells in a Microfluidic Channel. Physical Review Applied 2014, 1 (1).

151. Wu, J.; Li, J.; Chan, R. K. Y., A light sheet based high throughput 3D-imaging flow cytometer for phytoplankton analysis. Optics Express 2013, 21 (12), 14474.

152. Wu, J.-L.; Xu, Y.-Q.; Xu, J.-J.; Wei, X.-M.; Chan, A. C. S.; Tang, A. H. L.; Lau, A. K. S.; Chung, B. M. F.; Cheung Shum, H.; Lam, E. Y.; Wong, K. K. Y.; Tsia, K. K., Ultrafast laser-scanning time-stretch imaging at visible wavelengths. Light: Science & Applications 2016, 6 (1), e16196-e16196.

153. Han, Y.; Tang, R.; Gu, Y.; Zhang, A. C.; Cai, W.; Castor, V.; Cho, S. H.; Alaynick, W.; Lo, Y.-H., Cameraless high-throughput three-dimensional imaging flow cytometry. Optica 2019, 6 (10), 1297.